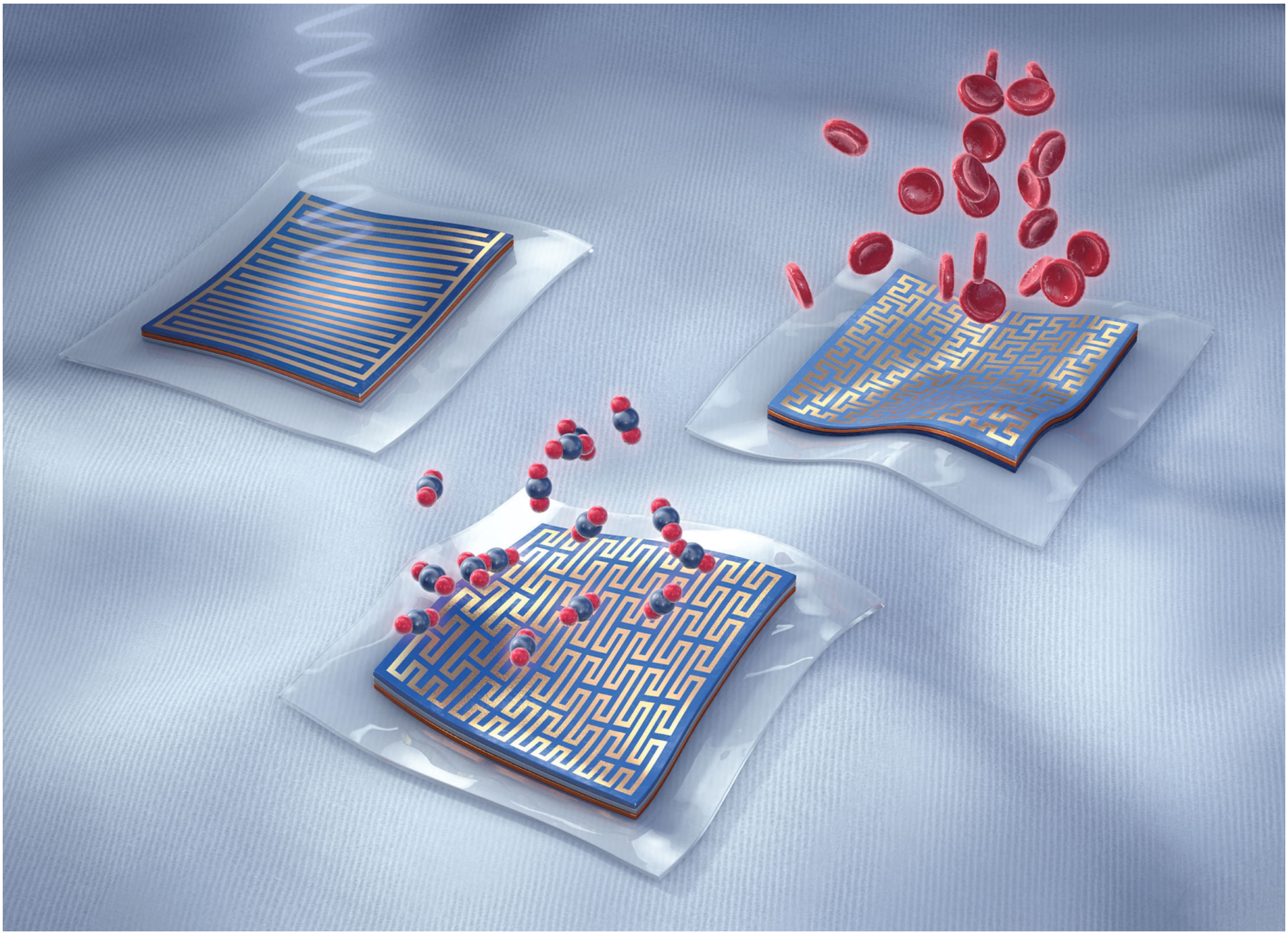

Showcasing research from Prof. Prashant Sonar's laboratory, School of Chemistry and Physics, Queensland University of Technology (QUT), Brisbane, QLD 4000, Australia and Prof. Khaled N. Salama's laboratory, Sensors Lab, AMPM Center, Computer, Electrical and Mathematical Science and Engineering Division, King Abdullah University of Science and Technology, Saudi Arabia

Organic field-effect transistor-based flexible sensors

This extensive review of organic field-effect transistors (OFETs) will potentially help improve the perspective of scientists working in interdisciplinary fields and gives a thorough insight on the advantages and challenges associated with using them in flexible electronic applications.

As featured in:

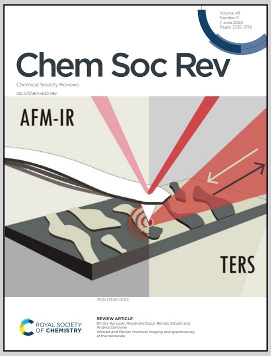

See Sandeep G. Surya,
Khaled N. Salama,
Prashant Sonar *et al.*,
Chem. Soc. Rev., 2020, **49**, 3423.

ROYAL SOCIETY
OF **CHEMISTRY**

rsc.li/chem-soc-rev

Chem Soc Rev

ROYAL SOCIETY OF CHEMISTRY

REVIEW ARTICLE

View Article Online
View Journal | View Issue

Check for updates

Cite this: *Chem. Soc. Rev.*, 2020, **49**, 3423

Received 4th February 2020

DOI: 10.1039/c9cs00811j

rsc.li/chem-soc-rev

Organic field-effect transistor-based flexible sensors†

Saravanan Yuvaraja, ‡[a] Ali Nawaz, ‡[bc] Qian Liu, [d] Deepak Dubal,[de] Sandeep G. Surya, *[a] Khaled N. Salama *[a] and Prashant Sonar *[de]

Flexible electronic devices have attracted a great deal of attention in recent years due to their flexibility, reduced complexity and lightweight. Such devices can conformably attach themselves to any bendable surface and can possess diverse transduction mechanisms. Consequently, with continued emphasis on innovation and development, major technological breakthroughs have been achieved in this area. This review focuses on the advancements of using organic field-effect transistors (OFETs) in flexible electronic applications in the past 10 years. In addition, to the above mentioned features, OFETs have multiple advantages such as low-cost, readout integration, large-area coverage, and power efficiency, which yield synergy. To begin with, we have introduced organic semiconductors (OSCs), followed by their applications in various device configurations and their mechanisms. Later, the use of OFETs in flexible sensor applications is detailed with multiple examples. Special attention is paid to discussing the effects induced on physical parameters of OFETs with respect to variations in external stimuli. The final section provides an outlook on the mechanical aspects of OSCs, activation and revival processes of sensory layers, small area analysis, and pattern recognition techniques for electronic devices.

---

[a] *Sensors Lab, Advanced Membranes and Porous Materials Center, Computer, Electrical and Mathematical Science and Engineering Division, King Abdullah University of Science and Technology, Saudi Arabia. E-mail: sandeep.surya@kaust.edu.sa, khaled.salama@kaust.edu.sa*

[b] *Departamento de Física, Universidade Federal do Paraná, Caixa Postal 19044, 81531-990, Curitiba, PR, Brazil*

[c] *Brazilian Nanotechnology National Laboratory (LNNano), Brazilian Center for Research in Energy and Materials (CNPEM), 13083-970, Campinas, São Paulo, Brazil*

[d] *School of Chemistry and Physics, Queensland University of Technology (QUT), Brisbane, QLD 4000, Australia. E-mail: sonar.prashant@qut.edu.au*

[e] *Centre for Materials Science, Queensland University of Technology, 2 George Street, Brisbane, QLD 4000, Australia*

† This article is dedicated to the memory of late Prof. Ivo A. Hümmelgen.

‡ These authors contributed equally to this work.

Saravanan Yuvaraja

Saravanan Yuvaraja received his bachelor's degree from Anna University, India, in Electronics and Communication Engineering with a first class in 2016. He also competed his MTech degree from Amity University, India, in the field of Solar and Alternative Energy Engineering in 2018. He is currently a PhD candidate in the Sensor Lab Group under the direction of Prof. Khaled Nabil Salama at King Abdullah University of Science in Saudi Arabia. His research interests are in developing flexible and wearable chemical sensors using organic semiconductors and metal organic frameworks on organic field effect transistor (OFET) chemiresistive, chemicapacitive platforms.

Ali Nawaz

Dr Ali Nawaz performed his post-doctoral research work at LNNano/CNPEM, Campinas, Brazil, working on the development of nano-membrane-based vertical organic transistors and sensors. He obtained his PhD in Physics from UFPR, Curitiba, Brazil (under the guidance of late Prof. Ivo A. Hümmelgen), where he was involved in the improvement of charge transport properties of low-voltage planar organic transistors. His research expertise and interests include organic transistors, sensors, device physics and engineering, micro-/nano-fabrication of organic devices and process development.

1. Introduction

1.1 Importance of flexible and wearable electronics

Wearable electronics have undergone a great evolution in the past few decades. While these devices have existed for several centuries—including inventions like portable and wearable clocks[1] and Nuremberg eggs in the 16th century[2]—only lately have they attracted significant attention in both academic and industrial fields. The progress in this technology can be seen, for example, by the advancement from pocket watches and wristwatches to current smartwatches such as the Apple watch and from phones to smartphones that can perform multiple modern-day functions. In addition, with ever-growing technological advancements in the Internet of Things (IoT), the wearable electronics industry met with increasing demands regarding futuristic applications that can be comfortably worn and readily blended into daily life.[3] The wearable device market is estimated to be worth approximately $67 billion by 2024,

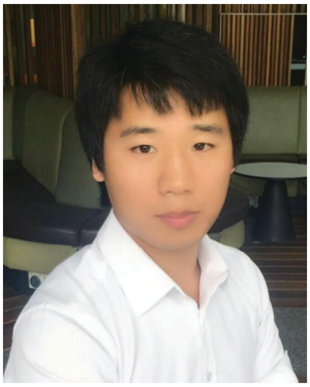

Qian Liu

Qian Liu received his MS degree from the Ocean University of China (OUC) in 2014 with joint supervision at Qingdao Institute of Bioenergy and Biotechnology (QIBEBT), Chinese Academy of Sciences (CAS). He is currently a PhD candidate at the School of Chemistry and Physics, Queensland University of Technology (QUT). His research interests focus on the design and synthesis of organic semiconducting materials based on dye molecules and their applications in various types of electronic devices.

Sandeep G. Surya

Sandeep G. Surya is a Postdoctoral Research Fellow at King Abdullah University of Science and Technology (KAUST), Kingdom of Saudi Arabia. He received his PhD degree from IIT Bombay and BTech degree from JNTU, Hyderabad. He worked as a Research Associate at Microsystems Technology Research Unit, CMM, Fondazione Bruno Kessler (FBK), Trento, Italy. He was a member of different teams working on explosive detectors and on Telemedicine. His work won the "Young Achiever Award" at IBAE-2019, GYTI AWARD at IIM-A 2012, the Fellowship at ISED 2011, and the P.P CHHABRIA AWARD OF EXCELLENCE in intelligent systems and robotics for the year 2009 at IIIT, Pune.

Khaled N. Salama

Khaled Nabil Salama received his BS degree from the Department of Electronics and Communications, Cairo University, Egypt, and his MS and PhD degrees from the Department of Electrical Engineering, Stanford University, USA, in 2000 and 2005. He was an Assistant Professor at Rensselaer Polytechnic Institute, NY, USA, between 2005 and 2009. He joined King Abdullah University of Science and Technology in January 2009, where he is now a professor and was the founding Program Chair until August 2011. He is the director of the Sensors Initiative, a consortium of 9 international universities. His work on CMOS sensors for molecular detection has been funded by NIH and DARPA, awarded the Stanford–Berkeley Innovators Challenge Award in biological sciences and was acquired by Illumina Inc. He is the author of 300 papers and 20 US patents on low-power mixed signal circuits for intelligent fully integrated sensors and neuromorphic circuits using memristor devices.

Prashant Sonar

*Prashant Sonar performed doctoral work at the Max-Planck Institute of Polymer Research, Mainz, Germany and was awarded PhD in 2004. He then moved to Swiss Federal Institute of Technology (ETH), Zurich, Switzerland, for his postdoctoral research from 2004 till 2006. From 2006 till 2014, he was working as a Research Scientist at the Institute of Materials Research and Engineering (IMRE), Agency of Science, Technology and Research (A*STAR), Singapore. Dr Sonar received the prestigious Future Fellowship (2013) from the Australian Research Council and was appointed an Associate Professor in July 2014 at Queensland University of Technology (QUT), Australia. A/Prof. Sonar is a Fellow of the Royal Society of Chemistry (FRSC) and a Foreign Fellow of the Maharashtra Academy of Sciences (FFMAS) and is currently serving as an Associate Editor of the journal Flexible and Printed Electronics, Material Research Express. He leads the Organic Electronic group at QUT and has published 147 peer-reviewed research papers and filed 11 patents to date.*

and it is expected that more than 1 trillion sensors will be designed and implemented in wearable electronics.

Wearable electronics is currently becoming increasingly prevalent in many aspects of life, including sports, communications, health and wellness, expenditure tracking and wireless payment, wireless keys, socialization, and so forth.[4] Fitness devices, to some extent, have dominated the wearable electronics market because of their universality and low cost. Such products not only help consumers in achieving their fitness goals but also allow them to conveniently perform numerous other functions such as listening to music and conducting video conference calls.

Another important application of wearable electronics lies in the medical area where the flexible sensors can be integrated into clothes or implanted in the human body to monitor the health and performance of a patient.[5] Such wearable sensors can further allow the detection of glucose, lactic acid, or uric acid by noninvasive chemical analysis of sweat, tears, or saliva without disrupting the outermost protective layers of the body's skin, which further reduces the risk of harm or infection.

Despite many significant advances, the utilization of rigid substrates (generally glass) in electronic devices still reduces the integration density of wearable applications, especially in skin-like electronics, such as medical treatment and implants, artificial skin and prosthetics, and biological studies. Therefore, developing electronic devices with flexible substrates is an urgent and cutting-edge research topic. Thus, several academic groups have dedicated their efforts to study devices based on mechanical flexibility and stretchability of materials.[6,7] The sensor component in electronic devices plays a significant role and can be considered the most fundamental part of wearable electronics. For example, the development of e-skin requires many sensor components to stimulate the response of human skin to external stimuli.[8]

As the examples above illustrate, flexible and wearable sensors are presently a topic of interest since they can enlarge the application scope and accelerate the advancement of wearable electronics. For instance, development of physical sensors such as strain sensors for electronic skin (e-skin) platforms has recently gained more attention. The most pressing challenges in developing e-skin based sensors stem from the material behavior problems such as poor mechanical stability, diverse sensing behavior and weak self-healing power. Unlike other materials, the human skin evolved from nature is composed of many layers whose sensing functions such as temperature, pressure, and force are strategically synchronized. This strategy helps the skin to produce logical responses facilitating the human system to react accordingly. Hence, we need to develop novel materials or tweak the existing organic materials which can potentially sense various chemical and physical changes simultaneously without compromising the individual sensing performance. In addition to this, we need to propose innovative device strategies for plausible integration of suitable materials on low-cost, easily fabricated and biocompatible platforms.[9] By considering this, many researchers have used innovative strategies to develop skin mimic materials and successfully integrated them on OFET platforms to enable organic based e-skin applications. For instance, Mannsfeld *et al.*[10] have integrated an organic elastomer as a gate dielectric into the OFET platform. Flexibility in tuning the material properties and the ability to self-heal after heavy deformations are some of the important properties that attracted them to use elastomers for tactile/pressure sensing applications. In the beginning, the elastomer was sandwiched between the conductive electrodes to realize the capacitance transducer mode. To augment the sensitivity toward low pressure conditions, the elastomer was micro-machined to different micro-structures such as pyramid and horizontally displaced pillars. However, it is obvious that the classical capacitance mode is not compatible to achieve electronic skin functions. This is due to the fact that the function of the epidermis and dermis regions of the human skin system exactly coincides with the multiple layers of an OFET device such as the substrate, dielectric, semiconductor and S/D contacts.[9] Hence, the authors have successfully integrated a micro-machined elastomer as a gate dielectric in a top-gate bottom-contact Rubrene based OFET. Moreover, the elastic properties of the employed elastomer were tuned in such a way that it can exhibit excellent sensitivity toward wide applied pressure conditions. The major drawback of this work is the mono-sensing capability of the OFET sensor. This problem critically limits the use of reported OFET for e-skin applications. To solve this problem, recently Hannah *et al.*[11] have successfully demonstrated the multi-sensing capabilities of an OFET sensor which aligns with the requirement of the electronic skin applications. To sense different stimulants such as pressure and temperature, a currently blooming ferroelectric P(VDF-TrFE) material was chosen due to its promising piezo-electric and pyro-electric characteristics. The chosen ferroelectric material was employed as a gate dielectric in a bottom-gate top-contact DNTT based OFET device platform. Due to the synergistic combination between P(VDF-TrFE) and DNTT materials, the developed OFET device was able to sense static force and static and dynamically changing temperature conditions simultaneously with high accuracy at low power consumption. Hence, these significant breakthroughs in the field of electronic skin based sensors strongly indicate the current research progress in wearable electronics.

It is also important to note that the development of smart materials with exceptional capabilities alone would not be able to grow the giant wearable technology sector. We have to also realize that some of the important aspects such as large-scale fabrication of flexible organic sensors, the feasibility of wirelessly communicating the sensor data and implementation of the decision-making algorithms are deciding factors too. The former one is of prime concern because of its core importance in the whole sensing system. It is important to note that in the past 5 years, various researchers have successfully demonstrated that some of the important components of OFET devices such as organic semiconductors, polymer dielectrics and metal nanoparticles for electrodes can be easily patterned and directly printed on the desired flexible substrates.[12,13] This ultimately led to the fabrication of organic transistor based integrated circuits for various applications under low cost and room temperature conditions.[13] As a result, in recent years, many innovative printing techniques emerged such as ink-jet, reverse offset, roll-to-roll gravure offset, screen printing and dispensing printing.[14] Spatial/pattern resolution and film thickness are some of the key parameters that decide the performance of the above mentioned printing techniques.[12] Ink-jet printing techniques have received higher attention in recent years solely because of two important reasons such as the plate-free printing process (unlike offset printers) and low viscous printable inks. The latter one is more crucial because inks with low viscous nature critically avoid the use of toxic additives which might damage the intrinsic properties of inks, thereby the device performance.[15] By using this technique, recently Rei *et al.*[16] have successfully printed a trap-free DTBDT based OFET device, with 10 μm and 26 μm channel lengths, on a glass substrate. The fabricated device exhibited low threshold voltage, negligible hysteresis and good ambient stability. Interestingly, the ink-jet printer is the only promising technique that can allow us to deposit the film on flexible substrates with a thickness down to 10 nm.[12] The dark side of this technique is the poor spatial resolution of the OFET device which can be as low as 10 μm. To solve these issues, many roll-to-roll (R–R) compatible printing techniques were proposed such as flexographic based, simple, direct and offset gravure based processes.[17] Among them, gravure offset printing is adopted widely because of (i) uniform film formation capability with relatively low roughness and (ii) low viscous ink requirements.[18,19] The former advantage helps to improve the film quality such as a dielectric film stacked on top of low roughness gravure printed electrodes.[20] These important features incredibly pave the way for improving the overall device performance. However, by using the offset gravure printing technique, the maximum device resolution achieved to date is 5 μm.[17] The development of an R–R based robust printing technique with excellent spatial resolution, ideally sub-μm, is indispensable to achieve large-scale production of OFET devices with reliable performance and effectively combine them to develop compact integrated circuits. To achieve the required spatial resolution and accuracy, a novel R–R compatible reverse offset printing (ROP) technique is developed.[21] Basically, the ROP process is governed by three important process stages starting from (i) drop-casting ink on the supporting layer (*e.g.* – PDMS), (ii) micro-patterning the stamp and using it to carry the ink from the supporting layer and (iii) finally, the stamp will transfer the ink to the desired flexible substrate suspended on top of the rolling cylinder.[21,22] The successful functioning of transferred ink on the substrate depends on some of the crucial parameters such as (i) roughness of the stamp and substrate, (ii) substrate wettability, (iii) viscosity of ink and (iv) pressure applied on the ink by the stamp.[22] One major obstacle that is often discarded in any offset printing is the effect of temperature generated by the high speed running, which in turn increases the operating temperature altering the properties of ink. Subsequently, undesirable stiction of the substrate to the cylinders follows due to such effects. Hence, rigorous optimizations are ideally required to print the device with high resolution and throughput. By considering these requirements, recently Ask *et al.*[23] have successfully printed organic transistors with a high resolution close to the sub-μm level without compromising the accuracy and reliability. However, some of the problems such as scalability of the fabrication process, miniaturization of organic devices and the corresponding poor electrical performance stand as a barrier for the fabrication of organic flexible sensors on a large scale.[24,25] Hence, more innovative solutions and groundbreaking research are essential to overcome the major problems in order to realize the fully organic and flexible devices for wearable electronics technology in the near future. This article thoroughly reviews the recent progress made in flexible sensors based on organic field-effect transistors (OFETs) and provides a systematic summary of different types of OFET-based flexible sensors, including chemical sensors, light sensors, biosensors, and pressure sensors. In addition, the various organic semiconducting materials utilized in such devices are summarized in detail. Thus, the review serves a purpose of providing current status and future guidance for the development of wearable electronics.

1.2 Organic semiconducting materials for flexible OFET devices

There are a wide range of conjugated small molecules, polymers, and room-temperature liquid crystals used as active channel semiconductors in OFET devices. The important criteria in selecting these materials depend on the highest occupied molecular orbital (HOMO) and lowest unoccupied molecular orbital (LUMO) energy levels of these molecules and their closeness to the work function of metals. The difference between HOMO and LUMO serves as the bandgap of organic semiconductors (OSCs) that is extracted from the cyclic voltammetry data.[26] The materials covered in this review have a bandgap in the range of 1 eV to 3 eV, which are suitable for flexible device applications. Table 1 lists the wide range of semiconducting materials used for flexible OFET platforms, including various aspects such as chemical name and structure (Scheme 1), HOMO level, LUMO level, deposition method, and deposition rate/solvent information.

Among different materials, semiconducting polymers and liquid crystals proved to be easy for processing by various techniques such as drop casting, spin coating, and spray coating, whereas small molecules needed complex deposition systems such as thermal evaporators, wherein the deposition rates and substrate temperature must be identified. Due to such controlled deposition parameters, uniformity and high quality of thin films can be achieved in these materials. During gas sensing, these ultrathin films facilitate interaction between the channel region at the insulator/semiconductor (I/S) interface and gas molecules with fewer diffusion-related losses, thus contributing to high sensitivities and specific binding properties. Subsequently, these materials were modified by means of functionalization on the surface of organic semiconductors to open up functional groups to interact with the chemical and bio analytes, or they were doped with other materials to induce properties such as piezoresistivity/piezoelectricity. Furthermore, to achieve an array of sensors, nanolithography is a good patterning solution because of its low complexity in implementation.

The sections below detail different aspects of organic semiconducting materials and their utilization in multiple configurations leading to wearable electronics technology.

1.3 Types of OFET sensors and their working mechanisms

In an OFET, the input signal is voltage, applied to the semiconducting channel *via* a capacitive structure. This signal,

Table 1 Detailed information regarding the flexible OFET devices fabricated using different OSCs

Materials	Class	HOMO/LUMO	Type	Deposition	Deposition rate (Å min^{-1})/solvent
1	Small molecule	—/—	n-Type	Spin coating	NA/chloroform
2	Small molecule	5.1/3.4	p-Type	Spray coating	NA/1,2-DCB
3	Polymer	5.35/3.98	p-Type	Spin coating	NA/1,2-DCB
4	Polymer	5.31/3.3	p-Type	Bar coating	NA/1,2-DCB
5	Polymer	5.24/3.37	p-Type	Bar coating, spin coating	NA/1,2-DCB
6	Sing. crystal	5.85/—	p-Type	Mechanical probe	—
7	Polymer	5.24/2.97	p-Type	Electro-spinning	NA/1,2-DCB
8	Small molecule	5.16/3.35	p-Type	Evaporation	0.5/NA
2	Small molecule	5.2/3.14	p-Type	Drop coating	NA/1,2-DCB
9	Small molecule	5.4/2.5	p-Type	Evaporation	—
10	Polymer	5.16/3.2	p-Type	Spin coating	NA/1,2-DCB
11	Small molecule	5.36/2.53	p-Type	Evaporation	—
12	Polymer	5.35/3.81	p-Type	Spin coating	NA/toluene
13	Small molecule	6.38/4.38	n-Type	Spin coating	NA/chloroform
14	Small molecule	—/—	p-Type	Picofilter fluidic dispenser	NA/1,2,4-TCB
15	Polymer	5.23/—	p-Type	Spin coating	NA/1,2-DCB
16	Polymer	5.25/2.3	p-Type	Spin coating	NA/chlorobenzene, chloroform
17	Small molecule	5.33/2.04	p-Type	Evaporation	0.4–0.5/NA
18	Small molecule	5.2/3.5	p-Type	Evaporation	—

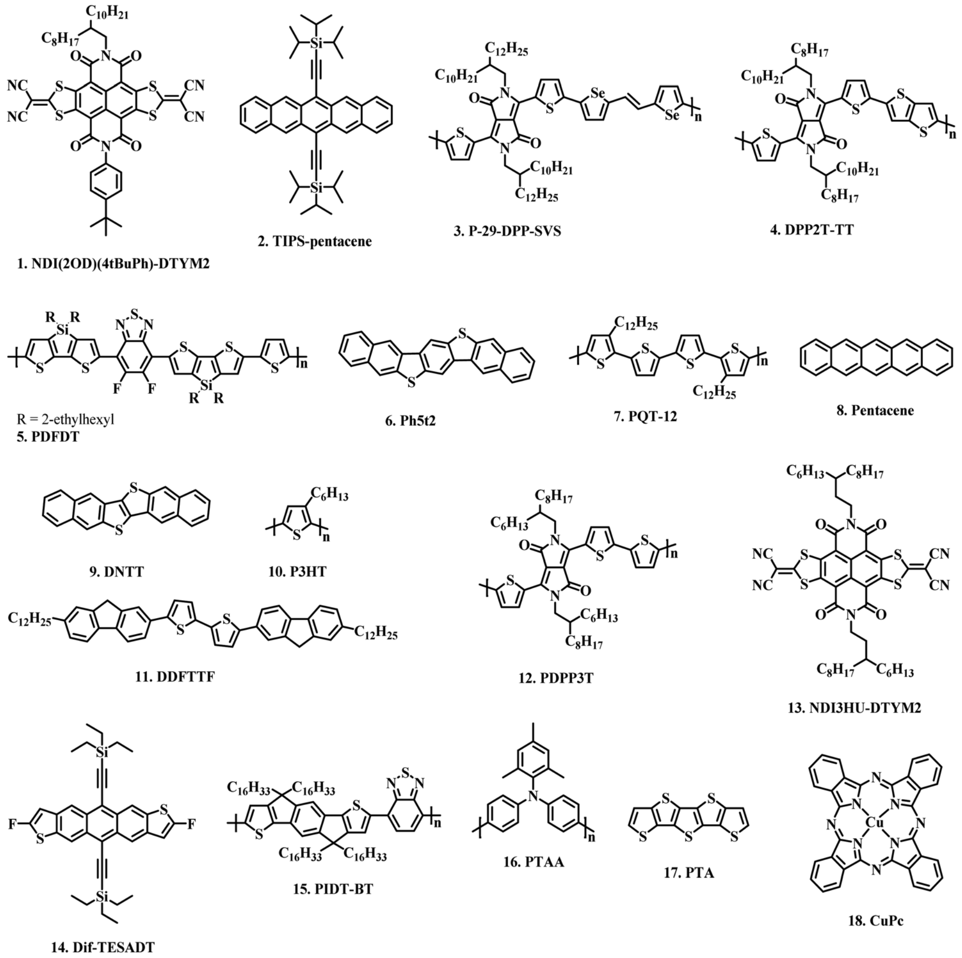

Scheme 1 The chemical structures of some organic semiconducting materials used for flexible OFET platforms.

called gate voltage, modulates the current in a narrow portion of the OSC layer (the channel) between two contacts, the source and drain.[27] An OFET is typically fabricated in a thin-film multilayered structure (Fig. 1a)—initially developed for amorphous silicon devices[28]—where the gate capacitor consists of an insulator sandwiched between a metal (gate) and a thin OSC layer. On the OSC side, the source and drain contacts are used for, respectively, injecting and extracting the current flow (I_D), which is dependent on both the gate bias (V_{GS}) and the drain voltage (V_{DS}). The conductance of the OSC in the channel area is switched between the on and off states by the gate, which is capacitively coupled through a thin gate insulating layer. The V_{GS} regulates the I_D between the source and drain electrodes under a constant V_{DS}.[29]

Although transistor electrodes are typically formed from a metal, nonmetallic electrodes (*e.g.*, those made from conducting graphite[31] or polymers[32,33]) have also been reported. The low thickness of the OSC layer is because an OFET does not operate in inversion mode, *i.e.*, the carriers that accumulate in the OSC channel are the same, which usually flow in the semiconductor bulk in the off state. Hence, applying a thick OSC layer would cause a high off state current,[34–37] compromising the switching ability of the OFET. The equations quantifying the *I*–*V* characteristics of OFETs are normally derived from the model developed for metal–insulator–semiconductor FET devices.[38] In the saturation-regime (eqn (1)) and linear regime (eqn (2)), I_D is given as:

$$I_{\mathrm{Dsat}} = \frac{W\mu_{\mathrm{FET}}C_{\mathrm{i}}(V_{\mathrm{GS}} - V_{\mathrm{T}})^2}{2L}, \quad (V_{\mathrm{DS}} > V_{\mathrm{GS}} - V_{\mathrm{T}}) \tag{1}$$

$$I_{\mathrm{Dlin}} = \frac{W\mu_{\mathrm{FET}}C_{\mathrm{i}}(V_{\mathrm{GS}} - V_{\mathrm{T}})(V_{\mathrm{DS}})}{L} \quad (V_{\mathrm{DS}} < V_{\mathrm{GS}} - V_{\mathrm{T}}) \tag{2}$$

where μ_{FET} corresponds to the field-effect charge carrier mobility, C_{i} to the capacitance per unit area of the gate insulator, V_{T} to the device threshold voltage, and W and L to the length and width of the OSC channel.

A number of parameters, including μ_{FET}, on–off current ratio ($I_{\mathrm{on}}/I_{\mathrm{off}}$), and threshold voltage (V_{T}), evaluate the performance of OFET devices. μ_{FET} can be defined as the average drift velocity of a charge carrier per unit electric field and decides the processing speed and on-currents of OFETs. Typical μ_{FET} values are in the 10^{-3} to 10^{-1} cm^2 V^{-1} s^{-1} range, but they can be greater than 5 cm^2 V^{-1} s^{-1} for highly ordered OSCs.[39–41] $I_{\mathrm{on}}/I_{\mathrm{off}}$ is defined as the ratio of I_D at the maximum V_{GS} value (in the accumulation mode) to the I_D below $V_{GS} - V_T$ (in the depletion mode). It indicates the switching performance of the OFET, and a low off-state current is, in principle, required to ensure a true switching of the device to the off state. To realize complementary circuits having large gains and small power consumption, transistors with large $I_{\mathrm{on}}/I_{\mathrm{off}}$ are required. V_T is the minimum required V_{GS} for the accumulation of free carriers at the I/S interface to form a channel in the OSC layer between the source and drain electrodes. Lower V_T helps in reducing the power consumption of the devices and is, therefore, useful in manufacturing portable devices. In principle, V_T in OFETs arises because of the traps induced by the non-crystalline structure of OSCs and/or those originating from the surface of the gate insulator layer.

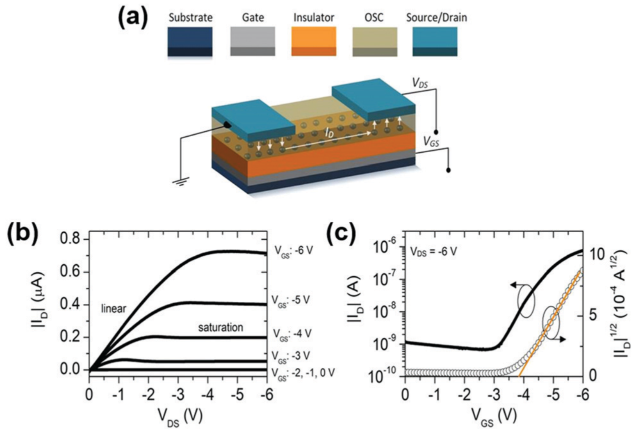

Fig. 1 (a) Schematic representation of an OFET device in a typical bottom-gate configuration. Source is, conventionally, the grounded terminal, and the biases V_{DS} and V_{GS} control the charge transport (resulting in electric current I_D) injected from the source and extracted at the drain; (b) output characteristics (I_D–V_{DS}) and (c) transfer characteristics (I_D–V_{GS}) of OFETs based on diketopyrrolopyrrole-naphthalene (PDPP-TNT). (b) and (c) are reprinted with permission from Nawaz *et al.*[30] (copyright 2018, IOP Publishing).

As an example of the electrical characteristics of OFETs, Fig. 1b and c show the *I*–*V* curves of devices in which diketopyrrolopyrrole-naphthalene (PDPP-TNT) was used as the OSC.[30] The output characteristics (I_D–V_{DS}) in Fig. 1b clearly demonstrate the linear and saturation regimes, whereas Fig. 1c shows the transfer characteristics (I_D–V_{GS}) and the $|I_D|^{1/2}$–V_{GS} plot, which can be used to easily extract the V_T and μ_{FET}.

OSCs show susceptibility to noncovalent π-interactions, which allows the detection of external chemical/physical stimuli. This is because the energy supplied in the form of heat/light can result in the modulation of conductivity in the effective channel of OFETs. In this way, OFETs can be efficiently used as sensing devices. Mechanical work, such as pressure, can also alter the output current of OFET devices; such alterations are mainly related to changes in the distribution of charge carriers among molecules in the effective conducting channel.

Tremendous advancements in molecular engineering allow control over the optoelectronic properties of OSCs (electronic energy levels, electrical/optical band gap, *etc.*) by chemically modifying their structures that can regulate the molecular order and/or morphology.[42,43] Consequently, ad hoc-designed OSCs, functionalized with particular recognition receptors or sites, can be used as the sensing layers, providing OFET sensors with the desired capability of the detection of light or environmental molecules (analytes).[44,45]

1.3.1 Organic phototransistors. In organic phototransistors (OPTs), light absorption modulates the electronic properties in the conducting channel, which causes transduction of the light-stimulating states into electrical signals. Fabrication of OPTs is typically required to enable direct interaction of light with the photoactive organic layer, which is normally required to demonstrate a wide absorption spectrum, and enhanced charge transport properties.[46,47]

Similar to conventional OFET devices, the device geometries of OPTs can be divided into four typical structures: top gate top contact (TGTC), top gate bottom contact (TGBC), bottom gate top contact (BGTC), bottom gate bottom contact (BGBC), as shown in Fig. 2. The light can be illuminated onto the device from the top side (Fig. 2) or the bottom side (not shown here). Depending on the device geometry and direction of light illumination, sufficient transparency of the gate electrode and gate insulator is required so that the light arriving on the OSC

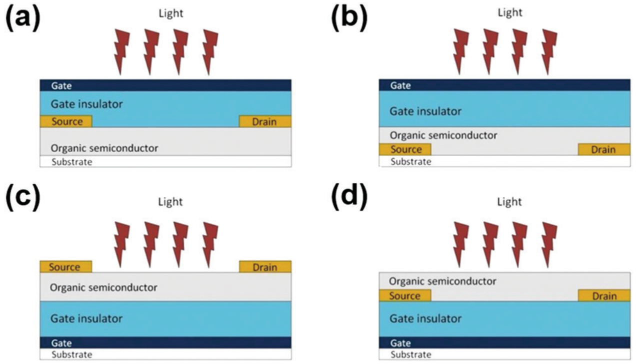

Fig. 2 Typical device geometries used for OPTs: (a) TGTC, (b) TGBC, (c) BGTC, and (d) BGBC.

layer effectively interacts with the OSC molecules, thereby sufficiently modulating the conductivity in the OFET channel.[44]

There are typically two operating modes in OPTs, photovoltaic mode and photoconductive mode, both of which are related to photocurrent (I_{ph}) and incident optical power (P_{opt}).[48] The photovoltaic mode is dominant when the transistors are operated in the accumulation regime ($V_{\mathrm{GS}} < V_{\mathrm{T}}$), whereas the photoconductive mode is dominant when the transistors are operated in the depletion regime ($V_{\mathrm{GS}} > V_{\mathrm{T}}$). Among other device parameters, photoresponsivity (R) and photosensitivity (P) are critical for the performance of OPTs. R and P are expressed as:[47,48]

$$R = \frac{I_{\mathrm{D,light}} - I_{\mathrm{D,dark}}}{SP_{\mathrm{i}}}, \tag{3}$$

$$P = \frac{I_{\mathrm{D,light}} - I_{\mathrm{D,dark}}}{I_{\mathrm{D,dark}}}, \tag{4}$$

where $I_{\mathrm{D,light}}$ and $I_{\mathrm{D,dark}}$ correspond to drain currents under illumination and in darkness, respectively. S is the effective device area, and P_{i} is the incident optical power.

Fig. 3a presents the transfer characteristics of poly(3,3-didodecylquaterthiophene):poly(ethylene oxide) (PQT-12:PEO) nanofiber-based OPTs in darkness and under illumination.[49] Similarly, Fig. 3b shows the results of real-time photo-sensing tests of the same devices performed by repeatedly turning the light off and on at 470 and 670 nm, respectively. These devices were fabricated on flexible polyethylene terephthalate (PET) textile substrates and demonstrated an R of 930 mA W^{-1} and P of 2.76 while exposed to 470 nm wavelength light. The authors also prepared 10 × 10 OPT arrays to be used as flexible image sensors. A red laser source was exposed to the sensor array, and it was observed that the OPTs are able to detect incoming signals at a high resolution. These results highlight the potential of PQT-12:PEO nanofiber OPT arrays to be applied as wearable photo or image sensors.

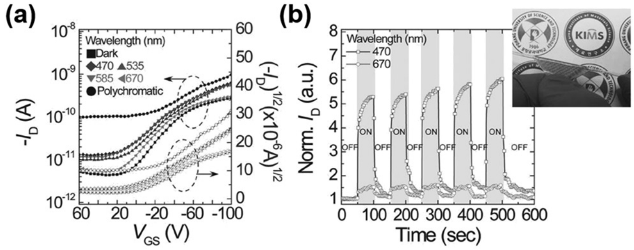

Fig. 3 (a) I_{D}–V_{GS} characteristics of PQT-12: PEO nanofiber-based OPTs under light illumination with different wavelengths, and (b) real-time photoresponse while the devices were illuminated using a monochromatic light with two different wavelengths. The inset of (b) shows the photograph of a flexible phototransistor array upon bending at a radius of ~0.75 mm (reprinted with permission from Lee *et al.*,[49] copyright 2016, Wiley-VCH).

A large number of reports on OPTs stress on improving the optical responsivity by making use of photoactive OSCs, and by performing optimizations on the device structure.[50,51] Nevertheless, even after significant advancements, one of the remaining challenges corresponds to distinguishing lights with different wavelengths, which is – in fact – the purpose of the photoreceptor cells in the human eye retina.[52] Besides, both effective photodetection and recording of exposure energy are prerequisites for radiation monitoring in the emerging fields of flexible and wearable electronics.[53] Recent reports have suggested a viable and straightforward approach to address this issue by integrating the memory functionality in OPT devices.[54–58] This results in the preparation of a new class of electronic devices, OPT memories, that integrate photodetection and signal storage in a single device. In this way, the recording of light exposure can be realized by the nonvolatile and cumulative photo-assisted charge trapping.[59,60] A promising approach relies on the utilization of molecular photochromics.[61] Chen *et al.* deposited a self-assembled monolayer (SAM) of diarylethene (DAE) photochromic onto the high-κ dielectric hafnium dioxide ($\mathrm{HfO_2}$) to realize flexible arrays of pentacene-based low-voltage OPT memories (Fig. 4a).[62] The programming and erasing cycles of I_{D} as a function of light intensity are shown in Fig. 4b. Firstly, the device was preset to an initial state by UV light illumination and a gate pulse of −3 V. The programming was then performed by applying 633 nm light with four different levels of light intensity. The initial programming signal caused a sudden increase in I_{D}. In principle, the UV irradiation resulted in the creation of photoexcited electrons, and at the same time, the DAE molecule transformed from its open to closed state *via* formation of a C–C bond. The latter phenomenon led to π-electron delocalization and decreased the LUMO energy of DAE to −3.22 eV, which is lower than that of pentacene. This resulted in the tunneling of high-energy electrons through the DAE SAM to charge the DAE/$\mathrm{HfO_2}$ interface. These trapped electrons provided an additional electric field, thereby leading to an increase in I_{D}. When the light was removed, the stored information was retained for at least 3 hours. This is understandable because the LUMO of DAE in its closed state is lower than that of pentacene, which effectively prevented the trapped electrons at the DAE/$\mathrm{HfO_2}$ interface from leaking through the pentacene/DAE interface. In order to recover to the initial state, a gate pulse of −3 V was applied. The authors also analyzed the changes in V_{T} to evaluate the memory window and retention ability of the OPT memories (Fig. 4c). In this case, the memory window was observed to be as large as 50% of the operating voltage, whereas the read-current ratios at V_{GS} = 0 V was as high as 4.4 × 10^4. Fig. 4d shows a photograph of a flexible OPT memory array (30 × 30 array with 900 memory devices) fabricated

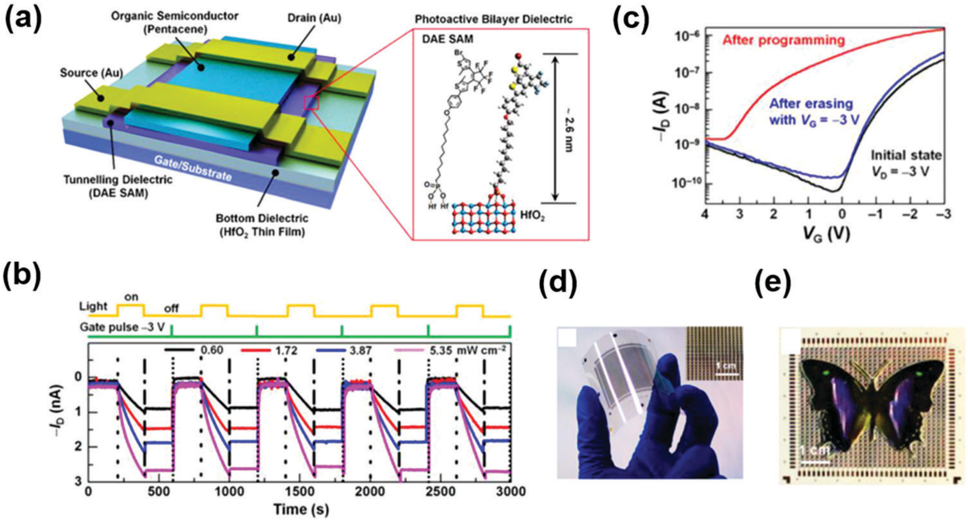

Fig. 4 (a) Schematic illustration of pentacene-based OPT memory device consisting of hybrid DAE/HfO_2 as the photoactive dielectric layer (molecular structure and real-space model of DAE bonding to HfO_2 is shown in the inset); (b) memory characteristics with five representative programming and erasing cycles as a function of light intensity. Programming is performed by 633 nm light illumination with four different intensities, while erasing is performed by a gate pulse of −3 V (V_{DS} = −100 mV and V_{GS} = 0 V); (c) $I_D \times V_{GS}$ characteristics showing a large memory window and read-current ratio; (d) photograph of a 30 × 30 OPT memory array fabricated on a flexible PET substrate (the inset shows a zoomed-in image of the array); and (e) photograph of a butterfly image stored on top of the flexible memory array (reprinted with permission from Chen *et al.*,[62] copyright 2016, American Chemical Society).

on an ITO-coated 5 × 5 cm^2 PET substrate. This bendable active-matrix array was utilized to measure the spatial distribution of the incident UV light and to store an analogue image. The resetting and programming was performed in a similar fashion by UV irradiance (365 nm, 100 μW cm^{-2}), while erasure was performed using a gate pulse. The lights were applied in the shape of a butterfly (Fig. 4e), and an evident shape was observed for up to 24 hours after removing the light and applied voltages. The results obtained by Chen *et al.* show the great potential of flexible OPT memories in practical applications involving environmental monitoring and health care.

1.3.2 OFET chemical sensors. Initial contributions to OFETs as chemical sensors were made in the late 1980s.[63–65] OFET chemical sensors are particularly advantageous because of their cost-effectiveness, real-time processability, and portability.[66–69] These devices are commonly fabricated using the bottom-gate approach (as illustrated in Fig. 1) since it enables direct OSC/analyte interaction. The working principle of OFET chemical sensors relies on the analyte-induced changes in electrical characteristics of OFETs, which can be affected by the morphology and/or energy levels of the corresponding OSC and analyte.[70] One of the main advantages of OFETs is that multiple parameters (μ_{FET}, I_{on}/I_{off}, and V_T) can be used to evaluate their sensing performance. This multi-parametric approach was first introduced in 2000 in an effort to characterize the response of an OFET to a given gaseous analyte.[71,72]

In addition to the three above-mentioned parameters, change in the OSC conductivity can also provide important insight into the sensing performance, which can be measured using an equivalent two-terminal configuration. Indeed, the multi-parametric response feature of OFETs has been reported to yield highly sensitive chemical sensors.[73] Similarly, OFET chemical sensors are also known to show enhanced recovery behavior after the sensing activity is completed. Essentially, the charge carriers trapped as a result of the interaction between the analyte and the OFET can be detrapped by applying an opposite V_{GS}.[74,75] As a result, the OFET chemical sensors can be repeatedly used.

The sensing mechanism of OFET gas sensors stems from the amenability of OSCs to noncovalent π-interactions. The interaction between the OSC and analyte molecules can occur at the surface of the OSC film or at the grain boundaries in the bulk of the OSC film. At the same time, the analyte molecules can even reach the I/S interface or the metal/OSC interface by percolating through the voids between the OSC grains. The interaction can be detected electrically, intrinsically (*via* 2D conductivity of the OSC layer), and extrinsically (*via* V_T, μ_{FET}, and I_{on}/I_{off} of the OFET device). In certain cases, the analyte exposure induces a shift of V_T, which depends on the analyte redox properties.[76,77] This behavior corresponds to the sensitivity of V_T to carriers injected/extracted from the OSC layer. Since OSCs typically demonstrate an electron-rich conjugated system, they show sensitivity to strong oxidants like nitroaromatic compounds and nitric oxide (NO), which act as electron acceptors and either trap charge carriers or dope the OSC layer. This results in an increase in I_D and positive V_T shift in p-type OSC materials. Some studies have proposed that the sensing mechanism originates from enhanced accumulation of holes due to oxidation of the OSC[77] or from the electron traps owing to the reduction of analyte near the I/S interface.[78]

In case of the detection of chemicals secreted from the human body, Liu *et al.* have demonstrated the development of nanoribbon semiconductor-based wearable sensors.[79] In these transistors, the source and drain electrodes were modified with glucose oxidase (GOx), chitosan, and single-walled carbon

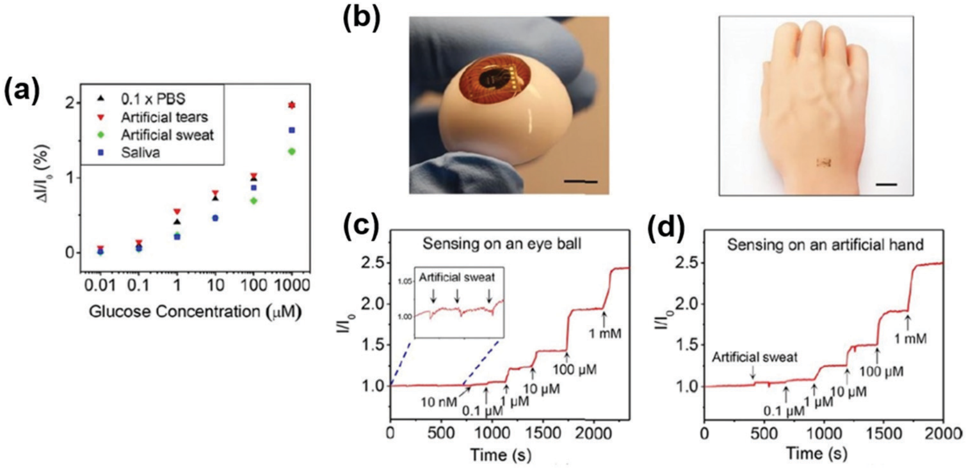

Fig. 5 (a) Sensing response of the chitosan and SWNT-modified wearable sensors as a function of glucose concentration in 0.1× PBS, artificial tears, artificial sweat, and saliva; (b) photographs of the sensors attached to an artificial eyeball and an artificial arm, the real-time response of the glucose level in the artificial sweat from the sensor attached in (c) artificial eye ball and (d) artificial hand (reprinted with permission from Liu *et al.*,[79] copyright 2018, American Chemical Society).

nanotubes (SWCNTs) using inkjet printing for the detection of glucose in human body fluids (tears, saliva, and sweat). The current responses of glucose in artificial human saliva, sweat, and tears are reproduced in Fig. 5a. At first, the baseline current was obtained by submerging the sensors in 0.1× phosphate-buffered saline (PBS). Sequentially, when the electrolyte was changed to human body fluids, a variation in the sensing response was observed (Fig. 5a). This variation was attributed to the pH difference between human body fluids and 0.1× PBS, which resulted in changes in the local electric fields (and eventually the conductance) of the sensors. To test on-body sensing capability, the sensors were attached to an artificial eyeball and an artificial arm (Fig. 5b). After connecting the artificial body parts to the measurement unit, artificial tears spiked with 0.01, 0.1, 1, 10, 100, and 1000 μM glucose were sequentially flowed (Fig. 5c and d). Overall, the authors demonstrated good sensitivity ranging from 0.1 μM to 1 mM. Among other applications, such results highlight the potential of this sensing platform to work as contact lenses for the detection of tear glucose levels.

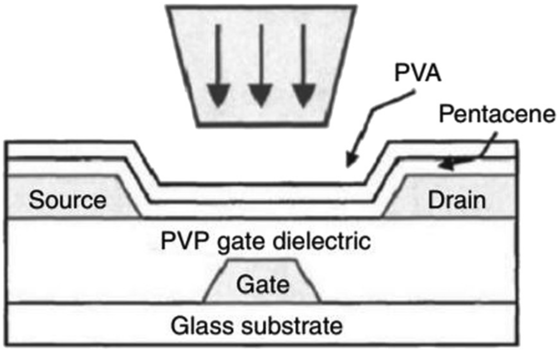

Fig. 6 Schematic illustration showing OFETs fabricated on a glass substrate and operating as free-standing pressure sensors (reprinted with permission from Darlinski *et al.*,[81] copyright 2005, American Institute of Physics).

1.3.3 OFET pressure sensors. In sensor devices where physical parameters (pressure or deformation) must be detected, the external stimulus is expected to reversibly affect one of the different layers of the sensor device, resulting in a variation of its electronic parameters (μ_{FET}, V_{T}, *etc.*). In the early reported OFET pressure sensors, the transistors themselves did not operate as the sensors but were used to address the matrix reading of the pressure signals from pressure-sensitive components. In 2004, Someya *et al.* reported on OFET-based pressure sensors as a tentative step toward the realization of an electronic artificial "skin".[80] The OFETs were used to address the flexible matrix, which was utilized to read out pressure maps from pressure-sensitive rubber elements. These devices could detect ∼10 kPa and had a response time of >100 ms. However, the high operating voltages (100 V) are unrealistic for electronic skin applications. In 2005, Darlinski *et al.* reported the pressure sensors where OFET itself acts as a sensor.[81] A mechanical force was applied on the OFETs using a motor-controlled microneedle (Fig. 6), and the applied pressures were measured while the devices were placed on a balance. The change in I_{D} as a function of induced force was explained to be a consequence of the variation in the distribution of trap states near the I/S interface. The main disadvantage of these devices was related to the use of nonflexible (glass) substrates, which limit their use in wearable applications like e-skin.

With recent progress regarding OFET pressure sensors, innovative methods have been developed to realize high-performance sensor devices on flexible substrates. For instance, Mannsfeld *et al.* and Schwartz *et al.* have reported on flexible pressure-sensor platforms in which the sensitivity of the OFET devices relied on the use of the polydimethylsiloxane (PDMS) gate insulator.[10,82] The regularly structured and compressible rubber insulator (PDMS) was the main component leading to high-pressure sensitivity in these devices. In addition, PDMS is well-known for its biomedical amenability with human tissue,[83] which made it a favorable choice since the authors were particularly

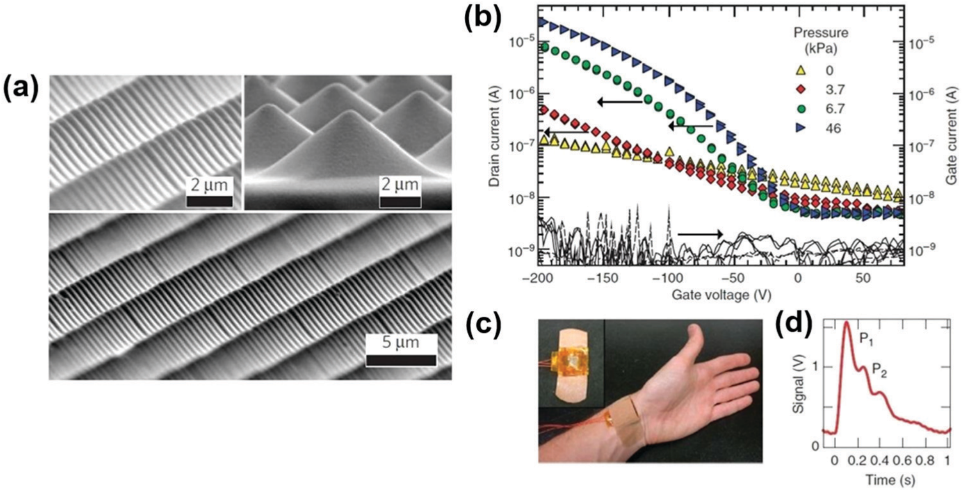

Fig. 7 (a) Scanning electron microscopy images of the PDMS thin films. Pyramidal arrays were etched into the faces of Si-wafer molds to form two-dimensional arrays of square pyramids (reprinted with permission from Mannsfeld *et al.*,[10] copyright 2010, Nature); (b) I_D–V_{GS} characteristics of flexible OFET sensors as a function of different applied external pressures; (c) an image showing a pressure sensor attached to a person's wrist; and (d) output signal of radial artery pulse measurement averaged from 16 periods. V_{DS} and V_{GS} were −100 V, and $I_D < 10$ mA (reprinted with permission from Schwartz *et al.*,[82] copyright 2010, Nature).

aiming for application in health monitoring and artificial skin. Before applying as the insulator layer in OFET devices, the PDMS thin films were microstructured with pyramid-shaped features (Fig. 7a).[10] The resultant PDMS film consisted of voids that enabled the micro-structured surface to elastically deform when external pressure was applied. The external pressures to the OFET sensors were applied and measured with a motorized z-stage in combination with a force gauge, which resulted in an increase in I_D. This behavior was explained as a result of the compression of the PDMS layer, which reduced the layer thickness, thereby increasing the gate capacitance and I_D. The transfer characteristics of OFET sensors at different pressure loads are reproduced in Fig. 7b. In this case, polyisoindigobithiophene-siloxane (PiI2T-Si) was used as the OSC.[82] These flexible sensors revealed a sensitivity of 8.4 kPa^{-1} and response time of <10 ms. To validate the functionality of the OFET sensors in a bending state, the authors performed radial artery pulse wave measurements, wherein the pressure sensor was attached to the wrist (Fig. 7c). The measurements were conducted in the motorized z-stage while the sensor was operated at constant V_{GS} and V_{DS}. Fig. 7d shows the pulse wave averaged over 16 periods. The first two peaks, $P_1(t_1)$ and $P_2(t_2)$, can be used to derive the two most frequently used parameters for arterial stiffness diagnosis (the radial augmentation index $AI_r = P_2/P_1$, and the time delay between the first and second peaks $\Delta T_{DVP} = t_2 - t_1$[84]). For the test subject, the authors extracted the AI_r and ΔT_{DVP} values as 59% and 155 ms, respectively,[82] which are considered healthy for an adult male in his mid-thirties.

Considering the importance of the development of wearable pressure sensors for emerging artificial intelligence and healthcare systems, Zang *et al.* developed suspended-gate OFETs.[85] The devices were fabricated in the TGBC architecture on flexible PET substrates using poly(diketopyrrolopyrrole-terthiophene) (PDPP3T) as the OSC layer. Strips of polyimide tape were laminated onto the substrates and used as supports to form the suspended gate. The polyimide/Al foil was then transferred to the support and fixed with tapes (Fig. 8a and b). A force gauge and a configurable motorized stand were utilized to apply and measure the external pressure (Fig. 8c). The sensing mechanism in these devices was explained as a result of the deformation of the gate when subjected to an external pressure. This modifies the capacitance of the gate insulator layer as a function of the applied pressure, thereby resulting in a pressure-dependent I_D (Fig. 8d and e). Sensitivity in this case is expressed as:

$$S = \frac{\Delta I}{I_0 \Delta P}, \tag{5}$$

where ΔI denotes the relative current change, I_0 denotes the initial sensor current without pressure loading, and ΔP gives the change in applied pressure. The authors observed high sensitivities (>190 kPa^{-1}), which were found to be sufficient for radial artery pulse detection.[84] Furthermore, when these OFET pressure sensors operated at a low voltage of 6 V, a low power consumption of <100 nW was achieved, highlighting their potential in wearable applications.

Yeo *et al.* reported on flexible OFET-based pressure sensors by combining a blend of small molecule OSC, 2,8-difluoro-5,11-bis(triethylsilylethynyl)anthradithiophene (diF-TESADT), and poly(methyl methacrylate) (PMMA) with an elastomeric top-gate dielectric, PDMS (Fig. 9a).[86] The OSC molecules were observed to vertically segregate and crystallize three-dimensionally at the apex of the PMMA baselines (Fig. 9b). The OFET pressure sensor was essentially prepared with two separate components. A top-gate component consisting of the PDMS elastomeric film was laminated to the bottom component of diF-TESADT:PMMA (Fig. 9c). The preparation of bottom component was performed by thermal deposition of Au source/drain electrodes onto the printed diF-TESADT:PMMA layer. To perform the sensor characterization, the authors used a probe station with a motorized stage to apply

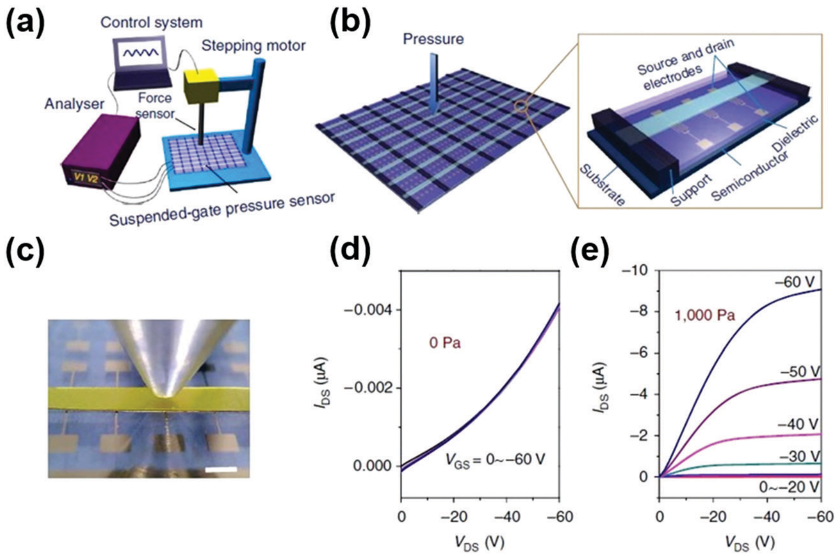

Fig. 8 (a) Schematic illustration of the experimental set-up of suspended-gate OFET pressure sensors; (b) an OFET array and magnified view of the device geometry; (c) optical image of a suspended-gate OFET (scale bar corresponds to 1 mm); I_D–V_{DS} curves of the transistors recorded at (d) 0 Pa and (e) 1000 Pa (reprinted with permission from Zang *et al.*,[85] copyright 2015, Nature).

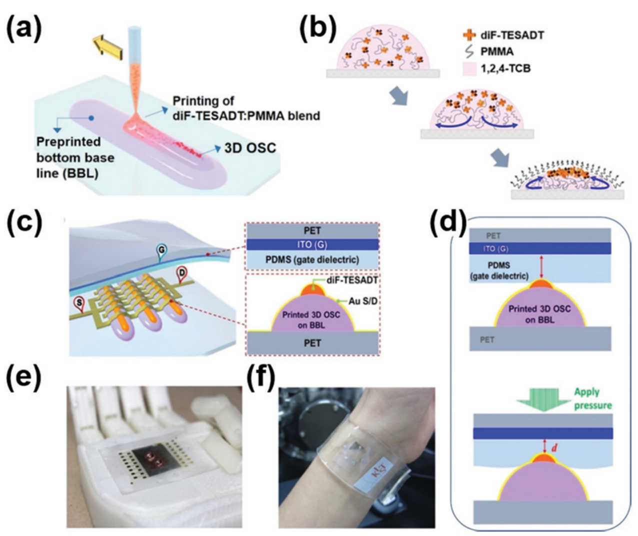

Fig. 9 Schematics of (a) the printing of the OSC:polymer (diF-TESADT:PMMA) blend solution on top of the preprinted PMMA baseline; (b) segregation and crystallization of the diF-TESADT molecules assisted by solvent evaporation; (c) flexible OFET pressure sensor in which the bottom component consists of a printed OSC structure, whereas at the top is the gate component consisting of an elastomer gate dielectric; and (d) pressure-sensing mechanism of the OFET sensor; photos (e) and (f) show OFET sensors attached to a prosthetic hand and around the wrist, respectively (reprinted with permission from Yeo *et al.*,[86] copyright 2017, American Chemical Society).

precise pressures, while a force gauge was used to measure the pressure-induced deformations, which were reflected by the change in I_D (Fig. 9d). The flexible pressure sensors yielded a pressure sensitivity of 1.07 kPa^{-1}, which was largely attributed to the change in capacitance of the gate dielectric layer originated from the pressure applied to the diF-TESADT layer. To demonstrate practical applicability of the flexible OFET sensors, the devices were tested in a prosthetic hand (Fig. 9e) and were utilized for the detection of the wrist artery pulse (Fig. 9f). In the case where the OFET sensor was attached to a prosthetic hand, a water droplet was dropped on top of the OFET sensor. The pressure load of the water droplet brought a change in the output current, and the sensors were found to detect pressures even below 20 Pa. Such results indicate the potential applicability of these sensors in healthcare monitoring and electronic skin applications.

In 2019, Liu *et al.* fabricated suspended-gate OFET-based pressure sensors on flexible substrates with poly(indacenodithiophene-*co*-benzothiadiazole) (PIDT-BT) as the OSC.[87] The devices consisted of patterned source/drain electrodes, whereas the gate structure (consisting of the gate electrode, the polyelectrolyte gate dielectric, and the polymer semiconductor) was kept at a distance of ~310 μm from the substrate by using a laminated thin tape (Fig. 10a). The pressure response was obtained by pressing the flexible gate structure of the OFET sensor, which led to the formation of an electrical contact between the polymer semiconductor and the source/drain electrodes. The authors reported high sensitivity values (452.7 kPa^{-1}), while the use of eco-friendly and nontoxic materials allowed the devices to be worn on human skin for spatial pressure mapping (Fig. 10b and c).

In a recent work, Baek *et al.* reported on OFET-based pressure sensors prepared on a biocompatible flexible parylene C substrate with poly(*N*-alkyl diketopyrrolo-pyrrole dithienylthieno[3,2-*b*]thiophene) (DPP-DTT) as the OSC.[88] The pressure-sensing capability of the devices was enabled *via* preparation of deformable source/drain electrodes by embedding conducting carbon nanotubes on the surface of microstructured PDMS which was integrated on top of a staggered OFET (Fig. 11a). The deformation of the electrodes on the polymer OSC layer modulated the channel geometry and contact resistance, resulting in pressure-dependent I_D and a high sensitivity of 18.96 kPa^{-1} (Fig. 11b and c). In this work, the authors also demonstrated a skin-attachable

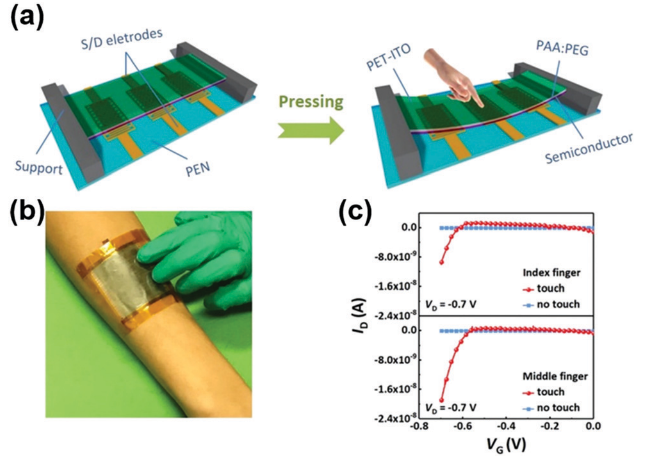

Fig. 10 (a) Schematics of the suspended-gate OFET pressure sensors, before and after the pressing of the flexible (suspended) gate structure; (b) photograph of the OFET sensor array affixed to a human arm; and (c) pressure-sensing response of the devices when touched using the index and middle fingers (reprinted with permission from Liu *et al.*,[87] copyright 2019, Wiley-VCH).

5 × 5 proof-of-concept active matrix transistor array (Fig. 11d) which highlights these devices as promising candidates for next-generation wearable electronic skin devices.

1.3.4 OFET temperature sensors. One of the achievements of the microelectronics industry is the cost-effective manufacturing of electronic gadgets and guaranteeing their widespread availability to millions of people around the world. However, one of the drawbacks of the commonly manufactured electronic gadgets (such as mobile phones and laptops) is related to their overheating.[89–91] To overcome this critical issue, the integrated system on chip concept is implemented by industries, which is specifically designed to handle the overheating issues and prevent gadgets from being damaged.[92,93] To support the function of this smart chip design, a robust and stable temperature sensor is required. However, most of the high-performance temperature sensors are based on inorganic materials that typically require high processing temperatures and show poor mechanical flexibility.[94–97] Thus, these issues stand as a barrier for employing thermal sensors to next-generation smart and flexible electronic devices.

Song *et al.* have recently demonstrated a P3HT-based OFET device as a flexible thermal sensor.[98] The proposed OFET devices were fabricated using the bottom-gate top-contact configuration, consisting of P3HT as the OSC, PMMA as the gate dielectric, and ITO-coated PEN as the flexible substrate (Fig. 12a). It is important to note that the solvents used for P3HT/PMMA bilayer formation (toluene/chlorobenzene) are not orthogonal to each other. This, in turn, increased the probability of chlorobenzene attacking the P3HT active layer, which can result in the formation of a rough I/S interface. For this reason, the authors observed a positive threshold voltage for the p-type OFET device, as seen in Fig. 12b. Another important characteristic of this device is the deposition of a reasonably thick aluminum-coated flexible PEN substrate on

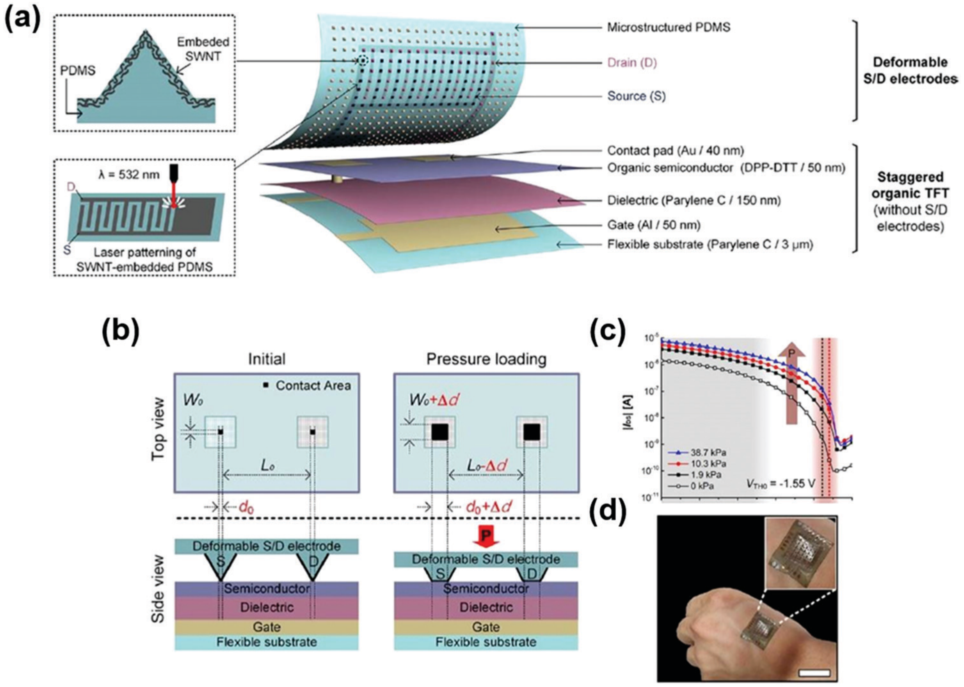

Fig. 11 (a) Illustration of an OFET-based flexible pressure sensor consisting of deformable source/drain electrodes integrated on top of a staggered OFET; (b) schematic illustration of OFET pressure sensors demonstrating parameter changes when pressure is applied. Pressure application results in an increase of W from the initial width W_0 to $W_0 + \Delta d$, while L decreases from the initial length L_0 to $L_0 - \Delta d$. This leads to an increase in the channel geometrical parameter, resulting in the pressure dependence of I_D; (c) device transfer characteristics as a function of applied pressures; and (d) photograph of the flexible OFET array on the back of a human hand as a proof-of-concept of wearable electronic skin; scale bar corresponds to 2 cm (reprinted with permission from Baek *et al.*,[88] copyright 2019, American Chemical Society).

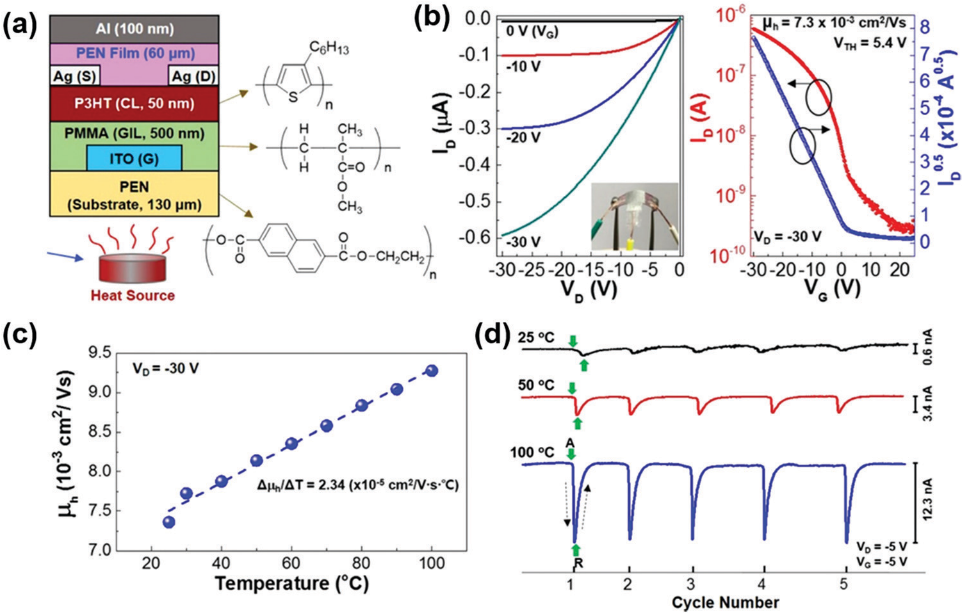

Fig. 12 (a) Schematic representation, (b) output and transfer characteristics of the fabricated OFET thermal sensor, (c) relation between charge carrier mobility of the sensor and ambient temperature, (d) drain current response of the sensor for different temperatures (reprinted with permission from Song *et al.*,[98] copyright 2017, American Chemical Society).

top of the device architecture. This was done to avoid the effect of ambient light on the photosensitive P3HT material.

The temperature-sensing properties of the proposed device were investigated by measuring transfer and output characteristics at different temperatures ranging between 25 and 100 °C. The I_D and μ_{FET} showed a gradual and steep increase with temperature (Fig. 12c). Based on these results, the authors investigated the robustness and repeatability of the proposed flexible thermal sensor, the results of which are presented in Fig. 12d. The drain current was observed to increase rapidly and decline relatively more slowly when the temperature source was near and far from the device, respectively. Finally, the as-fabricated flexible thermal sensor was attached to the finger for demonstrating its real-time sensing behavior. Interestingly, the drain current of the sensor remained stable enough while it was attached to the finger. In addition, the instantaneous increase in I_D when the sensor was attached to the finger was successfully retrieved after the detachment. Hence, the proposed versatile polymer-based flexible thermal sensor was shown to be robust and mechanically flexible and demonstrated good temperature-sensitive properties. These characteristics make it a good candidate for many artificial skin-related applications.

One of the significant drawbacks of the sensor devices proposed by Song *et al.* is the requirement of a high operating voltage. This limits the integration of these devices in wearable healthcare-based applications.[99–101] Some of the important requirements expected from a thermal sensor in medical industries are high temperature sensitivity with extremely high resolution, mechanical flexibility and robustness, and the capability to continuously monitor the temperature changes for an extended period of time.[102–104] Many researchers have addressed these requirements with innovative solutions based on either resistive- or capacitive-based temperature-sensing devices.[105–107] However, one of the problems in adapting these available solutions for the target market is related to their inherent poor sensing resolution and the utilization of nonflexible substrates. Furthermore, in addition to the usage of devices based on single parameters such as resistance and capacitance, the concept of employing a multi-parametric OFET approach constitutes an interesting choice.

Mandal *et al.* have recently reported on flexible OFET sensors in which hexagonal barium titanate nanocrystals (h-BTNC) served as the temperature-sensing layer with PDMS encapsulation.[108] The device architecture, as seen in Fig. 13a, was composed of h-BTNC + Al_2O_3 as the gate dielectric and pentacene as the OSC. It is worth noting that the bilayer dielectric combination was proposed for realizing two important requirements: low operating voltage and low gate leakage current. Interestingly, for the first time, the h-BTNC material was synthesized at low temperatures, of around 60 °C, to achieve nanocrystal morphology, which can significantly reduce the roughness of the surface, thereby improving the quality of the I/S interface. As seen in the transfer characteristics (Fig. 13b), the devices demonstrated a low V_T, of about −1.05 V, which was attributed to the combination of h–BTNC and Al_2O_3 as a gate dielectric material. In addition to this, μ_{FET} and I_{on}/I_{off} were found to be around 1.46 cm^2 V^{-1} s^{-1} and 10^3, respectively.

The authors initially performed stability tests on the as-fabricated flexible OFET device. As observed in Fig. 13c, μ_{FET} slowly decreased over a testing period of 200 days. To improve the stability, the device was encapsulated by a thin PDMS layer. The real-time response and recovery behavior of the device was tested during inhalation and exhalation of air by a human subject while sensing a change in temperature. The results revealed that the

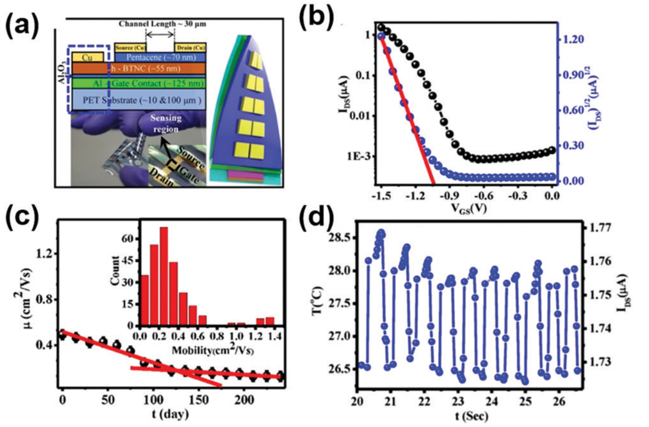

Fig. 13 (a) Pictorial representation and (b) transfer characteristics of a pentacene OFET thermal sensor. (c) Stability in terms of charge carrier mobility of the OFET device recorded for more than 200 days. (d) Repeatable thermal sensing performance of the pentacene OFET sensor (reprinted with permission from Mandal *et al.*,[108] copyright 2018, American Chemical Society).

devices were not only able to detect a change in temperature of about 2 °C but also exhibit quick response and recovery characteristics (Fig. 13d). Subsequently, many real-time tests were conducted by exposing the as-fabricated device in water, varied pH, and salt solutions. In all these cases, the as-fabricated device was able to sense the temperature with a high precision of around 4 mK over a narrow range of ambient temperatures ranging between 20 and 50 °C. In summary, Mandal *et al.* reported a temperature sensor that incorporates the essential features such as low power operation and high precision with quick response and recovery behavior under versatile environmental conditions. These features open various channels and opportunities for these devices to be used for various temperature-sensing applications.

1.3.5 OFET biosensors. A noninvasive, cost-effective, and consumer-compatible continuous health monitoring system is an ever-growing requirement in healthcare industries.[113] In this context, one of the important strategies is the noninvasive probing of target analytes from fluids to understand the metabolic activities in the human system.[114–116] This strategy has been used as a vital tool for designing and implementing wearable biosensing systems. Considering the importance of lactate as one of the important biomarkers for monitoring the physical conditions of human beings, Minamiki *et al.* have developed a low-cost and wearable lactate-sensing platform using an ISFET device.[109] The as-fabricated device consists of three main blocks: the signal-amplifying DNTT-based ISFET device, the reference electrode, and the extended gate electrode. All these blocks integrated on a common flexible PEN platform can be seen in Fig. 14a, while the optical image of the as-fabricated flexible device is presented in Fig. 14b. The ISFET exhibited a p-type behavior with moderate μ_{FET} and $I_{\mathrm{on}}/I_{\mathrm{off}}$ of around 0.10 cm^2 V^{-1} s^{-1} and 10^3, respectively. As shown in Fig. 14c and d, the rigorous DC bias stress and lactate-sensing cycle tests revealed good operational stability of the ISFET, which makes it a suitable candidate for continuous monitoring.

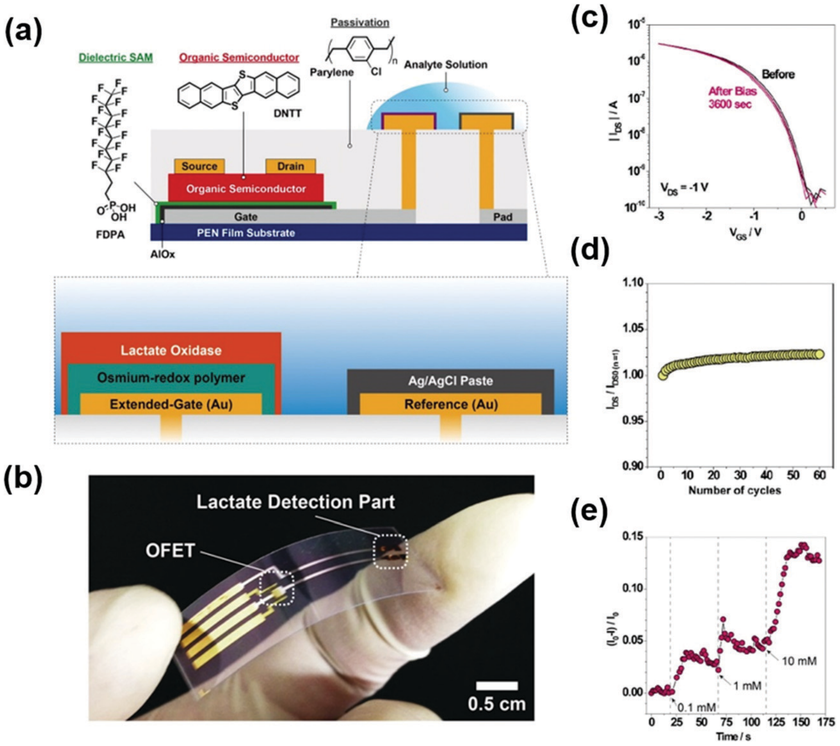

Fig. 14 (a) Schematic representation and (b) photograph of a flexible OFET device; effect of bias stress, (c) transfer behavior of one cycle and (d) current response toward 60 cycles; (e) transient drain current response of flexible OFET device toward different lactate concentrations (reprinted with permission from Minamiki *et al.*,[109] copyright 2019, Analytical Sciences).

The whole device architecture consists of a reference electrode (Au/Ag/AgCl) and three vertically stacked layers of Au/osmium-redox polymer/lactate oxidase, connected with each other by the extended electrode. During lactate detection, the target analyte solution was drop-cast on the surface of both reference and extended gate electrodes. When V_{GS} is applied across the reference electrode, the osmium polymer in the extended electrode tends to reduce based on the concentration of lactate. This reduction process results in the formation of positive potential in the gate electrode of the OFET device. This positive gate voltage reduces the majority hole-charge carrier concentration in the DNTT channel region and results in a reduction of I_D. Hence, with the change in lactate concentration from 0.1 mM to 10 mM, Minamiki *et al.* observed that the magnitude of negative relative sensitivity increases with time (Fig. 14e). These results clearly show that the reported sensing device has the capability to sense lactate biomolecules at concentrations as low as 0.1 mM.

It must be noted that in this work, the authors have only used sweat samples for the detection of lactate. Similarly, no significant information was presented regarding the role of parylene-C in the flow cell arrangement. In early reports, researchers have proposed the use of PDMS because of its inherent immunity to many buffers. In the case of parylene-C, a commonly reported issue is related to the formation of pinholes smaller than 1 μm.[117] Under such conditions, the sensor platform is vulnerable to non-target analytes and may influence the outcome. Essentially, the pinholes alter the sensitivity of the device by absorbing the anlayte and thereby reducing the limit of detection (LOD) (due to reduced concentration of the actual analyte interacting with the gate electrode).

The sensitivity and detection limit toward lactate are improved by increasing the sensing area and removing the reference electrode part in the extended gate section.[110] In addition to this, previously used DNTT material was replaced by a PbTTT-C16 organic semiconductor to improve the device stability and transistor performance. To achieve large scale production, authors have adopted a cost-efficient screen printing technique to print the proposed extended gate based organic field-effect transistors on plastic substrates. The synergistic combination of aluminium/aluminium oxide as gate/gate-dielectric with tetradecylphosphonic acid as an SAM layer played a crucial role in reducing the operating voltage of the device to less than 2 V. The device also exhibited extremely good selectivity toward lactate against other common interferents. This is mainly due to the tailor-made receptor layer composed of both horseshoe peroxidase and osmium redox polymer, and they are functionalized on top of the extended gate. This receptor layer specifically binds with the target lactate species to improve the selectivity of the device. With these specific improvements, the authors were able to augment the LOD to 60 nM which is around 40 nM lower than the previously reported one. Therefore, Minami *et al.*[110] have successfully developed a room-temperature operating, mass-scale production feasible, highly sensitive, selective and extremely flexible lactate sensor.

A step forward for early detection of Parkinson's disease is to develop an on-site monitoring compatible dopamine biosensor. This sensor must be able to detect a wide range of dopamine concentrations ranging from μM to aM depending on different aqueous media. By considering these requirements, for the first time, Jungkyun *et al.*[111] have developed a liquid-ion-gate organic field-effect transistor (LIG-OFET) based dopamine sensor using the enzyme-free approach. In the beginning, the CVD process was used to grow high-quality graphene on top of a flexible PEN substrate. The reason for choosing graphene is to facilitate the immobilization of Pt nanoparticle decorated reduced graphene oxide (Pt-rGO). This immobilized material acts as a receptor layer to specifically bind with the target dopamine analyte. Then, the non-conventional combination of PANI:CSA material was screen printed as the source and drain contacts. The classical buffer solution PBS is deposited on top of the Pt-rGO immobilized substrate to serve as a liquid ion gate dielectric. To evaluate the sensing behavior, the fabricated LIG-OFET was tested toward different dopamine concentrations. As a result, the sensor exhibited a good linear range from 100 aM to 10 nM. Moreover, the sensor was able to selectively detect the target dopamine against other commonly found interferents. High sensing performance on a good flexible substrate of the demonstrated dopamine sensor can be easily integrated to develop wearable and portable sensors.[111]

Recently, Khan *et al.*[112] have successfully developed a flexible organic field-effect transistor-based biotin sensor. One of the critical challenges faced by the authors is to improve the aqueous stability of the pentacene based OFET device, which is crucial to detect the target biotin analyte. Interestingly, a water-stable CuPc organic semiconductor was deposited on top of an active pentacene layer to serve as a passivation layer. In addition to this, the water stable polymer played an important role in electrostatically attracting but not specifically binding the target biotin molecules from the aqueous medium. Initially, the electrical characteristics of the OFET device was recorded under ambient conditions. The charge carrier mobility of the fabricated organic transistor on a flexible substrate was measured to be around 0.8 $cm^2\ V^{-1}\ s^{-1}$ at a low operating voltage of around -1 V. Afterwards, the device behavior was tested in the presence of freshly prepared PBS buffer solution. When compared to ambient conditions, there was a slight up-shift in both ON and OFF drain current levels with a small decrease in the charge carrier mobility. Due to the presence of CuPc in between the flow cell and pentacene channel layer, the device was showing exceptional stability in the presence of PBS buffer solution. After this, different concentrations of target biotin molecules were injected into the buffer solution and the corresponding changes in the drain current from the OFET device were recorded. As a result, the CuPc passivated flexible OFET device exhibited excellent sensitivity toward biotin with LOD measured around 200 nM concentration.[112] These ultra-flexible sensors can be integrated with the associated circuitry to develop low-cost wearable biosensors. The sensing performances of the above discussed OFET based flexible biosensors are compiled in Table 2. In summary, the authors reported a flexible, reliable, low-power, and highly sensitive lactate sensor that acts as a competitive candidate for noninvasive continuous health monitoring applications.

Table 2 Materials used for biosensing and their parameters in as-fabricated devices

Material	Bio-analytes	Sensitivity	Biasing condition	Limit of detection	Media used	Flexibility limit
9	Lactate[109]	No information	V_D[a] = −2.5 V, V_G[a] = −2.5 V	0.1 mM	PEN[a]	60 bending cycle tests
5	Lactate[110]	No information	$V_D = -1$ V, $V_G = -1$ V	66 nM	PEN	No information
11	Dopamine[111]	1% nM^{-1}	$V_D = 1$ V, $V_G = 10$ mV	100 am	PEN	No information
8	Biotin[112]	6 nA μM^{-1}	$V_D = -0.5$ V, $V_G = -1$ V	200 nM	Polyimide	No information

[a] V_G = gate voltage, V_D = drain voltage, V_{ref} = reference voltage, PEN = polyethylene naphthalene.

2. Semiconducting materials for flexible OFET sensors

Different OSCs are in use for OFET devices but for the purpose of flexibility these materials need to have various physical and electrical advantages to serve different applications. For example, they need to be sensitive enough for analytes even under strain conditions, rigorous application of external forces should not alter the dynamics in sensing and they should recuperate at faster rates in case of any deformation. In the following section, we have described the importance of OSC materials in different sensor applications. Typically, tuning material's properties not only brings more specificity and improved shelf-life but also can eventually help to reduce multi-faceted problems at the system level like power consumption and analyte classification.

2.1 Semiconducting materials for chemical sensors

2.1.1 Detection of gaseous pollutants. Gas phase pollutants emanating from automobiles, factories, and mines are one of the major causes of deaths in both developed and underdeveloped countries. Despite the strict actions to curb and limit such pollutants into the air, replacements exist that are equally dangerous as the original pollutants.[124,125] These include dangerous gases, volatile organic compounds (VOCs), and particulate matters (PMs), and chronic exposure to these can cause detrimental health effects. The sensing performances of the recently reported OFET based flexible chemical sensors are compiled in Table 3.

One such dangerous gas is ammonia; so Zhang *et al.*[118] have proposed highly transparent and flexible n-channel OFET-based devices for ammonia-sensing applications. They initially considered OSCs such as 13, 1, PBTTT-C12 (P1), and 10 (with reference to materials mentioned in Table 1) and investigated their electrical characteristics for different thicknesses or numbers of molecular layers. As depicted in Fig. 15a, the μ_{FET} of n-type material 13 stayed stable for the thickness ranging between a number of 10 and 4 molecular layers. However, the μ_{FET} rapidly decreased for polymer thickness less than 4 molecular layers. This sudden decrease in μ_{FET} may be due to the presence of trap states along the I/S interface region. Unlike material 13, by reducing the thickness from 60 nm to 4 nm, the μ_{FET} of n-type polymer P2 remains constant. Therefore, to achieve good transistor performance, an ultrathin polymer layer is preferred, which, in turn, reduces the surface roughness and supports the formation of a large grain size.

Fig. 15b shows the flexible and transparent ambipolar OFET device fabricated by depositing 4 nm of ultrathin n-type P1 polymer on the surface of 50 nm thick p-channel pentacene with PMSQ polymer as the gate dielectric layer. It is worth noting that the purpose of using an ultrathin layer of polymer is to enhance the interaction of target analytes with the polymer active channel layer at the I/S interface region. To emphasize this, ammonia gas-sensing studies were conducted for different thicknesses of P2 polymer active layers, as shown in Fig. 15c. In the case of an ultrathin film device, the sensitivity toward 100 ppm of ammonia was around one order of magnitude higher than the response of the thick film-based device. Moreover, comparatively, the ultrathin film-based device was able to sense ammonia down to a range of 10 ppm. Many researchers have reported that the utilization of ultrathin organic films is one of the most important requirements for achieving good sensitivities for various gas molecules.[126–129] Therefore, it is clear that the sensitivity is solely based on the architecture of the device and organic film morphology.

One of the most important issues in the proposed work of Zhang *et al.* is the use of the spin-coating technique, which has the potential to damage the surface and increase the roughness of some of the low-cost and commonly used polymer dielectric layers.[130] This can, in turn, affect the performance of the as-fabricated device. Based on this perspective, Yu *et al.* employed a spray-coating technique to deposit an ultrathin

Table 3 Materials used for chemical sensors and the sensing parameters

Materials	Analyte	Sensitivity	Voltage bias condition	Limit of detection (ppm)	Flexibility limit
1	NH_3[118]	I_{DS}[a]: 6.25%@10 ppm	$V_{GS} = 60$ V, $V_{DS} = 60$ V	10	No information
2	NH_3[119]	I_{DS}: 25%@100 ppm	$V_{GS} = -40$ V, $V_{DS} = -40$ V	10	No information
3	NH_3[120]	R_C[a]: 100%@0–1000 ppm	$V_{GS} = -5$ V, $V_{DS} = -5$ V	29	8.3 mm bending radius
4	NH_3[121]	I_{DS}: 82%@10 ppm	$V_{GS} = -5$ V, $V_{DS} = -5$ V	10	No information
5	NH_3[122]	I_{DS}: 2.8%@1 ppm	$V_{GS} = -5$ V, $V_{DS} = -5$ V	1	No information
6	H_2S[123]	I_{DS}: 400% [tensile stress]@1 ppm	No information	1	7 mm tensile and 15 mm compressive stress states

[a] I_{DS}: drain current; R_C: channel resistance.

Fig. 15 (a) Relationship between transistor parameters and the thickness of the active layers; (b) demonstrating the transparent properties of the as-fabricated device; (c) ammonia-sensing properties of thick and ultrathin film-based devices (reprinted with permission from Zhang *et al.*,[118] copyright 2013, Wiley-VCH).

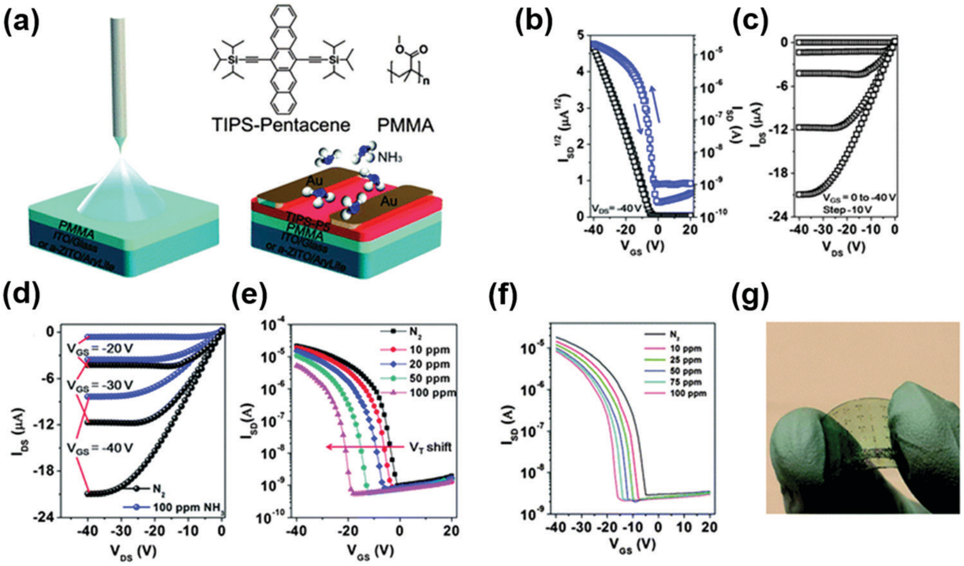

Fig. 16 (a) Schematic representation; (b and c) electrical characteristics; (d and e) ammonia-sensing behavior of the as-fabricated TIPS-pentacene on a glass substrate; and (f and g) ammonia-sensing behavior of the same device on a flexible substrate (reprinted with permission from Yu *et al.*,[119] copyright 2013, Royal Society of Chemistry).

layer of high-mobility TIPS-pentacene material on a commonly used PMMA gate dielectric material (Fig. 16a).[119] From the electrical characteristics (Fig. 16b and c), the as-deposited TIPS-pentacene devices showed p-type behavior with μ_{FET} and V_{T} of around 0.068 cm^2 V^{-1} s^{-1} and −4.2 V, respectively. By increasing the ammonia concentration from 0 to 100 ppm, the drain saturation current was reduced by four times, and V_{T} shifted negatively from −5 V to −20 V (Fig. 16d and e). This is because when ammonia interacts with an active layer, the incoming analyte tends to form charge trap sites, which significantly reduces the charge carrier concentration and mobility at the PMMA/TIPS–pentacene interface. Under 100 ppm of ammonia exposure, the response and recovery times of the sensor were around 10 and 240 s, respectively. Subsequently, transistor and sensing behavior of the devices was tested on Arylite/ZITO-based flexible plastic substrates. The μ_{FET} of the as-fabricated flexible device was measured to be around 0.0062 cm^2 V^{-1} s^{-1}. Moreover, the ammonia-sensing performance of the flexible device coincides with the response of the glass-based device (Fig. 16f). The photo-image of the as-fabricated device is presented in Fig. 16g. These results clearly show that the TIPS-pentacene-based OFET device is mechanically stable and has good sensitivity toward ammonia gas.

Important properties of OSCs, such as low-temperature processing, high mobility, and high environmental stability, are some of the ideal requirements for achieving reliable OFET-based gas sensors.[120] To satisfy these requirements, Ryu *et al.* used P-29-DPP-SVS, a donor–acceptor (DA) conjugated polymer, as the active sensing layer in an as-fabricated OFET (Fig. 17a).[120] The transistor and gas-sensing properties of the reported polymer were investigated by using two different device geometries (TGBC and BGTC, respectively) on two different substrates, namely glass and flexible PEN substrates. The μ_{FET} values were measured to be around 3.48 and 2.98 cm^2 V^{-1} s^{-1} on glass and flexible substrates, respectively. One of the important characteristics observed by the authors was the stability of these devices in both N_2 and air ambient environments (Fig. 17b). A reasonable explanation lies in the utilization of the top-gate geometry, which potentially served as an encapsulation layer, protecting the polymer OSC from environmental effects.[32,131–133] Subsequently, fabrication of devices

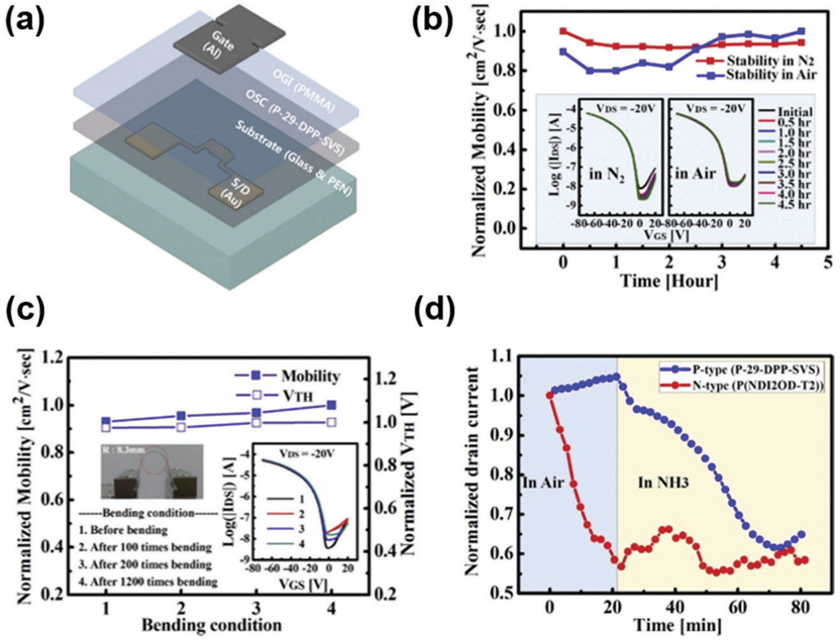

Fig. 17 (a) Schematic representation of a P-29-DPP-SVS-based OFET device. Relationship between the normalized mobility and the effect of (b) air and N_2 ambient, and (c) bending radius of the flexible OFET device. (d) Ammonia-sensing behavior of both p-type P-29-DPP-SVS and n-type (P(NDI2OD-T2)) materials (reprinted with permission from Ryu *et al.*,[120] copyright 2015, Elsevier B.V.).

on flexible PEN substrates was considered for investigating their mechanical stability. As seen in Fig. 17c, some of the parameters such as V_T and μ_{FET} remained constant even after 1200 bending sequences (bending radius: 8.3 mm). This clearly shows that the reported device is a good candidate for flexible platform-based applications.

To test the gas-sensing properties of the P-29-DPP-SVS-based OFETs (Fig. 17d), the devices were exposed to ammonia. It was observed that an increase in the concentration of ammonia from 29 to 1000 ppm results in a decrease of I_D and a negative shift of V_T. The sensing mechanism was further tested under ammonia exposure for both p-type P-29-DPP-SVS and n-type P(NDI2OD-T2) materials. The results revealed an abrupt decrease and a gradual increase in I_D for the p-type and n-type devices, respectively, which was attributed to the electron donor doping effect of ammonia.

Compared to the spin-coating method, deposition techniques with added advantages such as compatibility with industrial processing routes, large-scale production, and precise film thickness control are required to fabricate arrays of polymer-based flexible and transparent OFET architectures.[101,134] To fulfill this requirement, Khim *et al.*[135] reported the fabrication of ultrathin, uniform, and highly transparent devices based on p-channel (DPPT-TT) and n-channel (P(NDI2OD-T2))-based polymers. Devices were fabricated on flexible substrates with the help of a homemade bar coating solution-processed method. Primarily, the charge transport behavior of the reported polymers was investigated by embedding them as an active semiconductor layer in TGBC geometry. The results showed that the maximum μ_{FET} of DPPT-TT and P(NDI2OD-T2) is around 1.78 and 0.34 $cm^2 V^{-1} s^{-1}$, respectively, which decreased with their thickness. In contrast, the V_T of both polymers exhibited positive shifts by reducing their thickness. In addition, a BGBC device geometry on a PEN substrate was adapted for studying the gas-sensing properties of a DPPT-TT polymer. This study was performed by exposing the DPPT-TT-based device to ammonia (10 ppm), ethanol (1000 ppm), and ethylene (1000 ppm). In this case, the DPPT-TT polymer having a thickness of around 2 nm showed sensitivity toward ammonia of about 80%, which was 4 and 8 times greater than the respective responses of 5 and 12 nm-thick polymer-based devices. Nevertheless, one of the main issues in employing ultrathin polymers for sensing purposes is the poor stability of the OSCs.[135] Due to this issue, I_D showed a rapid decay over a short span of time when compared to their thick polymer counterparts.[135] Moreover, the proposed ultrathin device also tends to show significant sensing responses toward ethylene and ethanol vapors.

Notably, the devices reported above have two important setbacks—namely, low ambient stability and low selectivity toward target ammonia analyte. Hence, further development in this area would require careful optimization of the polymer film thickness without compromising the device performance.[135] This could eventually lead to a more robust sensing platform for ammonia and ethylene sensing, whereas the latter problem may be solved by employing fluorinated π-conjugated polymers.[136–138] One solution was proposed by Benjamin *et al.*, who reported on highly sensitive ammonia sensors.[121] The OFET sensors were prepared in BGTC geometry and were composed of an ultrathin PDFDT polymer as the active layer (Fig. 18a).

To augment the analyte–semiconductor channel interaction, ultrathin (<9 nm) poly(4-(4,4-bis(2-ethylhexyl)-4*H*-silolo[3,2-*b*:4,5-*b*′]dithiophen-2-yl)-7-(4,4-bis(2-ethylhexyl)-6-(thiophen-2-yl)-4*H*-silolo[3,2-*b*:4,5-*b*′]dithiophen-2-yl)-5,6-difluorobenzo[*c*][1,2,5]-thiadiazole) (PDFDT) active polymer was deposited with the help

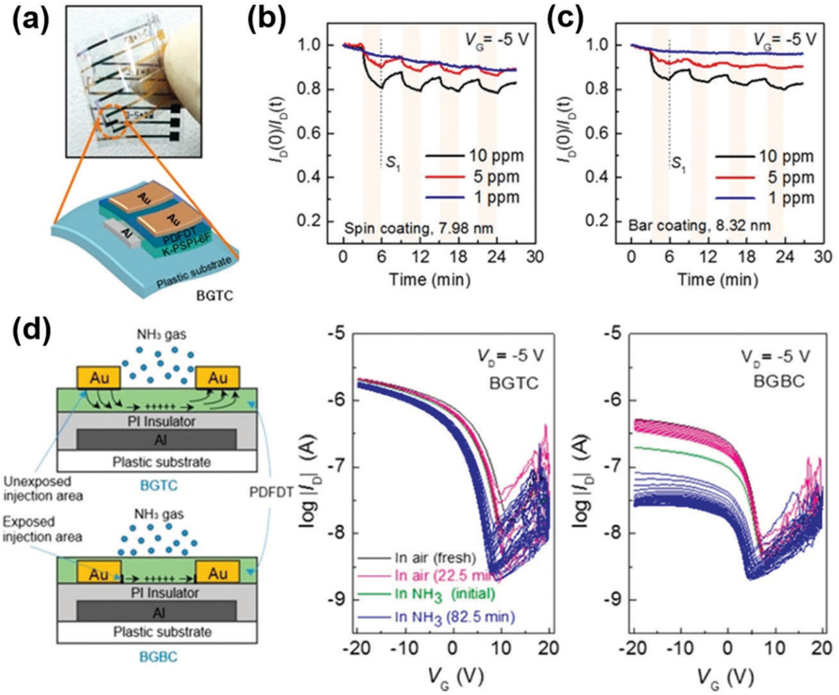

Fig. 18 (a) Schematic representation of PDFDT OFET sensor arrays on flexible substrates; (b) spin-coated and (c) bar-coated OFET sensing behavior to 10, 5, and 1 ppm ammonia gas; (d) ammonia-sensing mechanism and associated transfer behavior in BGTC and BGBC device geometry (reprinted with permission from Yawson *et al.*,[121] copyright 2017, American Chemical Society).

of both bar-coating and spin-coating techniques. The ammonia gas-sensing properties of the reported device were investigated at different exposure levels (10, 5, and 1 ppm). When compared to its bar-coating counterpart, the spin-coating-based OFET device showed good sensitivity of around 13, 5, and 1% for 10, 5, and 1 ppm, respectively (Fig. 18b and c). Under ammonia exposure, the density of the dominant hole charge carrier in the PDFDT OSC channel reduced, which affected the flow of the drain current. To understand the interaction between ammonia and PDFDT molecules, density functional theory (DFT) calculations were performed in three different modes of operations. The results showed that both hydrogen and electrostatic interactions were the two dominant effects that resulted in the sensing of ammonia gas vapors at low concentrations.

To understand the effect of different device architectures on sensing performance, two devices were fabricated in BGBC and BGTC geometries. As shown in Fig. 18d, the former device geometry showed a significant sensing response toward ammonia gas exposure when compared to its BGTC counterpart. This is because in the case of BGBC geometry, the area of the semiconductor exposed to the ammonia gas is relatively high. This, in turn, increased the trap density and, hence, the density of hole charge carriers at the I/S interface, influenced by the physically adsorbed ammonia gas molecules.

One of the drawbacks of most of the flexible gas-sensor reports that have been discussed is the absence of data regarding the effect of mechanical flexibility on gas-sensing performance.[118–121,135] This problem stands as a barrier for the commercial market in understanding the capability of a given flexible device for real-time sensing applications. To overcome this obstacle, Tang *et al.* studied the mechanical deformation effects of a dinaphtho[3,4-*d*:3′,4′-*d*′]benzo[1,2-*b*:4,5-*b*′]dithiophene (Ph5T2) single-crystal-based OFET device under H_2S gas exposure.[122] The devices were fabricated on PET substrates, while the single crystalline Ph5T2 layer was deposited on the surface of PMMA gate dielectric with the help of the vapor-transport method. The authors justified the use of Ph5T2 for testing gas-sensing properties because of its good electrical characteristics and ultrathin film formation capability with the added advantages of appreciable mechanical and environmental stability.[139,140] The reported device architecture is presented in Fig. 19a and b. In the first stage of investigation, the effect of substrate bending on the electrical characteristics of the OFET device was studied. This study showed that the drain saturation current decreased steeply and slowly ramped up under tensile and compressive states, respectively. Under non-stress conditions, the μ_{FET} of the device was measured to be around 0.07 cm^2 V^{-1} s^{-1}, which is about seven times greater and four times smaller than the tensile and compressive counterparts.

Subsequently, the effect of stress conditions on the device's gas-sensing behavior under exposure of H_2S gas was investigated. As shown in Fig. 19c, under 1 ppm H_2S gas exposure, the device with high tensile stress exhibited good sensitivity of around 400%, which is approximately 10 times greater than the response from compressive and non-stress state conditions. Moreover, the authors also performed a selectivity study by exposing the testing device to three different gases: NO (25 ppm), NO_2 (10 ppm), and H_2S (5 ppm). Among these, the device responded to H_2S with a sensitivity of around 438%

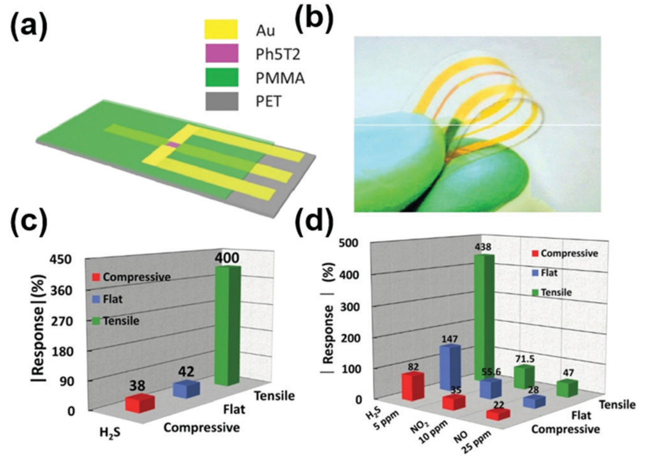

Fig. 19 (a) Schematic representation and (b) camera image of a Ph5T2 flexible OFET device. Effect of compressive, flat, and tensile stress on the response of the flexible OFET in the presence of (c) 1 ppm H_2S and (d) 5 ppm H_2S, 10 ppm NO_2, and 25 ppm NO (reprinted with permission from Tang *et al.*,[122] copyright 2017, IEEE).

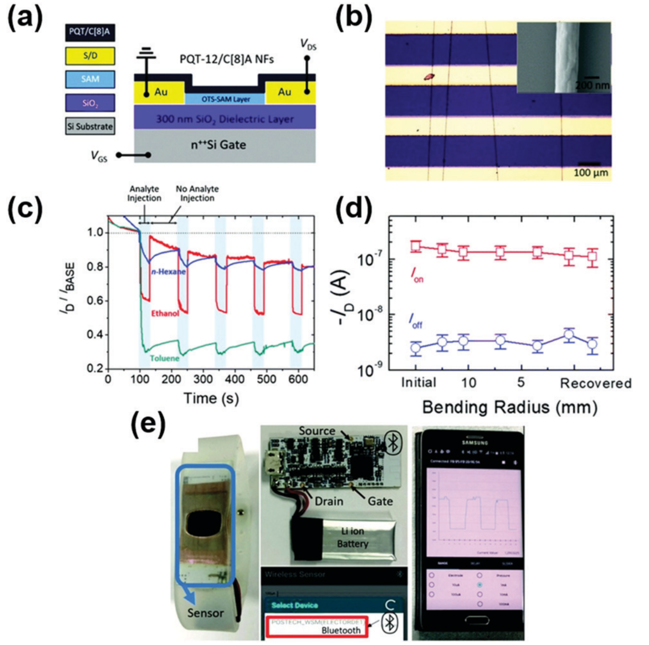

Fig. 20 (a) Schematic illustration of a PQT-12/C[8]A NF-based OFET device; (b) optical image along with SEM (inset) image of nanofibers; (c) transient response toward *n*-hexane, ethanol, and toluene vapors; (d) effect of bending radius on both "off" and "on" current of the device; (e) real-time demonstration of the OFET sensor for an IoT-based monitoring system (reprinted with permission from Kweon *et al.*,[123] copyright 2019, Royal Society of Chemistry).

under compressive stress conditions (Fig. 19d). The study by Tang *et al.* clearly depicts the effect of different stress conditions on the sensitivity of the device to H_2S gas. The proposed device showed good mechanical flexibility, high sensitivity, and selective H_2S gas-sensing capability. These features highlight the suitability of the reported device for future flexible and wearable electronics applications.

To improve the sensitivity and selectivity of target analytes, one of the important factors to account for is the efficient interaction between the analyte and OSC materials. This interaction mechanism is mainly guided by two important parameters: the aspect ratio of the sensing layer and the availability of functional groups for selective interaction with target analytes.[141,142] These requirements triggered Young *et al.* to propose the combination of nanostructure and surface functionalization strategy for augmenting the sensing performance of flexible and transparent sensing devices.[123] Formation of nanofibers in a polymer solution may be considered a challenging task, especially with an electro-spin deposition technique.

Thus, Young *et al.* started with the investigation of sensing capability by using a synergistic combination of PQT-12 nanofibers and polyethylene oxide (PEO). In this work, OTS-modified Si/SiO_2 substrates were utilized, and Au source/drain contacts were patterned on top using conventional photolithography. Subsequently, an organic polymer solution was prepared by blending PQT-12, calix[8]arene and poly(ε-caprolactone) molecules, which served as the active material, functionalizing agent, and high molecular weight polymers, respectively. The resultant solution was carefully electro-spun, with optimized parameters on the surface of the as-fabricated device to obtain PQT-12-based nanofibers. The schematic representation and the optical micrograph of the as-fabricated device are presented in Fig. 20a and b. The electrical properties of both p-type PQT-12 and PQT-12/calix[8]arene OSC-based devices were performed and tabulated. In principle, the nanofibers protrude out of the surface of the sensor device and can readily interact with the incoming analytes. The calix[8]arene-functionalized device exhibited higher hole mobility and V_T when compared to its pristine PQT-12 counterpart.

The chemical-sensing properties of PQT-12/calix[8]arene were tested under different electron-donating VOCs such as ethanol, *n*-hexane, and toluene. Toward these VOCs, the device exhibited a negative relative sensitivity trend, as shown in Fig. 20c. This is because, under VOC exposure, these electron-donating vapors tend to trap the majority hole-charge carriers from the active OSC. Consequently, I_D is reduced, which contributes to negative relative sensitivity. With the addition of calix[8]arene molecules, the host PQT-12 materials tend to show good sensitivity for ethanol and toluene of around 192% and 229%, respectively, when compared to counterpart *n*-hexane. This response can be attributed to the improved physical adsorption of the exposed analytes on the surface of calix[8]arene receptor layers, which significantly affected the I_D of the as-fabricated device. Subsequently, the PQT-12-based flexible sensing device was fabricated, and its electrical behavior was tested as a function of the bending radius. As seen in Fig. 20d, by increasing the bending radius from 0 to 12.5 mm and then releasing it back to the normal condition, I_{on} and I_{off} remain constant at 10^{-7} A and 10^{-9} A, respectively. Moreover, the effect of bending was found to be negligible on the chemical-sensing response of the modified PQT-12 flexible sensor device. This clearly shows that the reported flexible device exhibits not only good mechanical stability but also exceptional operational stability.

In addition, the authors also demonstrated the use of a flexible sensor for ethanol detection and wireless transferring of data to a smartphone with the help of customizable data processing board (Fig. 20e). However, one of the drawbacks of this work is related to the use of SiO_2 as the gate dielectric, which significantly increased the device's operating voltage. This would eventually require frequent battery recharge as the whole setup is based on a Li-ion battery. One viable solution is the utilization of a high-κ dielectric that guarantees low power consumption. Nevertheless, the reported flexible device is a good product to match the current requirement in smart sensing applications. The reported sensor has some of the important properties—namely, good stability under ambient conditions and high chemical-sensing capability—which makes it a suitable candidate for IoT smart-sensing applications.

2.1.2 Humidity sensor. Historically, a humidity-sensing mechanism was proposed around two centuries ago, based on the conduction of protons during the physical adsorption of water molecules on the surface of active materials.[143,144] Owing to their good thermal and operational stability, metal oxides, such as Al_2O_3,[145–147] In_2O_3,[148–150] SnO_2,[151–156] and TiO_2,[157–162] are typically preferred materials for this kind of sensing. One of the important morphological parameters achieved in all the explored oxide-based humidity sensors is porosity, which effectively improves the adsorption of water molecules on the surface of oxide layers.[154,160] However, the intrinsic limitation of using metal oxides for humidity-sensing applications is that usually high temperatures are required to achieve good sensing performance.[143] A viable solution is the use of conjugated polymers that can be processed at room temperature, thus facilitating the development of next-generation smart humidity sensors.[163,164] In the case of polymers, three commonly reported transducing mechanisms are chemiresistive,[165] chemi-capacitive,[166] and OFET[167,168] based concepts. The devices based on the first two concepts are relatively simple to fabricate. In either case, the complete sensing performance rests within a single parameter, which stands as a barrier to understand the detailed humidity-sensing mechanism of the employed active material. Alternatively, transduction based on an OFET device promises the characterization of humidity-sensing performance with the help of many parameters such as I_D, V_T, I_{on}/I_{off}, and SS.[167,168] Moreover, an OFET-based transducing mechanism is one of the preferred solutions for augmenting sensitivity to humidity analytes.

The common sensing mechanism proposed in the majority of the reported literature follows three important steps: (1) physical adsorption of humidity analyte at the interface between air and the organic layer, (2) diffusion of analyte molecules from the OSC surface to the I/S interface, and (3) the modulation of charge carrier density at the I/S interface and consequent variation of the OFET electrical behavior. However, the sensitivity of the device mainly depends on the efficiency of the second step in the proposed mechanism. To improve this efficiency, the utilization of ultrathin OSC films has been suggested to augment the interaction between the analyte and the OFET I/S interface. Nevertheless, the main bottleneck in the proposed solution is related to poor mechanical stability.[169,170] To overcome this, Park *et al.* reported ultrasensitive humidity sensors with the help of a unique sensing mechanism based on an analyte-induced doping phenomenon.[171] In this work, the authors considered Si/SiO_2 substrates for the device fabrication process. The unique part of this study was the inclusion of a polyelectrolyte layer whose electrical conductivity changed with respect to the ambient humidity condition.

The important aspect addressed by the authors is related to the diffusion of analytes into the sensing medium.[171] They adopted a supporting material into the system that can enhance the diffusion of the analyte to the I/S interface. The dielectric polyelectrolyte layer was spin-coated and successfully sandwiched between the top OSC layer of pentacene and the bottom dielectric layer of SiO_2. The transistor behavior of the as-fabricated device was tested under different humidity conditions. It was observed that the response improves due to the enhancement of ion migration in the polyelectrolyte upon absorption of moisture. The transfer characteristics showed a linear increase in I_D from 10^{-11} to 10^{-4} when the humidity was increased from 0 to18% (Fig. 21a). This increase in I_D was attributed to the release of negative chlorine ions triggered by humidity. Due to the electrostatic effect, these free chlorine ions tend to attract the majority of hole-charge carriers at the polymer/polyelectrolyte interface. As a result, the hole-charge carriers facilitate the increase in I_D, as shown in Fig. 21b. In addition to this, as shown in Fig. 21c, the as-fabricated device showed good repeatability and reliable performance with exceptional response (10 s) and recovery (40 s) times.

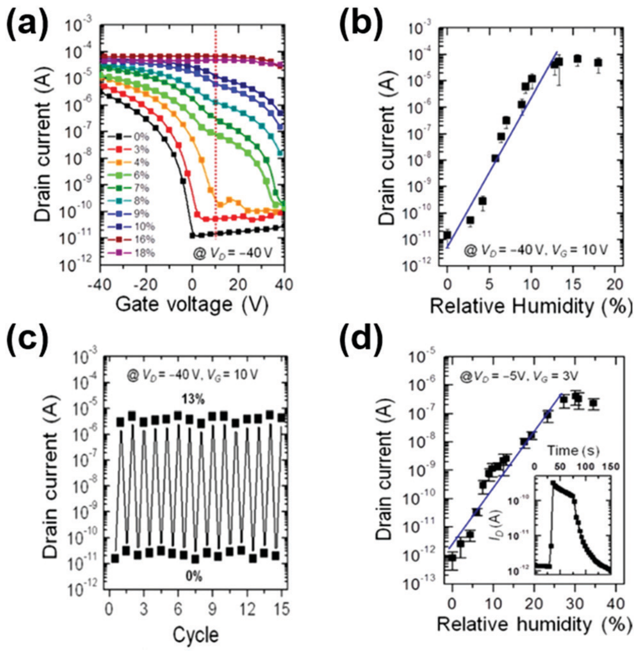

Fig. 21 (a) Effect of different humidity levels on the transfer behavior of an OFET device. At V_D = −40 V and V_G = 10 V, (b) relationship between the device drain current and humidity, and (c) repeatable behavior of the device toward 13% humidity. (d) Flexible OFET device behavior and (inset) transient response toward different humidity levels at V_D = −5 V and V_G = 3 V (reprinted with permission from Park *et al.*,[171] copyright 2013, American Chemical Society).

To develop a transparent and flexible sensor, the rigid Si/SiO_2 substrate was replaced by a flexible PEN substrate. In this case, alumina was employed as the gate dielectric, whereas graphene was used as the top source/drain contact electrode. Because of the use of high-κ dielectric materials, the operating voltage of the devices drastically decreased by ten times without compromising the unique sensing performance. An interesting feature is the sensing window extension by impeding the Cl^- ions into the polyelectrolyte, which reduces the humidity interaction. Furthermore, the authors observed an abrupt increase in I_D at low humidity levels. In the case of alumina dielectric, the sensor window doubled as compared to SiO_2, and the current increased continuously up to a relative humidity of 30% as shown in Fig. 21d.

The integration of microelectromechanical systems (MEMS) with the standard OFET model is another novel strategy for augmenting the performance of a humidity-sensing device.[172,173] For instance, Thuau *et al.* have proposed a novel combination of organic MEMS cantilever and OFET-based transducer architecture as a humidity sensor.[174] Poling of the dielectric layer was achieved with the application of an electric field, which essentially helps in inducing the piezoelectric nature into the gate dielectric. Polarized devices can exhibit high sensitivity since this doubles the I_D current in comparison to a nonpolarized dielectric. The device's working mechanism is similar to a cantiFET[172] in that when there is a mechanical load, the cantilever bends, and the change in the piezoelectric property of the gate dielectric brings a change of the semiconducting channel.

The schematic and SEM images of the as-fabricated device presented by Thuau *et al.* are shown in Fig. 22a and b, respectively. The authors prepared a humidity-sensitive hydrogel layer and deposited it on the surface of the microcantilever. Under humidity exposure, the hydrogel layer initially tends to swell and develop strain on the surface of the cantilever, and the cantilever tends to oscillate due to the bilayer. This oscillation influences the piezoelectric gate dielectric, P(VDF-TrFE)/PVT polymer, to induce the polarization effect. This effect, in turn, influences the transistor channel properties and, hence, the drain current. As a result, the sensitivity and limit of detection (LOD) of the proposed humidity sensor was around 7500 ppm per % RH and 0.2% RH, respectively, as shown in Fig. 22c. Moreover, the reported humidity sensor exhibited good reversible and repeatable behavior under the humidity exposure levels ranging from 20% to 80%, as seen in Fig. 22d. The authors reported a high sensitivity of 607 for the combination of polarized P(VDF-TrFE)/PVT and pentacene; however, the combinations of DNTT, PMMA, and pentacene showed poor results. Similarly, the capacitor devices prepared with P(VDF-TrFE) and tested under the same tensile strain showed a lower response. In this configuration, a 40% ($\Delta C/C$) response was recorded in comparison to the 170% change in I_D with the OFET configuration. In addition, some of the important limitations of the ultrathin film-based flexible OFET device sensing behavior were effectively improved by adding special transducing features without compromising the sensing performance and device simplicity.

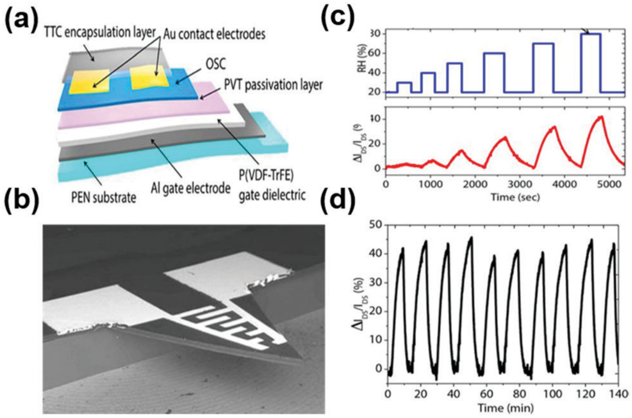

Fig. 22 (a) Schematic representation and (b) SEM image of an OFET-integrated MEMS sensor device; (c) (above) relative humidity introduced and (below) corresponding current response of the device; (d) repeatable behavior of the device in an 80% RH environment (reprinted with permission from Thuau *et al.*,[174] copyright 2016, Nature).

2.2 Semiconducting materials for light sensing (phototransistors)

The preparation of flexible phototransistors for wearable electronics (*e.g.*, in healthcare and environment monitoring systems) requires the use of semiconducting materials that simultaneously show a degree of mechanical flexibility,[29] nontoxicity, and biodegradability.[175,176] Indigo and its brominated derivative (6,6′-dibromoindigo (6-BrIG)) can be considered classic examples of safe and nontoxic organic semiconducting materials.[175,177] Indigo and 6-BrIG were known to be the subjects of the world's oldest chemical industry, being manufactured from natural sources and valued as much as gold.[178–180] Among these, 6-BrIG is of particular interest since it demonstrates the optoelectronic properties desired for the successful functionality of a phototransistor.[175,181–183] 6-BrIG exhibits strong inter- and intramolecular hydrogen bonding between its carbonyl and amine groups, which decreases the π–π stacking distances and induces planarity, both of which are favorable for effective charge transport. Air-stable electron transport is promoted by its low-lying LUMO level (3.7 eV), whereas the ambipolar charge injection is enabled by the small bandgap (1.8 eV). The addition of a broad absorption band (350–700 nm) of 6-BrIG implies facile electronic excitation upon exposure to visible light. Hence, 6-BrIG can be considered an attractive candidate to be used as a photoactive material. For instance, Kim *et al.* have recently reported on the fabrication and characterization of 6-BrIG-based ambipolar OPTs, having *n*-channel photoresponsivity and external quantum efficiency of 10.3 A W^{-1} and 2437%, respectively, and p-channel photoresponsivity and external quantum efficiency of 0.0554 A W^{-1} and 13.1%, respectively.[183]

In the OSC family, π-conjugated polymers show improved solution-processability, and better compatibility with flexible substrates. Furthermore, from a molecular viewpoint, polymers exhibit broader optical absorption, and much larger conjugation lengths which renders them more valuable for optoelectronic devices,[44] compared to small molecules.[184,185] For application

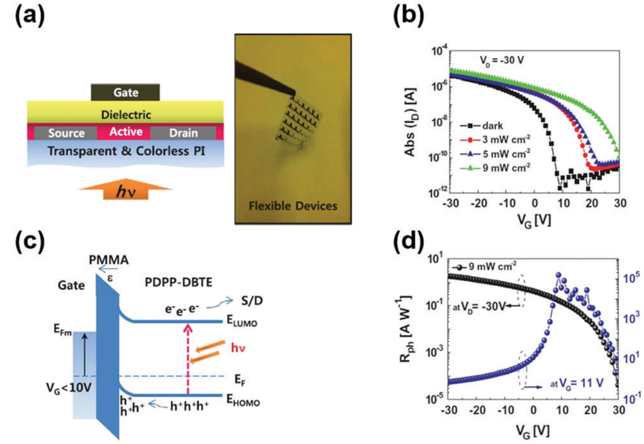

Fig. 23 (a) Schematic illustration of PDPP-DBTE-based OPTs and photograph of devices fabricated on flexible substrates; (b) $I_D \times V_{GS}$ characteristics in the dark and under illumination at various light intensities; (c) energy band diagram of PDPP-DBTE-based OPTs under illumination conditions with a negative V_{GS}; and (d) photoresponsivity and sensitivity as a function of V_{GS} (reprinted with permission from Kim *et al.*,[187] copyright 2014, Elsevier).

in OPTs, polymers are essentially required to demonstrate wide absorption and high μ_{FET}, such that the process of effective light absorption, exciton dissociation and charge transport is facilitated.[44,186] Kim *et al.* used the photoactive polymer, poly[2,5-bis(2-octyldodecyl)pyrrolo[3,4-*c*]pyrrole-1,4(2*H*,5*H*)-dione-(*E*)-1,2-di(2,20-bithiophen-5-yl)ethene] (PDPP-DBTE), to fabricate OPTs in a TGBC architecture with PMMA as the gate dielectric (Fig. 23a).[187] Under illumination intensities of 3, 5, 9 and 15 mW cm^{-2}, the OPTs showed a substantial increase in I_D and shift of V_T to positive values (Fig. 23b). In principle, following the photogeneration of charge carriers in the PDPP-DBTE layer, holes flow to the drain electrode whereas electrons mostly accumulate under the source electrode (Fig. 23c). The latter phenomenon can cause lowering of the hole injection barrier, leading to a positive shift in V_T. Overall, owing to the favorable optical properties of PDPP-DBTE, the OPTs developed by Kim *et al.* showed promising results with a photo-to-dark current ratio exceeding 5 orders. In addition, the devices showed an on-state photoresponsivity of $\sim$2.5 A W^{-1}, and off-state photosensitivity of $\sim 1.54 \times 10^5$ (Fig. 23d).

Pentacene is a desirable choice as far as wearable electronic applications are concerned since it is nontoxic, biocompatible, biodegradable, and mechanically flexible.[188,189] Thin films of this small molecule formed *via* evaporation consist of a highly ordered molecular structure in a "herringbone" arrangement.[190,191] The solid-state structure is dominated by strong intermolecular interactions, which promotes a high degree of crystallinity and efficient charge transport properties.[192] Pentacene is typically known to yield μ_{FET} values of $\sim$1 cm^2 V^{-1} s^{-1} in OFETs,[120,193] while the devices in which single crystals of pentacene are utilized are reported to show a μ_{FET} of $\sim$60 cm^2 V^{-1} s^{-1}.[194] In the case of phototransistor applications, pentacene is widely utilized in the research industry because of its small bandgap (2 eV) and relatively broad absorption band (300–600 nm). In SiO_2/pentacene-type devices, Debucquoy *et al.* have attributed the phototransistor effect to the trapping of photogenerated electrons by OH groups at the I/S interface.[195] Moreover, in a recent work, Park *et al.* have combined the nontoxic OSC (pentacene) with the biodegradable and flexible substrate (cellulose nanofibrillated fiber) to prepare high-performance phototransistors.[196] The devices withstood over 2000 bending cycles, and the use of environmentally friendly materials resulted in exceptional biodegradability characteristics, as confirmed by the fungal biodegradation test. Similarly, it was reported that the use of highly transparent nonmetallic electrodes (molybdenum trioxide-buffered indium zinc oxide) lead to phototransistor transmittance over 70%. This study not only further asserts the potential of pentacene-based phototransistors in wearable electronics but also highlights the advantage of combining biodegradable substrates for the realization of eco-friendly disposable systems.

Recent studies have highlighted DA copolymers as promising materials for OPT applications because of their low bandgap, which facilitates the harvesting of incident photons for effective charge carrier generation.[197–200] Wang *et al.* used a PBTIDBIBDF copolymer, blended with poly(1,4-butylene adipate) (PBA), to fabricate low-voltage and flexible OPTs (Fig. 24a).[201] The devices showed *P* and *R* values of 5.7×10^4 and 180 mA W^{-1}, respectively, while an increase in the illumination intensity was observed to induce a higher I_D and larger V_T shifts (Fig. 24b). Furthermore, the devices showed fairly stable photocurrent behavior under various on/off illumination cycles. The efficient photoresponse of these OPTs was attributed to the utilization of the PBTIDBIBDF copolymer as the photoactive layer, which exhibits highly ordered molecular packing, assisting in the effective transport of separated charge carriers under illumination. Similarly, the

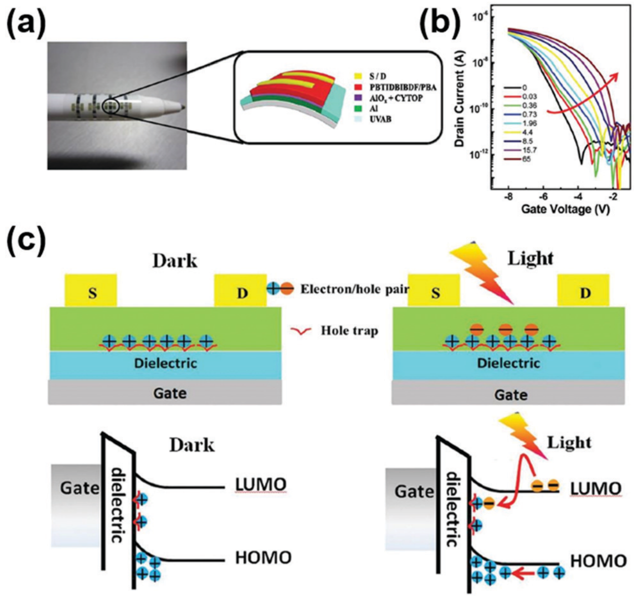

Fig. 24 (a) Flexible PBTIDBIBDF-based OPTs fabricated in the BGTC architecture; (b) $I_D \times V_{GS}$ characteristics of OPTs under various illumination intensities (V_{DS} = −5 V); and (c) schematic illustration of the OPTs and energy band diagrams elucidating the photoresponse behavior (reprinted with permission from Wang *et al.*,[201] copyright 2019, Wiley-VCH).

polar groups in the PBA molecules induced the charge trapping effects at the I/S interface, which improved the photosensitivity by causing significant shifts in V_T (Fig. 24b). The photoresponse behavior of PBTIDBIBDF-based OPTs can be further understood by the energy band diagram in Fig. 24c. The application of V_{GS} results in the accumulation of holes (that form positive donor areas) at the I/S interface. When the device is illuminated, free electrons and holes are generated in the PBTIDBIBDF layer, and the recombination of electrons and holes causes a positive shift in V_T. The increase in illumination intensities causes an increase in the recombination ratio, thereby resulting in a larger V_T shift. This also reveals that the PBTIDBIBDF-based OPTs operated in the photovoltaic mode.

2.3 Semiconducting materials for pH sensing

A pH sensor plays an important role in maintaining quality control in laboratory experimentation within a wide range of scientific areas, including bioelectronics,[202–204] agriculture,[205] oil,[206] water quality,[207] and drug delivery industries.[208] Although researchers around the world have been developing state-of-the-art pH sensors, there is still difficulty in making them cheap and easy to use. A good example is the paper-based colorimetric sensor, which is both low in cost and easy to make and use.[209] However, some cases require more stable devices where the temperature exceeds the room ambience. In this context, OFET has proved to be a promising candidate since it can be operated at low voltages and provides enhanced sensitivities in various sensing conditions.[210–212] It is important to note that bottom-gate OFET geometries are commonly preferred to avoid any kind of damage induced by the gate dielectric on the surface of the OSC.[133,213] One of the important drawbacks in this architecture, however, is the direct contact of the organic materials with the ambient conditions. To overcome these issues, Diallo *et al.* reported on a top-gated OFET-based ion-sensitive pH sensor prepared on Kapton flexible substrates using pentacene as the OSC.[214] This sensor consists of chemically inert parylene as the gate dielectric material, deposited on the surface of a pentacene active layer. The schematic representation of the as-fabricated device is shown in Fig. 25a.

In the initial stage of investigation, an increase in I_D was observed when the pH level was increased from 4 to 10 (Fig. 25b). In addition, the reported device showed good response and recovery behaviors (Fig. 25c), attributed to the use of the parylene dielectric and due to the slow annealing process of SiN:H.[214] Although the devices demonstrated good sensitivity to a wide pH range, the successful device operation relied on the use of a reference electrode (Ag/AgCl in Fig. 25a), which can be considered a barrier for integrating such devices in wearable and disposable applications. To overcome this issue, unique counter-electrodeless or freestanding ion-sensitive FET (ISFET) architecture was proposed by Caboni *et al.*[215] The proposed architecture consisted of two independent devices: a capacitor (Fig. 26a) and a pentacene-based OFET (Fig. 26b).

In this intricate device architecture, the capacitor and OFET devices are connected by the floating gate. The device mechanism is dominated by the electric field applied at the control gate and common source terminals, respectively. The electric field applied at the control gate terminal influences the biasing condition of the adjacent OFET *via* the floating gate terminal. The device operation mechanism takes the effect of pH sensing, which manifests itself by a change in I_D of the OFET device. One of the most crucial parts of this device is the effective functionalization of the floating gate surface with thio-aminic groups, which helps in determining the pH of the solution. When the test solution is exposed to the modified floating gate, a desired protonation and deprotonation cycle takes place based on the pH of the solution. Such chemical cycles change the charge density of either holes or electrons in the floating gate terminal. This, in turn, modifies the charge carrier concentration in the semiconducting channel of the adjacent OFET device. This process can be well understood with the help of the pH-sensing mechanism shown in Fig. 26b. The results obtained by Cobini *et al.* while using the ISFET sensor architecture are shown in Fig. 26c and d. The device showed good sensitivity behavior between pH levels 3 and 5, which is evident by the significant variation of both I_D and V_T of the OFET.

Although the authors successfully demonstrated a highly sensitive and reproducible pH-sensing device,[215] the high operating voltage makes it inappropriate for wearable device applications. This issue has been recently addressed by Li *et al.*, who developed a low-voltage, highly sensitive, and flexible pH sensor platform using the ISFET architecture.[216] Different from the architecture proposed by Caboni *et al.*,[215] the device architecture of Li *et al.* consisted of three key components: the OFET device, the working electrode, and the reference electrode.[216]

The OFET devices were fabricated on a PEN substrate. Firstly, the bottom gate and top source/drain contacts were

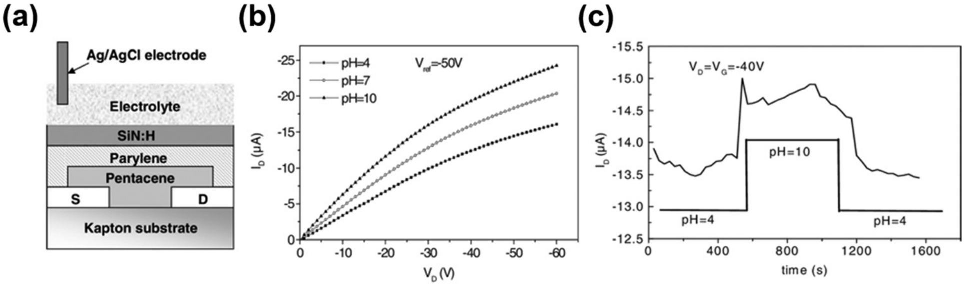

Fig. 25 (a) Schematic representation of flexible OFET device, (b) output characteristics and (c) transient response of device toward pH = 4, 7, and 10 (reprinted with permission from Diallo *et al.*,[214] copyright 2008, American Institute of Physics).

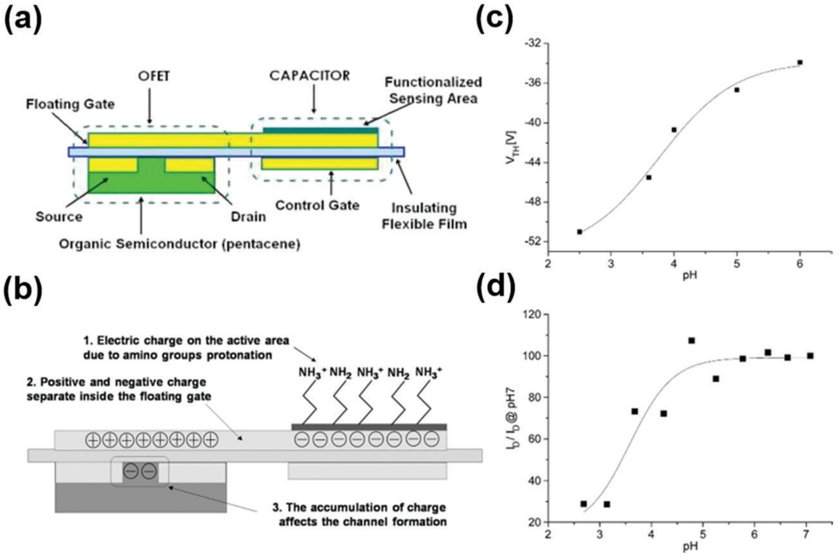

Fig. 26 (a) Schematic representation and (b) pH-sensing mechanism of a flexible OFET device; (c) threshold voltage behavior and (d) sensitivity of the device toward different pH conditions (reprinted with permission from Caboni *et al.*,[215] copyright 2009, IEEE).

formed by inkjet printing of silver ink. Subsequently, both the buffer layer and the gate insulator thin film were deposited by spin coating the PMMA solution on the gate, while the active channel was formed by drop casting the TIPS-pentacene:PS blend solution on top of the source/drain contacts. The as-fabricated OFET device was then separated from the original PEN substrate and transferred to a common PET substrate. Similarly, the other two important components of the sensing device, the reference electrode (Ag/AgCl/PVB) and the working electrode (ITO), were also formed on top of the PET substrate. Hence, all three major components of the device were integrated on a common PET platform, as shown in Fig. 27a.

As presented in Fig. 27b, the as-fabricated TIPS-pentacene:PS-based OFET device operated at low voltages and showed a promising I_{on}/I_{off} of around 10^5. Subsequently, the open-circuit potential difference was measured between the working and reference electrodes under different pH conditions. Notably, the pH was observed to maintain a linear relationship with respect to the measured voltage over a long period. To present a real-time model, a concrete relationship between the pH of the solution and the output current of the OFET device is required. To obtain this, an experiment was conducted in which the pH of the testing buffer solution was varied and the corresponding changes in I_D were observed (Fig. 27c). For fixed reference and

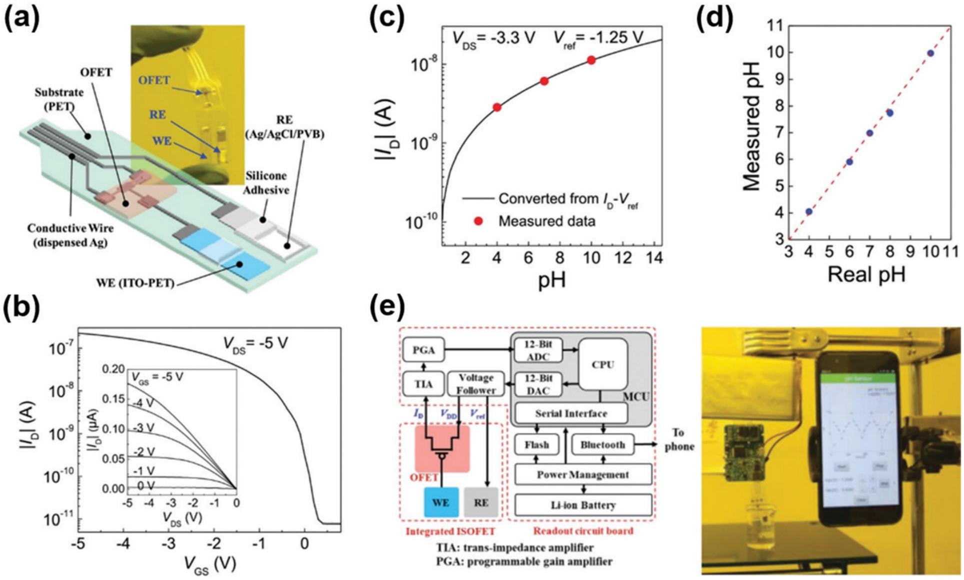

Fig. 27 (a) Schematic representation and (b) transfer with (inset) output behavior of an ion-sensitivity OFET (IOSFET) device; (c) relation between measured drain current and pH condition; (d) comparing the measured and standard pH values; (e) pH value reading circuit and real-time pH measuring set up using an as-fabricated flexible IOSFET device (reprinted with permission from Li *et al.*,[216] copyright 2018, IEEE).

drain voltages, I_D was observed to change nonlinearly for pH ranging from 2 to 14. In addition, the measured data also satisfied the theoretical values (Fig. 27d). Based on the obtained results, the electrical data readout circuits were developed and interfaced with the as-fabricated ISFET, as shown in Fig. 27e. In conclusion, Li *et al.* successfully demonstrated the pH-sensing behavior and, at the same time, wireless transmission of data to a mobile phone to visually observe the change in pH values of a given solution with respect to time (Fig. 27e). Hence, the reported device shows great potential to satisfy the requirements for future IoT-based smart-sensing applications.

2.4 Semiconducting materials for early disease diagnosis

Disease diagnosis is another important sector that constantly requires innovation and huge production capability.[217–221] As most of the diagnostic elements are not reusable and require regular replacement, it is favorable to adopt disposable elements with low cost.[222–224] Reactive oxygen species (ROS) are important signaling agents for diagnosing diseases at an early stage in human beings.[225–227] During a disease period, some of the cells' metabolic activities and their associated functions tend to generate biomolecules such as superoxides, which come under the class of ROS.[227] Jeong *et al.* have proposed a novel combination of rutin, a type of polyphenol, and conjugated polymer for the detection of superoxides secreted by the mouse macrophages.[228] The proposed sensing device, with the BGBC configuration, was fabricated by initially patterning the flexible PET substrate with ITO, which acted as the bottom-gate electrode (Fig. 28a). Subsequently, the spin-coating method was employed for depositing the gate dielectric (PMMA) on the surface of the as-prepared flexible substrate on top of which the source and drain electrodes were lithographically patterned. The active sensing layer (rutin-P3HT hybrid) was spin coated on the surface of the source/drain electrodes. In the first stage of investigation, after careful optimization, the proposed device showed good transistor performance when the rutin content was around 10 wt% in the host polymer material. However, the threshold voltage of the p-type rutin-modified device exhibited more positive voltage along with an increase in off current. Here, this problem may be mitigated by exploring more on the interface engineering with solvents other than toluene. As it is not an orthogonal solvent, it could have generated traps at the P3HT and PMMA, leading to increased roughness at the I/S interface regions.

The superoxide-sensing studies of the proposed OFET device were performed at 0.5 mM O_2^- molecules in the buffer solution. In this case, the OFET responded with a time lag of $\sim$50 s. As a result, irrespective of the increase in applied gate and drain voltages, an increase in relative drain current sensitivity with respect to time was observed. To find the LOD of the proposed device for the target superoxide, two methods were employed: the perfusion method and drop test. In the former, under constant gate and drain voltages of -0.5 V each, the concentration of the O_2^- superoxide molecules was tuned from 0 to 3 mM. As shown in Fig. 28b, the proposed device was observed to sense as low as 0.001 mM O_2^- concentration. Here, hydroxyl groups in rutin molecules interact with superoxide species in aqueous solutions and form H_2O_2 and oxygen anions. Thus, the positive charge gets doped in P3HT with these oxygen anions, increasing the response current. Unlike the perfusion technique, the drop test method played a vital role in observing the sensitivity of the proposed OFET sensing device down to an nM

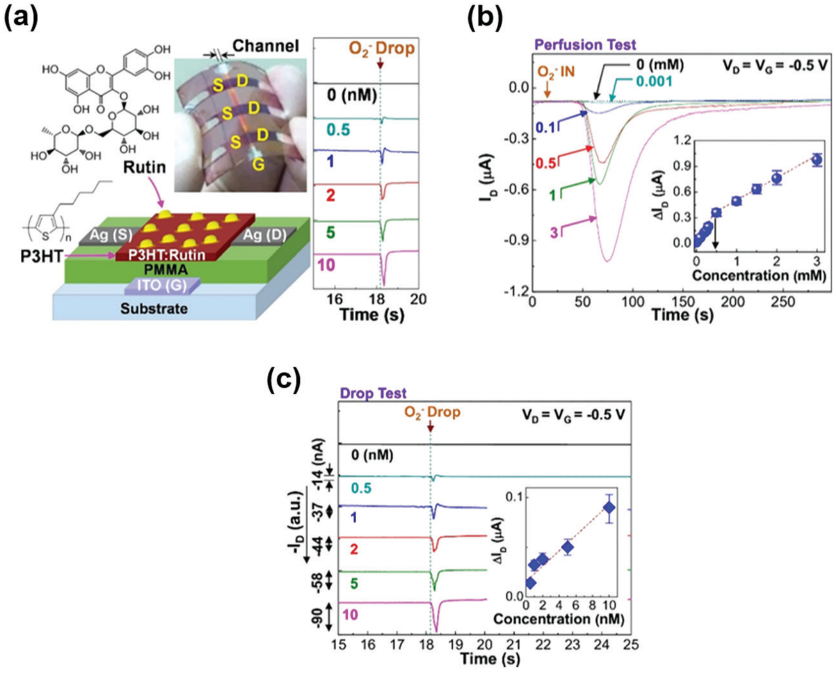

Fig. 28 (a) Schematic illustration of a P3HT:rutin-based flexible OFET device, (b) perfusion, and (c) drop test of the OFET device toward different lactate concentrations (reprinted with permission from Jeong *et al.*,[228] copyright 2018, Elsevier B.V.).

O_2^- concentration range. In this case, the device under testing showed ultrahigh sensitivity by successfully detecting 500 pM O_2^- ions concentration, which implies a difference of four orders of magnitude compared to the perfusion method, which can be seen in Fig. 28c. This can be explained as a result of the availability of abundant binding sites for the interaction to take place. In the former case, the presence of inlet and outlet in the flow cell could have led to less interaction time, thereby leading to a minimal LOD. However, in the case of the drop test, the entire solution is concentrated around the device with improved interaction time. As a result, the available O_2^- gets enough time to interact with target analytes since no flushing is involved.

In addition to sensing studies, based on the requirements of real-time applications, the authors also conducted operational stability and device reusability tests. Interestingly, the reported device successfully responded to various superoxide concentrations, ranging from 0.1 mM to 3 mM, repeated ten times. Moreover, by using a PBS buffer solution, the as-fabricated sensor exhibited satisfactory superoxide response after 15 days of cold storage. In summary, the study by Jeong *et al.* reported a sensor that is mechanically flexible and highly sensitive, showing stable and reliable detection of superoxide molecules from living organisms.[228]

2.5 Semiconducting materials for drug abuse detection

In the modern era, drug-based tablets are commonly prescribed medications for various diseases. Among many, amphetamine-type stimulants (ATS) are one of the most popularly prescribed drugs for treating health problems such as asthma, diabetes, and so forth.[229–232] However, this easy access to such strong prescribed medications can very easily lead to drug abuse and addiction. According to the WHO, in recent years, young people from different parts of the world have been reported to illegally consume ATS drugs for boosting their physical and mental activities.[233] At present, the widely used systems for detecting ATS analytes are based on chromatography,[234] spectroscopy,[235] and molecularly imprinted polymers.[236,237] However, these systems are bulky and costly, which obviously stands as a barrier for large-scale usage. A viable solution was recently proposed by Jang *et al.*, who reported on a low-cost, highly sensitive, and wearable OFET-based ATS sensing system.[238] The BGTC DDFTTF-based OFETs were fabricated on Si/SiO_2 substrates (Fig. 29a), and the receptor–analyte interaction strategy was used for selectively sensing ATS biomolecules from various aqueous solutions. Hence, the cucurbit[7]uril (CB[7])-based derivatives were spin coated on the surface of the OSC. Based on the results from NMR and XRD analysis, the CB[7] receptor molecules tend to show weak van der Waals force of interaction with the target ATS biomolecules. Here, the authors used CB[7] derivatives since they are soluble only in water, whereas the OSC (DDFTTF) is immune to water. Thus, they adopted an orthogonal solvent technique to deposit a bilayer stack of both channel layer and receptor layer. This approach apparently improved the easy thin-film formation of CB[7] on top of DDFTTF without degrading the channel characteristics. The electrical characteristics of the OFET device with and without CB[7] were initially measured. As shown in Fig. 29b, the former device architecture exhibited the transfer characteristics with high hysteresis when compared to their non-CB[7] counterpart. However, both the device architectures notably presented a I_{on}/I_{off} ratio of around 10^5. Subsequently, the ATS-sensing properties of the CB[7]-modified DDFTTF-based OFET device

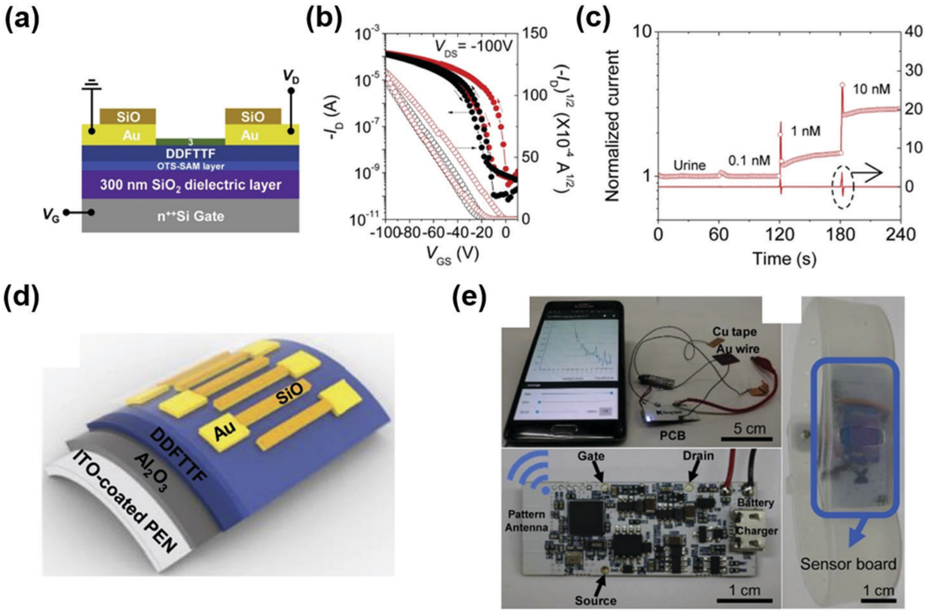

Fig. 29 (a) Schematic illustration and (b) transfer characteristics of a DDFTTF OFET on a silicon substrate, (c) OFET device response toward different concentrations of ATS analytes in urine samples, (d) schematic representation of the DDFTTF-based flexible OFET device, (e) photograph demonstrating the integration of the flexible OFET device on the wristband for real-time monitoring application (reprinted with permission from Jang *et al.*,[238] copyright 2017, Elsevier Inc.).

were investigated. The as-fabricated device was primarily exposed to different concentrations of ATS with distilled water as a base reference solution. As a result, in the case of one of the CB[7] derivatives, allyloxyCB[7], the modified OFET device showed good sensitivity for ATS concentration as low as 1 pM. Unlike an allyloxyC[7] derivative, its phenylbutoxyCB[7] counterpart exhibited good sensitivity toward a wide range of ATS concentrations from 1 pM to 1 μM, having standard PBS as the base solution. Furthermore, to mimic real-time testing conditions, the phenylbutoxyCB[7] functionalized OFET device was used for sensing ATS molecules in biological urine samples. Interestingly, the device under testing presented excellent sensitivity toward a narrow range of ATS concentrations from 0.1 nM to 10 nM, as shown in Fig. 29c.

In the next stage of investigation, for achieving low-voltage operation conditions, the reported sensors were fabricated on ITO/PEN flexible substrates, having Al_2O_3 as the gate dielectric and CB[7]-functionalized DDFTTF as the active channel material (Fig. 29d). When the as-fabricated flexible device was exposed to 1 pM ATS molecules with distilled water as the base solution, a good sensing response was observed at operating voltages of -1.5 V (V_{DS}) and -10 V (V_{GS}), which is much lower than those of the Si/SiO_2 devices. As shown in Fig. 29e, Jang *et al.* successfully demonstrated the real-time usage of the proposed ATS sensor. In essence, a low-power, cost-effective, and portable ATS sensor for biomedical applications was developed that shows high sensitivity and selectivity toward target analytes.

2.6 Semiconducting materials for other sensing target applications

2.6.1 Strain sensor. Strain sensors can be considered one of the integral parts of flexible and stretchable sensing systems. To achieve good sensitivity and robustness, silicon-based strain sensors are widely used.[242–244] However, the currently available rigid silicon-based strain sensors are not compatible with target flexible and wearable electronics.[245] In this context, one of the growing alternatives is the utilization of OFET devices for sensing application.[246] Researchers have adopted the OFET-based strain sensors for two main reasons: high sensitivity of structural and charge transport properties to mechanical changes and possibility of large-scale fabrication on flexible substrates.[247] Considering these unique features, Loi *et al.* compared the strain-sensing properties of pentacene and P3HT-based OFET devices.[246]

As seen in Fig. 30a, the OFET devices were fabricated on flexible PET substrates, having parylene-C as the gate dielectric material. Two OSCs (pentacene and P3HT) were employed, and their strain-sensing properties were tested. The pentacene-based strain sensor displayed good sensitivity and a linear response over a short range of strain when compared to the P3HT device (Fig. 30b). This behavior was attributed to the large grain sizes, and uniform thin film formation was confirmed with the help of AFM images. Based on these results, the as-fabricated sensor was tested under real-time conditions. In the beginning, the sensor was subjected to intensive bending conditions for different angles ranging between 90° and 180°. Interestingly, the as-fabricated strain-sensing system differentiated each bending angle with the equivalent drain current (Fig. 30c), and the reported device remained both mechanically and electrically stable even after 100 bending cycles (Fig. 30d). These outcomes clearly highlight the robustness and reliability of employing these devices in flexible strain-sensing applications.

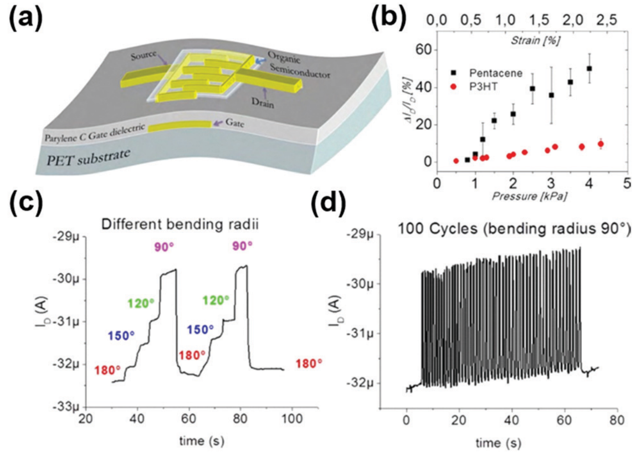

Fig. 30 (a) Schematic representation of a P3HT based OFET flexible device. (b) Comparison of P3HT and pentacene device current response for different pressure and strain conditions applied. (c) Distinct current response for a wide range of device bending conditions from 180 to 90 degree. (d) Repeatable (100 times) current response of the device under 90 degree bending radius strain condition (reprinted with permission from Loi *et al.*,[246] copyright 2013, IEEE).

Along with this report, many research groups have strongly suggested that under applied strain, the change in electrical behavior is mainly due to the structural deformation of the active OSC material.[248–250] However, Scenev *et al.* have detected that a detailed study regarding the relationship between applied strains and their relative changes on the structural properties of OSC was lacking.[239] Thus, to understand this relationship, Scenev *et al.* investigated the electromechanical properties of pentacene-based flexible OFET devices for strain-sensing-based applications. The OFET devices were fabricated on flexible PET substrates and utilized PVA as the gate dielectric (Fig. 31a). In this case, a special bending apparatus was employed to produce uniform strain conditions over the whole device area. The transfer characteristics of the as-fabricated flexible device were measured under two different conditions. Primary test results show that the device displayed hysteresis-free electrical characteristics for an applied strain of less than 2%. From the latter test, the hysteresis drastically increased with the strain applied from 0 to 3.3%, as shown in Fig. 31b. To understand this behavior, both scanning force microscopy (SFM) and XRD characterization on a PEN-modified PVA dielectric was performed. When the PEN layer was deformed from 0 to 1.3%, the SFM results confirmed that there is no significant shift in the inter-grain boundary distance (Fig. 31c). In contrast, the inter-grain boundary distance gradually increased when the applied strain reached 10% (Fig. 31d). Moreover, the XRD results confirmed that there is no deformation in the PEN crystal structure for the applied strain of about 10%. Hence, with the help of these results, Scenev *et al.* have suggested that

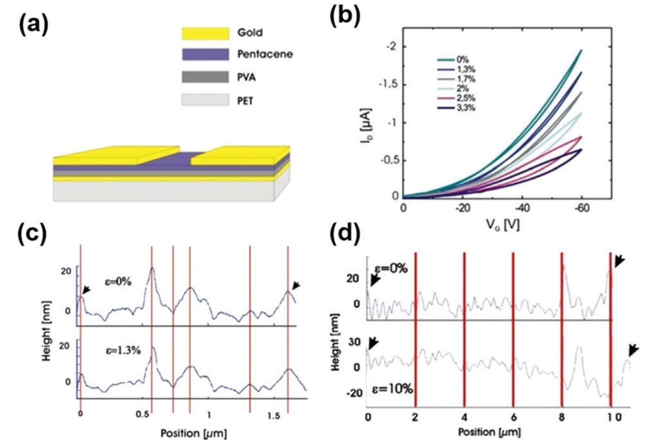

Fig. 31 (a) The fabricated pentacene OFET device stack. (b) Transfer characteristics of device for different strain conditions from 0 to 3.3%. AFM height images recorded after applying (c) 1.3% and (d) 10% strain on pentacene film (reprinted with permission from Scenev *et al.*,[239] copyright 2013, Elsevier B.V.).

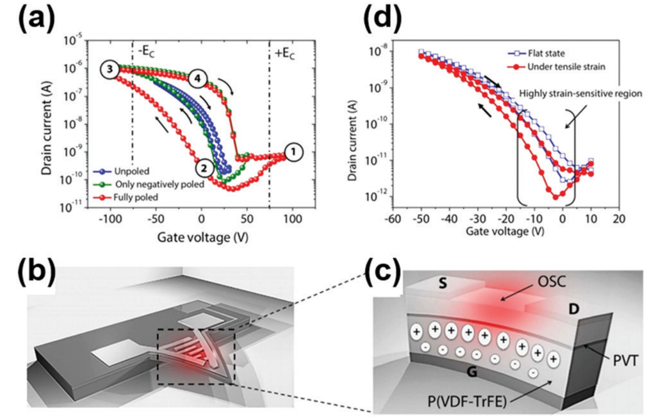

Fig. 32 (a) Comparison of transfer characteristics and associated hysteresis behavior for different poling conditions. (b) Effect of strain and (c) corresponding impact on the dipole properties of the P(VDF-TrFE) layer. (d) Change in device transfer characteristics under applied tensile strain conditions (reprinted with permission from Thuau *et al.*,[174] copyright 2016, Nature).

upon the application of strain, the potential barrier for the electron flow between the grain boundaries tends to increase. This, in turn, decreased the μ_{FET} and I_{D} along the channel at the I/S interface region, which satisfied the results observed in Fig. 31b. Notably, the gold electrodes, on top of the OSC, lost their mechanical stability for the strain $<2\%$. This stands as a barrier for using the proposed device as a reliable strain sensor. To overcome this problem, Scenev *et al.* suggested the use of soft yet highly conductive electrodes for improving the sensitivity and lifetime of the proposed flexible OFET-based strain sensor.

Another approach for improving the sensitivity toward applied strain is the integration of micro-electromechanical systems (MEMS) technology in the OFET device architecture. It is important to note that the growth of inorganic MEMS-based sensors has drastically declined in the past decade due to their poor compatibility in flexible and wearable applications.[251] Alternatively, the organic MEMS device concept is growing rapidly because of the intrinsic high sensitivity to mechanical deformations.[174] For developing sensitive strain sensors, the mechanism that bridges the gap between MEMS and OFET is the mechanical-to-electrical conversion technique.[172] In this context, Damien *et al.* combined the versatile properties of a MEMS-based organic cantilever with OFET devices using a piezoelectric mechanism for strain-sensor application.[174] Owing to the air stability requirement, pentacene and DNTT organic small molecules were chosen for fabricating the OFET-embedded cantilever device architecture. Here, the piezoelectric P(VDF-TrFE)/PVT polymer was employed as the gate dielectric material. As shown in Fig. 32a, the electrical characteristics of the as-fabricated OFET device were studied with different poling conditions which is crucial for understanding their strain sensing capabilities.

It is clear from the figure that the hysteresis in the drain current response was enhanced with the level of sweeping voltage. This result is attributed to the influence of polarization parameters in the piezoelectric gate dielectric by the applied gate bias. The schematic representation of the strain-induced changes in the device are presented in Fig. 32b and c. When the cantilever tip is subjected to mechanical strain, shifts in both drain current and threshold voltage are witnessed (Fig. 32d). This is due to a positive polarization effect induced in the gate dielectric material. This, in turn, influenced the charge density in the channel region of the OFET device. As a result, the sensitivity of the pentacene-based OFET-cantilever hybrid device was measured to be around 600, which is around five times greater than the DNTT-based strain sensor. This report also highlighted the importance of the polarization effect in the piezoelectric gate dielectric material for augmenting the sensitivity toward the change in strain levels. The above discussed literature reports have critically failed to project the real time capability of the sensor. Demonstrating the real time potential of the home-made sensor is crucial to bridge the gap between the laboratory inventions and the practical devices. In light of this requirement, Lai *et al.*[252] have not only fabricated a novel and low power flexible strain sensor but also successfully integrated it into commercially available gloves to monitor hand movement. This embedded sensor was connected to the custom-designed readout circuits to convert the current into useful voltage levels which can then be processed for conveying required information to the people. Even-though the authors have demonstrated the effective use of strain sensors in transducing the hand movement, they ended up with a bulky system. Hence, still there is a need to develop a smart, compact, flexible, low power and high performance flexible strain OFET sensor system to satisfy the demand of wearable electronics.

2.6.2 Multifunctional sensing capabilities. For the past two decades, many researchers have proposed numerous sensing solutions for various applications.[253,254] However, most of the solutions are based on the use of a single sensing system. Moreover, these proposed systems are generally prepared with inorganic materials for attaining good performance and robustness,[255–257]

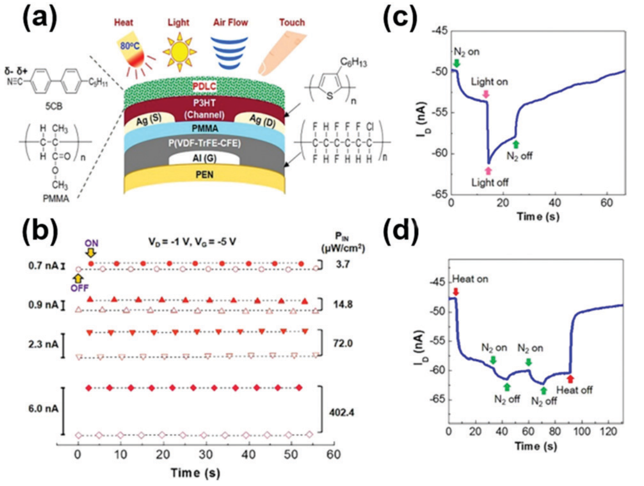

Fig. 33 (a) Schematic representation and (b) photo-response of the bottom contact OFET device with a dual polymer gate dielectric. Multi-sensing device response toward (c) N_2 and light, (d) heat and N_2 stimulants (reprinted with permission from Song *et al.*,[240] copyright 2017, Nature).

which makes them unsuitable for next-generation flexible and wearable sensing platforms. One of the reliable alternatives in the current research trend is the use of an OFET device approach.[240] The main objective of this approach is to achieve good sensitivity and robustness, appreciable mechanical flexibility, and large-scale production on flexible platforms through cost-effective industrial processing techniques. Therefore, a combination of multi-functional sensing strategy with OFETs is needed to satisfy the requirements of future applications such as artificial skin, complex sensing systems in unmanned aerial vehicles, and so forth.[258–260]

Song *et al.* have recently proposed a novel combination of polymer-dispersed liquid crystal (PDLC) and an OFET device for realizing a multi-sensing platform.[240] The BGBC P3HT-based OFET devices were fabricated on PEN flexible substrates with PMMA/P(VDF-TrFE-CFE) as the bilayer gate dielectric (Fig. 33a). This device was then considered for testing its sensing capability toward different external stimulants such as heat, light, airflow, and physical touch. When the device was subjected to N_2 gas flow, I_D increased linearly with the gas flow ranging between 0.1 and 10 sccm. With an increase in gas flow, a small amount of pressure was experienced by the surface of the PDLC layer, which resulted in drifting the negative dipoles of the 4,4′-pentyl-cyanobiphenyl (5CB) microdots downward. This increased the hole-charge carrier density and, thus, the drain current in the OFET channel region.

A similar sensing mechanism was proposed when the as-fabricated device was subjected to the applied load. As a result, when compared to the N_2 flow response, the change in drain current steeply increased with the load applied between 0.1 and 10 g. It is worth noting that in both N_2 flow and load-sensing cases, the electrical dipole moment of the PDLC layer influences the charge-carrier transport behavior in the P3HT layer. Interestingly, as shown in Fig. 33b, when the incident light (550 nm) power increased from 3.7 to 400 μW cm^{-2}, the drain current increased from 0.7 to 6.0 nA. This behavior was observed because when light is absorbed by the P3HT layer, exciton pairs are generated, which increases the dominant charge-carrier concentration along the channel. Subsequently, the temperature-sensing capability of the proposed PDLC-based OFET device was observed. At drain and gate voltages of −1 V and −5 V, respectively, the relative current sensitivity gradually increased with temperatures from 40 to 70 °C. This increased drain current is due to the effect of thermally induced hole-carrier mobility along the P3HT/PDLC interface.

Recently, our group[261] has successfully developed a fully flexible, biocompatible, and wearable device with good stretchable nature. This homemade skin platform was successfully integrated with a biocompatible sensor. The combination of the proposed magnetic skin and the associated sensor was demonstrated by installing them in the vicinity of the eye to monitor the movement of eyelids. As a next step to this research work, we can integrate the developed system with the circuit system (comprising an amplification block and Analog to Digital circuit (ADC)) that can be completely realized using organic transistors.[261]

In the next step of investigation, the multi-sensing capability of the proposed device was reported. Primarily, the device was simultaneously exposed to N_2 flow and light. As seen in Fig. 33c, the drain current increased gradually and then sharply decreased when exposed to N_2 flow and light exposure, respectively. After turning off the light and gas flow, the device retreated back to the base current. Similar experiments were conducted to test the as-fabricated device with the combination of heat and nitrogen gas. From Fig. 33d, it is clear that the current change with respect to the applied heat is more significant than the effect of nitrogen gas. In conclusion, low-cost, flexible, and compact PDLC-based P3HT OFET devices exhibited excellent multi-sensing capability toward various external stimulant conditions.

An optically transparent and mechanically flexible sensor with multi-sensing capability is in high demand for satisfying the requirements of robotic applications.[241] However, some of the bottlenecks in realizing such a sensor include the choice of materials and employing low-temperature processing techniques, which can assist in fabricating simple yet innovative devices on low thermally stable flexible substrates.[262–264] Trung *et al.* studied the mechanical and temperature-sensing capabilities of the pentacene-based OFET devices fabricated on flexible PES substrates (Fig. 34a).[241] Here, the multi-sensing capability of the proposed devices was mainly attributed to the crystalline nature, as well as pyroelectric and piezoelectric properties, of the gate dielectric P(VDF-TrFe). In addition to the dominant electric dipole properties of the gate dielectric, the properties of the OSC and the substrate may also influence the sensing response. To avoid these negative effects, an AC gate bias was applied to measure the dielectric potential or voltage (V_0). This measured voltage precisely changes with respect to the applied multiple stimulant conditions. To observe this effect, the as-fabricated device was primarily exposed to different physical stimulants, such as IR illumination, pressure, and strain excitation individually, and the corresponding changes in V_0 values were measured. With the

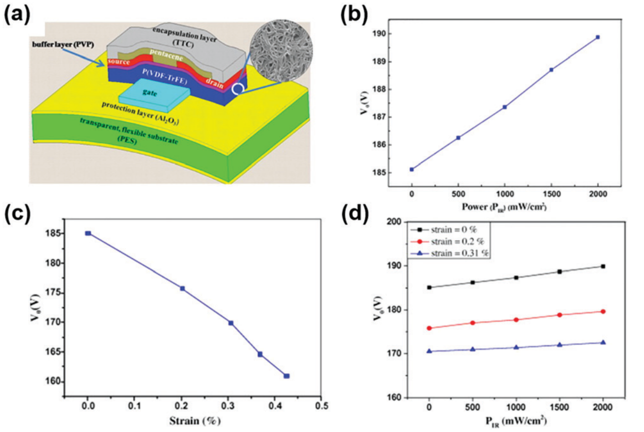

Fig. 34 (a) Illustration of materials used in bottom gate bottom contact pentacene OFET flexible device. Device voltage response toward (b) incident light, (c) applied strain and (d) combination of both light and strain (reprinted with permission from Trung *et al.*,[241] copyright 2012, Elsevier B.V.).

increase in incident IR power from 0 to 2000 mW cm^{-2}, the gate-dielectric crystal layer experienced thermal expansion due to a positive pyroelectric effect. This leads to the increase in electric dipole moment, which results in a linear increase of V_0, as seen in Fig. 34b.

In contrast, when the mechanical deformations such as pressure and strain were applied, due to a negative piezoelectric effect, V_0 showed a reduction (Fig. 34c). Subsequently, the multi-sensing capability was tested by simultaneously exposing the as-fabricated device to IR radiation and strain. Fig. 34d shows the plot of V_0 as a function of IR radiation power for different strain conditions. With the increase in IR radiation and strain, V_0 increases due to a positive pyroelectric effect, and the voltage level shifts down because of the piezoelectric mechanism. Furthermore, the authors also tested the effect of mechanical deformation on the sensing performance of the proposed device. Even after 10^4 bending cycles, irrespective of external stimulants, the degradation of the device's sensing capability tends to reduce with the increase in bending radius from 1 cm to 1.5 cm of the proposed flexible device. Such characteristics validate the development of a mechanically flexible, portable, cost-effective, and multifunctional OFET device. In summary, the sensing performances of the recently reported flexible OFET based strain and multimodal sensors are presented in Table 4.

3. Outlook and conclusion

Mechanical flexibility of electronic devices can be considered an important criterion due to the ever-growing need for making electronics conformable around objects, which will eventually lead to the development of wearable sensors and bendable electronics. In this paper, we have reviewed different types of flexible OFET devices that can be effectively utilized as transducers in next-generation sensing applications. There was also a thorough analysis of various OSCs reported in the literature that show compatibility with flexible OFET sensors and of the fabrication details that pertain to flexible sensor devices. On one hand, we stressed the dependence of sensitivity on the device geometry and the OSC material, while, on the other hand, we discussed the role of materials' characteristic features in deciding the selectivity of the sensor. Thus, it is proposed that the optimization of device structure can efficiently improve the sensitivity while retaining the selectivity of the corresponding analyte, which essentially renders a change in its LOD. Furthermore, the stability of an OFET is a material-specific issue and cannot be ruled out for both high and low shelf-life materials. It also depends on the medium on which the sensing is being carried out; for instance, OFETs will not have the same kind of response in air and aqueous media (in the presence of sweat). Similarly, other media like acidic and base will affect the surface of the device either by a reduction or oxidation process, essentially doping the bulk. Finally, key parameters like the response time and intensity are not static. They depend on the concentration of the analyte under test, intensity of pressure, intrinsic strain withstanding capability, amplitude of radiation, lifetime of the source, volume of the flow cell (container), and saturation levels of the receptor material. Thus, every individual application will have its own set of geometrical and fundamental physical property limitations apart from the externally influencing factors.

In addition, the essential cleaning techniques employed in the process of fabrication can greatly influence the properties of the deposited device layers. Unlike the Si and other inorganic substrates, acetone and high-frequency sonication cleansing

Table 4 Materials used for other sensing applications and their parameters in as-fabricated devices

Material	Sensor application	Sensitivity	Device	Limit of detection	Media	Flexibility limit
10	Strain sensor[239]	15%	BGBC OFET	0.01 N	Kapton	No information
8	Strain sensor[174]	600	Cantilever OFET	$<0.3\%$	PEN[a]	No information
10 + PDLC[a]	Multimodal sensor[240]	Gas flow: 2 nA sccm^{-1} Pressure: 1 nA g^{-1} Light: 0.2 nA (μW cm^{-2})$^{-1}$ Temperature: 0.06 nA °C^{-1}	BGBC OFET	0.2 sccm 0.8 g 3.7 μW cm^{-2} 40 °C	PEN[a]	No information
8	Multimodal sensor[241]	Light: 3 mV (mW cm^{-2})$^{-1}$ Pressure: 10 V MPa^{-1} Strain: 50 V per %	BGBC OFET	0.1 mW cm^{-2} 0.15 MPa 0.1%	PES[a]	Bending radius: 1.5 cm

[a] PEN = polyethylene naphthalene, PES: polyestersulfone, PDLC: polymer dispersed liquid-crystal.

cannot be used for organic polymer substrates. Such approaches do affect the plasticity of these substrates and may render unwanted surface effects. An approach with mild sonication in ethanol and isopropyl alcohol (IPA) would suffice for the later substrates. In the case of flexible glass and ultrathin Si substrates, which are flexible enough and brittle as compared to PET, PEN, and polyimide sheets, acetone can be used in the cleaning process since it does not damage the substrate. Furthermore, either plasma oxygen or UV light-assisted cleaning renders the surface more hydrophilic. This helps in the better adhesion of OSCs or any other SAMs on the surface used as per the requirement.

A strategic way to build any kind of sensor depends on the capabilities to engineer the deposited material. In some cases, material properties like spring constant play a crucial role in the bending radius of the sensor and can influence pressure-sensing characteristics. On the other hand, for gas, bio, and chemical sensing, it is the intrinsic conduction capability and the ability to tune the energy levels when encountered by an alien element that decide the efficiency. For applications like soil nutrient sensing or in solution detection, DDFTTF proves to be more efficient as it repels any H_2O content and remains pristine. Active binding sites in the composite format or dual layer (with receptors beneath the DDFTTF) can help in realizing specific sensors with humidity and moisture aversion capability.

The activation of the receptor surfaces (binding sites) is another important criterion for most of the sensors. This requires removal of the whole solvent from the system by means of annealing or by N_2 gas purge. Unless the activation of the compound is performed, the required sensitivity cannot be achieved. In addition, sometimes these solvent sites can also contribute to the early degradation of the material (*i.e.*, the shelf-life of the material lessens). An efficient technique like Brunauer–Emmett–Teller (BET) analysis can provide more information regarding the adsorption of gas on a solid surface and in pores of a system. The results of BET vary depending on the presence of solvent in the system. In addition, the use of thermogravimetric analysis (TGA) of the systems is to check the mass of the polymers with varying temperatures. This provides in-depth information on the polymers used in flexible devices and their effects due to the presence of an alien material. Thus, TGA assists in finding the suitable temperatures for polymers and simultaneously helps in identifying the foreign particles they can withstand without affecting the integrity. We believe that exploring the small molecule OSC, 2,2′,6,6′-tetraphenyl-dipyranylidene (DIPO-Ph4), for the analog circuit concomitantly with the sensors' geometry in wearable electronics will assist in overcoming the dichotomy between different OSCs.[265] We have also previously reported on transistor and memory performance of DIPO-Ph4 while achieving μ_{FET} of 2×10^{-2} cm^2 V^{-1} s^{-1} and $I_{\mathrm{on}}/I_{\mathrm{off}}$ of 10^4. The memory characteristics of the material in the lateral configuration were observed over the surface of the device with conductive atomic force microscopy (c-AFM) using voltage profiles of +4 V and −4 V. We recorded most accentuated hysteresis for a distance d = 5.5 μm, with a current ratio of ~7.5 nA at −2.5 V between both voltage sweeps.

When a process flow covers all the above criteria, one tends to think that the tradeoff has been achieved for successful implementation. However, in bigger flexible platforms, issues exist such as an increase in line resistance by orders of magnitude between sensor devices and between device-to-contact pads. Such conditions can be mitigated by adopting proper patterning techniques or by adapting materials that are highly sensitive to the changes induced due to line resistance issues. For example, a wearable sensor substrate for the trunk of a tree or the stem of a plant requires dimensions ranging from a few millimeters to hundreds of centimeters. Thus, for substrates that must be conformable, it is always essential to have uniformity in the thickness of materials, avoid substrate wrinkles, have more bendable radius, and have optimized interconnection widths.

Apart from the above issues related to substrates and platforms, material combinations need to be synergistic to attain multi-functional requirements. Innovative materials and reliable methods are essentially needed to make sure that the active channel layer and the receptor layers are indeed safe and can revive. Perhaps the most pressing need is for self-healable materials that can actually mimic traditional electronic materials and at the same time recuperate from any deformations. In some cases, even the existing inorganic electronic materials can be thinned down to the nanoscale, which essentially improves their flexibility. By means of elastomers, these materials can also be made stretchable as long as the Young's modulus for the wearable material is in the range of 1 kPa to 1 MPa. However, these materials are not suitable for applications in harsh environments, and thus there is a tremendous need for healable materials that can withstand such circumstances. Newly emerging composites may be considered a reasonable alternative in cases where the material is required to be both conductive and mechanically stable.[266,267] Similarly, the advantage will be multifold if thermoelectric materials (generators) themselves are used as substrates to provide the required power for devices to operate. This not only helps in energy scavenging from body heat or vibrations but also retains most of the initial power (scavenged) after multiple cuts and healing.

To conclude, the integration of electronics with a bendable and stretchable platform is the pathway to the future. Recently, we were successful in developing a wearable platform of a three electrode potentiostat system that can sense multiple analytes. Such a system includes both analog and digital front ends on a flexible PCB made with off the shelf components and consume more space. Thus readout circuit integration into the system itself with the same device technology is the need of the hour. Although significant progress has been made in OFETs in the past three decades, with a wide range of applications, there is a lack in their performance in terms of speed and stability. In addition, these devices must imbibe qualities such as multivariate sensing, which can be possible only when other transduction mechanisms can be supported in such systems. Such requirements vary from application to application, with multifunctional coatings doing more than just repelling water. In addition, adopting CMOS kind of technology with OFETs paves way to integrated circuit technology based completely on OSCs. This way one can realize a flexible electronics platform that integrates analog-to-digital converters (ADC) with the sensor devices and helps in not only realizing the 3D integration technology by means of stacking multiple materials but also avoids weak interfaces. Further, by adopting light emitting OFETs, this 3D integration can be made more viable and is the future path for multiple applications. Provided we address the above criteria, the doors will be open for OFETs in different wearable sensing platforms such as healthcare, plant science, and marine science, to name a few.

Conflicts of interest

There are no conflicts to declare.

Acknowledgements

Qian Liu is thankful to QUT for offering the QUTPRA scholarship to conduct his research. Prashant Sonar is thankful to QUT for the financial support from the Australian Research Council (ARC) for the Future Fellowship (FT130101337) and QUT core funding (QUT/322120-0301/07).

References

1 M. Billinghurst, *Computer*, 1999, **32**, 57–64.
2 T. L. Martin, in Proceedings – International Symposium on Wearable Computers, ISWC, IEEE Computer Society, 2002, vol. 2002, pp. 5–11.
3 J. R. Sempionatto, T. Nakagawa, A. Pavinatto, S. T. Mensah, S. Imani, P. Mercier and J. Wang, *Lab Chip*, 2017, **17**, 1834–1842.
4 E. Teller, J. M. Stivoric, C. D. Kasabach, C. D. Pacione, J. L. Moss, C. B. Liden and M. A. McCormack, *US Pat.*, 7689437B1, 2003.
5 J. Kim, A. S. Campbell, B. E.-F. de Ávila and J. Wang, *Nat. Biotechnol.*, 2019, **37**, 389–406.
6 S. Wang, J. Xu, W. Wang, G.-J. N. Wang, R. Rastak, F. Molina-Lopez, J. W. Chung, S. Niu, V. R. Feig, J. Lopez, T. Lei, S.-K. Kwon, Y. Kim, A. M. Foudeh, A. Ehrlich, A. Gasperini, Y. Yun, B. Murmann, J. B.-H. Tok and Z. Bao, *Nature*, 2018, **555**, 83–88.
7 A. Nawaz and I. A. Hümmelgen, *J. Mater. Sci.: Mater. Electron.*, 2019, **30**, 5299–5326.
8 X. Wang, L. Dong, H. Zhang, R. Yu, C. Pan and Z. L. Wang, *Adv. Sci.*, 2015, **2**, 1500169.
9 A. N. Sokolov, B. C. K. Tee, C. J. Bettinger, J. B. H. Tok and Z. Bao, *Acc. Chem. Res.*, 2012, **45**, 361–371.
10 S. C. B. Mannsfeld, B. C.-K. Tee, R. M. Stoltenberg, C. V. H.-H. Chen, S. Barman, B. V. O. Muir, A. N. Sokolov, C. Reese and Z. Bao, *Nat. Mater.*, 2010, **9**, 859–864.
11 S. Hannah, A. Davidson, I. Glesk, D. Uttamchandani, R. Dahiya and H. Gleskova, *Org. Electron.*, 2018, **56**, 170–177.
12 H. Matsui, Y. Takeda and S. Tokito, *Org. Electron.*, 2019, **75**, 105432.
13 Q. Huang and Y. Zhu, *Adv. Mater. Technol.*, 2019, **4**, 1800546.
14 R. Shiwaku, H. Matsui, K. Hayasaka, Y. Takeda, T. Fukuda, D. Kumaki and S. Tokito, *Adv. Electron. Mater.*, 2017, **3**, 1600557.
15 S. Chung, K. Cho and T. Lee, *Adv. Sci.*, 2019, **6**, 1801445.
16 S. Conti, S. Lai, P. Cosseddu and A. Bonfiglio, *Adv. Mater. Technol.*, 2017, **2**, 1600212.
17 C. Koutsiaki, T. Kaimakamis, A. Zachariadis, A. Papamichail, C. Kamaraki, S. Fachouri, C. Gravalidis, A. Laskarakis and S. Logothetidis, *Org. Electron.*, 2019, **73**, 231–239.
18 M. Hambsch, K. Reuter, M. Stanel, G. Schmidt, H. Kempa, U. Fügmann, U. Hahn and A. C. Hübler, *Mater. Sci. Eng., B*, 2010, **170**, 93–98.
19 D. Kim, Y. Jung, J. Sun, C. Yeom, H. Park, D. G. Jung, Y. Ju, K. Chen, A. Javey and G. Cho, *Nanoscale*, 2016, **8**, 19876–19881.
20 W. Lee, H. Koo, J. Sun, J. Noh, K. S. Kwon, C. Yeom, Y. Choi, K. Chen, A. Javey and G. Cho, *Sci. Rep.*, 2015, **5**, 1–10.
21 M. Koutake and Y. Katayama, in 2014 International Conference on Electronics Packaging, ICEP 2014, IEEE Computer Society, 2014, pp. 279–282.
22 Y. M. Choi, E. S. Lee, T. M. Lee and K. Y. Kim, *Microelectron. Eng.*, 2015, **134**, 1–6.
23 A. Sneck, T. Mäkelä and A. Alastalo, *Flexible Printed Electron.*, 2018, **3**, 014001.
24 W. Tang, Y. Huang, L. Han, R. Liu, Y. Su, X. Guo and F. Yan, *J. Mater. Chem. C*, 2019, **7**, 790–808.
25 S. Chung, K. Cho and T. Lee, *Adv. Sci.*, 2019, **6**, 1801445.
26 J. Sworakowski, *Synth. Met.*, 2018, **235**, 125–130.
27 J. Zaumseil and H. Sirringhaus, *Chem. Rev.*, 2007, **107**, 1296–1323.
28 P. Weimer, *Proc. IRE*, 1962, **50**, 1462–1469.
29 G. Horowitz, *Adv. Mater.*, 1998, **10**, 365–377.
30 A. Nawaz, A. C. B. Tavares, T. Trang Do, B. B. Patil, P. Sonar and I. A. Hümmelgen, *Flexible Printed Electron.*, 2018, **3**, 015006.
31 F. Garnier, R. Hajlaoui, A. Yassar and P. Srivastava, *Science*, 1994, **265**, 1684–1686.
32 H. Rost, J. Ficker, J. S. Alonso, L. Leenders and I. McCulloch, *Synth. Met.*, 2004, **145**, 83–85.
33 G. Albrecht, S. Heuser, C. Keil and D. Schlettwein, *Mater. Sci. Semicond. Process.*, 2015, **40**, 772–776.
34 H. Jia, S. Gowrisanker, G. K. Pant, R. M. Wallace and B. E. Gnade, *J. Vac. Sci. Technol., A*, 2006, **24**, 1228–1232.
35 B. Gburek and V. Wagner, *Org. Electron.*, 2010, **11**, 814–819.
36 M. Nurul Islam, *J. Appl. Phys.*, 2011, **110**, 114906.
37 A. Nawaz, I. Cruz-Cruz, J. S. Rego, M. Koehler, S. P. Gopinathan, A. Kumar and I. A. Hümmelgen, *Semicond. Sci. Technol.*, 2017, **32**, 084003.
38 G. Horowitz, X. Peng, D. Fichou and F. Garnier, *J. Appl. Phys.*, 1990, **67**, 528–532.
39 Y. Yuan, G. Giri, A. L. Ayzner, A. P. Zoombelt, S. C. B. Mannsfeld, J. Chen, D. Nordlund, M. F. Toney, J. Huang and Z. Bao, *Nat. Commun.*, 2014, **5**, 3005.
40 H.-R. Tseng, H. Phan, C. Luo, M. Wang, L. A. Perez, S. N. Patel, L. Ying, E. J. Kramer, T.-Q. Nguyen, G. C. Bazan and A. J. Heeger, *Adv. Mater.*, 2014, **26**, 2993–2998.

41 A. Nawaz, A. Kumar and I. A. Hümmelgen, *Org. Electron.*, 2017, **51**, 94–102.

42 *Printed organic and molecular electronics*, ed. D. R. Gamota, P. Brazis, K. Kalyanasundaram and J. Zhang, Springer Science & Business Media, 2013.

43 H. Bässler and A. Köhler, *Electronic Processes in Organic Semiconductors: An Introduction*, Wiley-VCH, 2015.

44 P. Gu, Y. Yao, L. Feng, S. Niu and H. Dong, *Polym. Chem.*, 2015, **6**, 7933–7944.

45 S. G. Surya, H. N. Raval, R. Ahmad, P. Sonar, K. N. Salama and V. R. Rao, *TrAC Trends Anal. Chem.*, 2019, **111**, 27–36.

46 K.-J. Baeg, M. Binda, D. Natali, M. Caironi and Y.-Y. Noh, *Adv. Mater.*, 2013, **25**, 4267–4295.

47 Y. Wakayama, R. Hayakawa and H.-S. Seo, *Sci. Technol. Adv. Mater.*, 2014, **15**, 024202.

48 H.-S. Kang, C.-S. Choi, W.-Y. Choi, D.-H. Kim and K.-S. Seo, *Appl. Phys. Lett.*, 2004, **84**, 3780–3782.

49 M. Y. Lee, J. Hong, E. K. Lee, H. Yu, H. Kim, J. U. Lee, W. Lee and J. H. Oh, *Adv. Funct. Mater.*, 2016, **26**, 1445–1453.

50 Y. S. Rim, Y. M. Yang, S.-H. Bae, H. Chen, C. Li, M. S. Goorsky and Y. Yang, *Adv. Mater.*, 2015, **27**, 6885–6891.

51 D. Yang, L. Zhang, H. Wang, Y. Wang, Z. Li, T. Song, C. Fu, S. Yang and B. Zou, *IEEE Photonics Technol. Lett.*, 2015, **27**, 233–236.

52 H. Wang, H. Liu, Q. Zhao, Z. Ni, Y. Zou, J. Yang, L. Wang, Y. Sun, Y. Guo, W. Hu and Y. Liu, *Adv. Mater.*, 2017, **29**, 1701772.

53 T. Leydecker, M. Herder, E. Pavlica, G. Bratina, S. Hecht, E. Orgiu and P. Samorì, *Nat. Nanotechnol.*, 2016, **11**, 769–775.

54 C. S. Smithson, D. Ljubic, Y. Wu and S. Zhu, *J. Mater. Chem. C*, 2015, **3**, 8090–8096.

55 Z.-D. Zhang, X. Gao, Y.-N. Zhong, J. Liu, L.-X. Zhang, S. Wang, J.-L. Xu and S.-D. Wang, *Adv. Electron. Mater.*, 2017, **3**, 1700052.

56 J.-J. Lv, X. Gao, L.-X. Zhang, Y. Feng, J.-L. Xu, J. Xiao, B. Dong and S.-D. Wang, *Appl. Phys. Lett.*, 2019, **115**, 113302.

57 A. R. Tuktarov, R. B. Salikhov, A. A. Khuzin, N. R. Popod'ko, I. N. Safargalin, I. N. Mullagaliev and U. M. Dzhemilev, *RSC Adv.*, 2019, **9**, 7505–7508.

58 L.-X. Zhang, X. Gao, J.-J. Lv, Y.-N. Zhong, C. Xu, J.-L. Xu and S.-D. Wang, *ACS Appl. Mater. Interfaces*, 2019, **11**, 40366–40371.

59 X. Gao, C.-H. Liu, X.-J. She, Q.-L. Li, J. Liu and S.-D. Wang, *Org. Electron.*, 2014, **15**, 2486–2491.

60 Y. J. Jeong, D.-J. Yun, S. H. Kim, J. Jang and C. E. Park, *ACS Appl. Mater. Interfaces*, 2017, **9**, 11759–11769.

61 E. Orgiu and P. Samorì, *Adv. Mater.*, 2014, **26**, 1827–1845.

62 H. Chen, N. Cheng, W. Ma, M. Li, S. Hu, L. Gu, S. Meng and X. Guo, *ACS Nano*, 2016, **10**, 436–445.

63 H. Laurs and G. Heiland, *Thin Solid Films*, 1987, **149**, 129–142.

64 A. Assadi, G. Gustafsson, M. Willander, C. Svensson and O. Inganäs, *Synth. Met.*, 1990, **37**, 123–130.

65 G. Guillaud, M. Al Sadoun, M. Maitrot, J. Simon and M. Bouvet, *Chem. Phys. Lett.*, 1990, **167**, 503–506.

66 J. Yu, X. Yu, L. Zhang and H. Zeng, *Sens. Actuators, B*, 2012, **173**, 133–138.

67 N. Huo, S. Yang, Z. Wei, S.-S. Li, J.-B. Xia and J. Li, *Sci. Rep.*, 2015, **4**, 5209.

68 S. G. Surya, S. S. Nagarkar, S. K. Ghosh, P. Sonar and V. Ramgopal Rao, *Sens. Actuators, B*, 2016, **223**, 114–122.

69 S. G. Surya, B. S. N. Ashwath, S. Mishra, A. R. B. Karthik, A. B. Sastry, B. L. V. Prasad, D. Rangappa and V. R. Rao, *Sens. Actuators, B*, 2016, **235**, 378–385.

70 C. Zhang, P. Chen and W. Hu, *Chem. Soc. Rev.*, 2015, **44**, 2087–2107.

71 L. Torsi, A. Dodabalapur, L. Sabbatini and P. Zambonin, *Sens. Actuators, B*, 2000, **67**, 312–316.

72 M. T. Vijjapu, S. G. Surya, S. Yuvaraja, X. Zhang, H. N. Alshareef and K. N. Salama, *ACS Sens.*, 2020, **5**, 984–993.

73 L. Torsi, M. Magliulo, K. Manoli and G. Palazzo, *Chem. Soc. Rev.*, 2013, **42**, 8612–8628.

74 B. Crone, A. Dodabalapur, A. Gelperin, L. Torsi, H. E. Katz, A. J. Lovinger and Z. Bao, *Appl. Phys. Lett.*, 2001, **78**, 2229–2231.

75 L. Torsi, A. J. Lovinger, B. Crone, T. Someya, A. Dodabalapur, H. E. Katz and A. Gelperin, *J. Phys. Chem. B*, 2002, **106**, 12563–12568.

76 S. Tiwari, A. K. Singh, L. Joshi, P. Chakrabarti, W. Takashima, K. Kaneto and R. Prakash, *Sens. Actuators, B*, 2012, **171–172**, 962–968.

77 J. E. Royer, E. D. Kappe, C. Zhang, D. T. Martin, W. C. Trogler and A. C. Kummel, *J. Phys. Chem. C*, 2012, **116**, 24566–24572.

78 A.-M. Andringa, M.-J. Spijkman, E. C. P. Smits, S. G. J. Mathijssen, P. A. van Hal, S. Setayesh, N. P. Willard, O. V. Borshchev, S. A. Ponomarenko, P. W. M. Blom and D. M. de Leeuw, *Org. Electron.*, 2010, **11**, 895–898.

79 Q. Liu, Y. Liu, F. Wu, X. Cao, Z. Li, M. Alharbi, A. N. Abbas, M. R. Amer and C. Zhou, *ACS Nano*, 2018, **12**, 1170–1178.

80 T. Someya, T. Sekitani, S. Iba, Y. Kato, H. Kawaguchi and T. Sakurai, *Proc. Natl. Acad. Sci. U. S. A.*, 2004, **101**, 9966–9970.

81 G. Darlinski, U. Böttger, R. Waser, H. Klauk, M. Halik, U. Zschieschang, G. Schmid and C. Dehm, *J. Appl. Phys.*, 2005, **97**, 093708.

82 G. Schwartz, B. C.-K. Tee, J. Mei, A. L. Appleton, D. H. Kim, H. Wang and Z. Bao, *Nat. Commun.*, 2013, **4**, 1859.

83 Y. Mi, Y. Chan, D. Trau, P. Huang and E. Chen, *Polymer*, 2006, **47**, 5124–5130.

84 W. Nichols, *Am. J. Hypertens.*, 2005, **18**, 3–10.

85 Y. Zang, F. Zhang, D. Huang, X. Gao, C. Di and D. Zhu, *Nat. Commun.*, 2015, **6**, 6269.

86 S. Y. Yeo, S. Park, Y. J. Yi, D. H. Kim and J. A. Lim, *ACS Appl. Mater. Interfaces*, 2017, **9**, 42996–43003.

87 Z. Liu, Z. Yin, J. Wang and Q. Zheng, *Adv. Funct. Mater.*, 2019, **29**, 1806092.

88 S. Baek, G. Y. Bae, J. Kwon, K. Cho and S. Jung, *ACS Appl. Mater. Interfaces*, 2019, **11**, 31111–31118.

89 Y. Ye, C. C. Ahn, C. Witham, B. Fultz, J. Liu, A. G. Rinzler, D. Colbert, K. A. Smith and R. E. Smalley, *Appl. Phys. Lett.*, 1999, **74**, 2307.

90 P. J. Mankowski, J. Kanevsky, P. Bakirtzian and S. Cugno, *Burns*, 2016, **42**, e61–e64.

91 S. Yuvaraja and A. S. Vithya, in 2015 7th International Conference on New Technologies, Mobility and Security - Proceedings of NTMS 2015 Conference and Workshops, Institute of Electrical and Electronics Engineers Inc., 2015.

92 A. Akturk, N. Goldsman and G. Metze, *IEEE Trans. Electron Devices*, 2005, **52**, 2395–2403.

93 H.-C. Chien, J. H. Lau, Y.-L. Chao, M.-J. Dai, R.-M. Tain, L. Li, P. Su, J. Xue and M. Brillhart, in 2012 IEEE 62nd Electronic Components and Technology Conference, IEEE, 2012, pp. 1866–1873.

94 M. A. Khan, C. Allemand and T. W. Eagar, *Rev. Sci. Instrum.*, 1991, **62**, 392–402.

95 D. O'Sullivan and M. Cotterell, *J. Mater. Process. Technol.*, 2001, **118**, 301–308.

96 A. Bakker and J. H. Huijsing, *IEEE J. Solid-State Circuits*, 1996, **31**, 933–937.

97 L. V. Nguyen, D. Hwang, S. Moon, D. S. Moon and Y. Chung, *Opt. Express*, 2008, **16**, 11369–11375.

98 M. Song, J. Seo, H. Kim and Y. Kim, *ACS Omega*, 2017, **2**, 4065–4070.

99 M. L. Hammock, A. Chortos, B. C.-K. Tee, J. B.-H. Tok and Z. Bao, *Adv. Mater.*, 2013, **25**, 5997–6038.

100 X. Wang, Y. Gu, Z. Xiong, Z. Cui and T. Zhang, *Adv. Mater.*, 2014, **26**, 1336–1342.

101 X. Wu, Y. Ma, G. Zhang, Y. Chu, J. Du, Y. Zhang, Z. Li, Y. Duan, Z. Fan and J. Huang, *Adv. Funct. Mater.*, 2015, **25**, 2138–2146.

102 K.-I. Jang, S. Y. Han, S. Xu, K. E. Mathewson, Y. Zhang, J.-W. Jeong, G.-T. Kim, R. C. Webb, J. W. Lee, T. J. Dawidczyk, R. H. Kim, Y. M. Song, W.-H. Yeo, S. Kim, H. Cheng, S. Il Rhee, J. Chung, B. Kim, H. U. Chung, D. Lee, Y. Yang, M. Cho, J. G. Gaspar, R. Carbonari, M. Fabiani, G. Gratton, Y. Huang and J. A. Rogers, *Nat. Commun.*, 2014, **5**, 4779.

103 A. M. Hussain, E. B. Lizardo, G. A. Torres Sevilla, J. M. Nassar and M. M. Hussain, *Adv. Healthcare Mater.*, 2015, **4**, 665–673.

104 T. Q. Trung and N.-E. Lee, *Adv. Mater.*, 2016, **28**, 4338–4372.

105 H.-Y. Ma, Q.-A. Huang, M. Qin and T. Lu, *J. Micromech. Microeng.*, 2010, **20**, 055036.

106 S. Abdullah, Z. Ahmad and K. Sulaiman, *Sensors*, 2014, **14**, 9878–9888.

107 S. Harada, K. Kanao, Y. Yamamoto, T. Arie, S. Akita and K. Takei, *ACS Nano*, 2014, **8**, 12851–12857.

108 S. Mandal, M. Banerjee, S. Roy, A. Mandal, A. Ghosh, B. Satpati and D. K. Goswami, *ACS Appl. Mater. Interfaces*, 2019, **11**, 4193–4202.

109 T. Minamiki, S. Tokito and T. Minami, *Anal. Sci.*, 2019, **35**, 103–106.

110 T. Minami, T. Sato, T. Minamiki, K. Fukuda, D. Kumaki and S. Tokito, *Biosens. Bioelectron.*, 2015, **74**, 45–48.

111 J. Oh, J. S. Lee, J. Jun, S. G. Kim and J. Jang, *ACS Appl. Mater. Interfaces*, 2017, **9**, 39526–39533.

112 H. U. Khan, M. E. Roberts, W. Knoll and Z. Bao, *Chem. Mater.*, 2011, **23**, 1946–1953.

113 S. G. Surya, S. M. Majhi, A. A. Lahcen, S. Yuvaraja, K. N. Chappanda, K. N. Salama, D. K. Agarwal and K. N. Chappanda, *J. Mater. Chem. B*, 2019, **8**, 18–26.

114 R. Paradiso, A. Alonso, D. Cianflone, A. Milsis, T. Vavouras and C. Malliopoulos, in 2008 30th Annual International Conference of the IEEE Engineering in Medicine and Biology Society, IEEE, 2008, pp. 1699–1702.

115 A. J. Bandodkar and J. Wang, *Trends Biotechnol.*, 2014, **32**, 363–371.

116 C. Kotlowski, P. Aspermair, H. U. Khan, C. Reiner-Rozman, J. Breu, S. Szunerits, J.-J. Kim, Z. Bao, C. Kleber, P. Pelosi and W. Knoll, *Flexible Printed Electron.*, 2018, **3**, 034003.

117 S. G. Surya, S. K. Samji, P. Dhamini, B. P. Ganne, P. Sonar and V. R. Rao, *IEEE Sens. J.*, 2018, **18**, 1364–1372.

118 F. Zhang, C. Di, N. Berdunov, Y. Hu, Y. Hu, X. Gao, Q. Meng, H. Sirringhaus and D. Zhu, *Adv. Mater.*, 2013, **25**, 1401–1407.

119 X. Yu, N. Zhou, S. Han, H. Lin, D. B. Buchholz, J. Yu, R. P. H. Chang, T. J. Marks and A. Facchetti, *J. Mater. Chem. C*, 2013, **1**, 6532–6535.

120 G.-S. Ryu, K. H. Park, W.-T. Park, Y.-H. Kim and Y.-Y. Noh, *Org. Electron.*, 2015, **23**, 76–81.

121 B. Nketia-Yawson, A.-R. Jung, Y. Noh, G.-S. Ryu, G. D. Tabi, K.-K. Lee, B. Kim and Y.-Y. Noh, *ACS Appl. Mater. Interfaces*, 2017, **9**, 7322–7330.

122 K. Tang, Z. Song, Q. Tang, H. Tian, Y. Tong and Y. Liu, *IEEE Electron Device Lett.*, 2018, **39**, 119–122.

123 O. Y. Kweon, M. Y. Lee, T. Park, H. Jang, A. Jeong, M.-K. Um and J. H. Oh, *J. Mater. Chem. C*, 2019, **7**, 1525–1531.

124 S. Chowdhury, S. Dey, S. Guttikunda, A. Pillarisetti, K. R. Smith and L. Di Girolamo, *Proc. Natl. Acad. Sci. U. S. A.*, 2019, **116**, 10711–10716.

125 S. Yuvaraja, H. Dhasmana, A. Kumar, B. Barman, V. Kumar, A. Verma and V. K. Jain, *Springer Proceedings in Physics*, Springer Science and Business Media, LLC, 2019, vol. 215, pp. 939–946.

126 M. C. Petty, *Biosens. Bioelectron.*, 1995, **10**, 129–134.

127 L. Li, P. Gao, M. Baumgarten, K. Müllen, N. Lu, H. Fuchs and L. Chi, *Adv. Mater.*, 2013, **25**, 3419–3425.

128 S.-W. Lee, N. Takahara, S. Korposh, D.-H. Yang, K. Toko and T. Kunitake, *Anal. Chem.*, 2010, **82**, 2228–2236.

129 S. Ji, H. Wang, T. Wang and D. Yan, *Adv. Mater.*, 2013, **25**, 1755–1760.

130 R. P. Ortiz, A. Facchetti and T. J. Marks, *Chem. Rev.*, 2010, **110**, 205–239.

131 M. Scharnberg, V. Zaporojtchenko, R. Adelung, F. Faupel, C. Pannemann, T. Diekmann and U. Hilleringmann, *Appl. Phys. Lett.*, 2007, **90**, 013501.

132 X. Cheng, M. Caironi, Y.-Y. Noh, J. Wang, C. Newman, H. Yan, A. Facchetti and H. Sirringhaus, *Chem. Mater.*, 2010, **22**, 1559–1566.

133 D. K. Hwang, C. Fuentes-Hernandez, J. Kim, W. J. Potscavage, S.-J. Kim and B. Kippelen, *Adv. Mater.*, 2011, **23**, 1293–1298.

134 J. Yang, Z. Zhao, S. Wang, Y. Guo and Y. Liu, *Chem*, 2018, **4**, 2748–2785.

135 D. Khim, G.-S. Ryu, W.-T. Park, H. Kim, M. Lee and Y.-Y. Noh, *Adv. Mater.*, 2016, **28**, 2752–2759.

136 T. Lei, J.-H. Dou, Z.-J. Ma, C.-H. Yao, C.-J. Liu, J.-Y. Wang and J. Pei, *J. Am. Chem. Soc.*, 2012, **134**, 20025–20028.

137 B. Nketia-Yawson, H. Lee, D. Seo, Y. Yoon, W. Park, K. Kwak, H. J. Son, B. Kim and Y. Noh, *Adv. Mater.*, 2015, **27**, 3045–3052.

138 X. Li, X. Liu, P. Sun, Y. Feng, H. Shan, X. Wu, J. Xu, C. Huang, Z.-K. Chen and Z.-X. Xu, *RSC Adv.*, 2017, **7**, 17076–17084.

139 Y. Chen, H. Chang, H. Tian, C. Bao, W. Li, D. Yan, Y. Geng and F. Wang, *Org. Electron.*, 2012, **13**, 3268–3275.

140 X. Zhao, T. Pei, B. Cai, S. Zhou, Q. Tang, Y. Tong, H. Tian, Y. Geng and Y. Liu, *J. Mater. Chem. C*, 2014, **2**, 5382–5388.

141 M. E. Roberts, A. N. Sokolov and Z. Bao, *J. Mater. Chem.*, 2009, **19**, 3351–3363.

142 A. N. Sokolov, M. E. Roberts, O. B. Johnson, Y. Cao and Z. Bao, *Adv. Mater.*, 2010, **22**, 2349–2353.

143 Z. Chen and C. Lu, *Sens. Lett.*, 2005, **3**, 274–295.

144 S. G. Surya, S. Yuvaraja, K. N. Salama, M. Shojaei Baghini and V. S. Palaparthy, in Proceedings of IEEE Sensors, Institute of Electrical and Electronics Engineers Inc., 2019, vol. 2019.

145 J. M. Thorp, *Trans. Faraday Soc.*, 1959, **55**, 442–454.

146 V. K. Khanna, *Sens. Actuators, B*, 2015, **213**, 351–359.

147 U. Mittal, T. Islam, A. T. Nimal and M. U. Sharma, *IEEE Trans. Electron Devices*, 2015, **62**, 4242–4250.

148 N. K. Singh, B. Choudhuri, A. Mondal, J. C. Dhar, T. Goswami, S. Saha and C. Ngangbam, *Electron. Mater. Lett.*, 2014, **10**, 975–980.

149 J.-W. Yoon, J.-S. Kim, T.-H. Kim, Y. J. Hong, Y. C. Kang and J.-H. Lee, *Small*, 2016, **12**, 4229–4240.

150 N. B. Ibrahim, A. Z. Arsad, N. Yusop and H. Baqiah, *Mater. Sci. Semicond. Process.*, 2016, **53**, 72–78.

151 A. S. Ismail, M. H. Mamat, M. F. Malek, M. M. Yusoff, R. Mohamed, N. D. M. Sin, A. B. Suriani and M. Rusop, *Mater. Sci. Semicond. Process.*, 2018, **81**, 127–138.

152 Y. Zhao, B. Yang and J. Liu, *Sens. Actuators, B*, 2018, **271**, 256–263.

153 D. Zhang, D. Wang, X. Zong, G. Dong and Y. Zhang, *Sens. Actuators, B*, 2018, **262**, 531–541.

154 Y. Zhao, B. Yang, J. Liu, X. Chen, X. Wang and C. Yang, in 2018 IEEE Micro Electro Mechanical Systems (MEMS), IEEE, 2018, pp. 912–915.

155 H. Zhu, Q. Li, Y. Ren, Q. Gao, J. Chen, N. Wang, J. Deng and X. Xing, *Small*, 2018, **14**, 1703974.

156 J. Zhang, Y. Zhen, H. Xue, X. Gao, W. Wang, Y. Li, T. Hayat and N. S. Alharbi, *Sens. Actuators, B*, 2019, **283**, 643–650.

157 C. Ashok and K. Venkateswara Rao, *J. Mater. Sci.: Mater. Electron.*, 2016, **27**, 8816–8825.

158 M. Zhang, S. Wei, W. Ren and R. Wu, *Sensors*, 2017, **17**, 1310.

159 X. Zhao, X. Chen, X. Yu, P. Du, N. Li and X. Chen, *IEEE Sens. J.*, 2017, **17**, 6148–6152.

160 E. S. Araújo, J. Libardi, P. M. Faia and H. P. de Oliveira, *J. Mater. Sci.: Mater. Electron.*, 2017, **28**, 16575–16583.

161 M. I. Azmer, F. Aziz, Z. Ahmad, E. Raza, M. A. Najeeb, N. Fatima, T. M. Bawazeer, M. S. Alsoufi, R. A. Shakoor and K. Sulaiman, *Talanta*, 2017, **174**, 279–284.

162 G. Dubourg, J. Katona, M. Rodović, S. Savić, G. Kitic, G. Niarchos, N. Jancović and V. Crnojević-Bengin, *J. Phys.: Conf. Ser.*, 2017, **939**, 012008.

163 A. Solonaru, M. Grigoras, I. Petrila and F. Tudorache, *J. Appl. Polym. Sci.*, 2019, **136**, 47743.

164 Y. J. Jang, Y. E. Jung, G. W. Kim, C. Y. Lee and Y. D. Park, *RSC Adv.*, 2019, **9**, 529–535.

165 X.-J. Lv, M.-S. Yao, G.-E. Wang, Y.-Z. Li and G. Xu, *Sci. China: Chem.*, 2017, **60**, 1197–1204.

166 J. Boudaden, M. Steinmaßl, H.-E. Endres, A. Drost, I. Eisele, C. Kutter and P. Müller-Buschbaum, *Sensors*, 2018, **18**, 1516.

167 K. Amer, S. Ebrahim, M. Feteha, M. Soliman and A. El-Shaer, in 2017 34th National Radio Science Conference (NRSC), IEEE, 2017, pp. 440–447.

168 Q. Zafar, S. M. Abdullah, M. I. Azmer, M. A. Najeeb, K. W. Qadir and K. Sulaiman, *Sens. Actuators, B*, 2018, **255**, 2652–2656.

169 Z.-T. Zhu, J. T. Mason, R. Dieckmann and G. G. Malliaras, *Appl. Phys. Lett.*, 2002, **81**, 4643–4645.

170 D. Li, E.-J. Borkent, R. Nortrup, H. Moon, H. Katz and Z. Bao, *Appl. Phys. Lett.*, 2005, **86**, 042105.

171 Y. D. Park, B. Kang, H. S. Lim, K. Cho, M. S. Kang and J. H. Cho, *ACS Appl. Mater. Interfaces*, 2013, **5**, 8591–8596.

172 V. Seena, A. Nigam, P. Pant, S. Mukherji and V. R. Rao, *J. Microelectromechanical Syst.*, 2012, **21**, 294–301.

173 P. Ray and V. Ramgopal Rao, *Appl. Phys. Lett.*, 2013, **102**, 064101.

174 D. Thuau, M. Abbas, G. Wantz, L. Hirsch, I. Dufour and C. Ayela, *Sci. Rep.*, 2016, **6**, 38672.

175 M. Irimia-Vladu, E. D. Głowacki, G. Voss, S. Bauer and N. S. Sariciftci, *Mater. Today*, 2012, **15**, 340–346.

176 Q. Zhang, W. Bao, A. Gong, T. Gong, D. Ma, J. Wan, J. Dai, J. N. Munday, J.-H. He, L. Hu and D. Zhang, *Nanoscale*, 2016, **8**, 14237–14242.

177 S. Yuvaraja, V. Kumar, H. Dhasmana, A. Kumar, A. Verma and V. K. Jain, *J. Mater. Sci.: Mater. Electron.*, 2019, **30**, 7618–7628.

178 C. Cooksey, *Molecules*, 2001, **6**, 736–769.

179 H. Zollinger, *Color chemistry: syntheses, properties, and applications of organic dyes and pigments*, John Wiley & Sons, 2003.

180 E. D. Głowacki, G. Voss, L. Leonat, M. Irimia-Vladu, S. Bauer and N. S. Sariciftci, *Isr. J. Chem.*, 2012, **52**, 540–551.

181 P. Meredith, C. J. Bettinger, M. Irimia-Vladu, A. B. Mostert and P. E. Schwenn, *Rep. Prog. Phys.*, 2013, **76**, 034501.

182 E. D. Głowacki, G. Voss and N. S. Sariciftci, *Adv. Mater.*, 2013, **25**, 6783–6800.

183 H. Kim, G. Kim, I. Song, J. Lee, H. Abdullah, C. Yang and J. H. Oh, *RSC Adv.*, 2018, **8**, 14747–14752.

184 B. Lucas, T. Trigaud and C. Videlot-Ackermann, *Polym. Int.*, 2012, **61**, 374–389.

185 A. Nawaz, L. Merces, D. M. de Andrade, D. H. S. de Camargo and C. C. Bof Bufon, *Nat. Commun.*, 2020, **11**, 841.

186 T. Sekitani, U. Zschieschang, H. Klauk and T. Someya, *Nat. Mater.*, 2010, **9**, 1015–1022.

187 M. Kim, H.-J. Ha, H.-J. Yun, I.-K. You, K.-J. Baeg, Y.-H. Kim and B.-K. Ju, *Org. Electron.*, 2014, **15**, 2677–2684.

188 E. Bystrenova, M. Jelitai, I. Tonazzini, A. N. Lazar, M. Huth, P. Stoliar, C. Dionigi, M. G. Cacace, B. Nickel, E. Madarasz and F. Biscarini, *Adv. Funct. Mater.*, 2008, **18**, 1751–1756.

189 M. Irimia-Vladu, *Chem. Soc. Rev.*, 2014, **43**, 588–610.

190 C. C. Mattheus, A. B. Dros, J. Baas, A. Meetsma, J. L. de Boer and T. T. M. Palstra, *Acta Crystallogr., Sect. C: Cryst. Struct. Commun.*, 2001, **57**, 939–941.

191 H. Klauk, *Organic electronics: materials, manufacturing, and applications*, Wiley-VCH, 2006.

192 S. E. Fritz, S. M. Martin, C. D. Frisbie, M. D. Ward and M. F. Toney, *J. Am. Chem. Soc.*, 2004, **126**, 4084–4085.

193 G. H. Gelinck, H. E. A. Huitema, E. van Veenendaal, E. Cantatore, L. Schrijnemakers, J. B. P. H. van der Putten, T. C. T. Geuns, M. Beenhakkers, J. B. Giesbers, B.-H. Huisman, E. J. Meijer, E. M. Benito, F. J. Touwslager, A. W. Marsman, B. J. E. van Rens and D. M. de Leeuw, *Nat. Mater.*, 2004, **3**, 106–110.

194 O. D. Jurchescu, J. Baas and T. T. M. Palstra, *Appl. Phys. Lett.*, 2004, **84**, 3061–3063.

195 M. Debucquoy, S. Verlaak, S. Steudel, K. Myny, J. Genoe and P. Heremans, *Appl. Phys. Lett.*, 2007, **91**, 103508.

196 J. Park, J.-H. Seo, S.-W. Yeom, C. Yao, V. W. Yang, Z. Cai, Y. M. Jhon and B.-K. Ju, *Adv. Opt. Mater.*, 2018, **6**, 1701140.

197 Q. Wang, M. Zhu, D. Wu, G. Zhang, X. Wang, H. Lu, X. Wang and L. Qiu, *J. Mater. Chem. C*, 2015, **3**, 10734–10741.

198 M. Zhu, S. Lv, Q. Wang, G. Zhang, H. Lu and L. Qiu, *Nanoscale*, 2016, **8**, 7738–7748.

199 Y. He, J. T. E. Quinn, D. Hou, J. H. L. Ngai and Y. Li, *J. Mater. Chem. C*, 2017, **5**, 12163–12171.

200 M. J. Kim, S. Choi, M. Lee, H. Heo, Y. Lee, J. H. Cho and B. Kim, *ACS Appl. Mater. Interfaces*, 2017, **9**, 19011–19020.

201 X. Wang, F. Zhao, Z. Xue, Y. Yuan, M. Huang, G. Zhang, Y. Ding and L. Qiu, *Adv. Electron. Mater.*, 2019, **5**, 1900174.

202 S. Mohri, A. Yamada, N. Goda, M. Nakamura, K. Naruse and F. Kajiya, *Sens. Actuators, B*, 2008, **134**, 447–450.

203 B. Schyrr, S. Pasche, E. Scolan, R. Ischer, D. Ferrario, J.-A. Porchet and G. Voirin, *Sens. Actuators, B*, 2014, **194**, 238–248.

204 P. Salvo, N. Calisi, B. Melai, B. Cortigiani, M. Mannini, A. Caneschi, G. Lorenzetti, C. Paoletti, T. Lomonaco, A. Paolicchi, I. Scataglini, V. Dini, M. Romanelli, R. Fuoco and F. Di Francesco, *Biosens. Bioelectron.*, 2017, **91**, 870–877.

205 Aqeel-ur-Rehman, A. Z. Abbasi, N. Islam and Z. A. Shaikh, *Comput. Stand. Interfaces*, 2014, **36**, 263–270.

206 R. Karimi Shervedani, H. R. Zare Mehrdjardi and S. H. Kazemi Ghahfarokhi, *J. Iran. Chem. Soc.*, 2007, **4**, 221–228.

207 S. Dutta, D. Sarma and P. Nath, *AIP Adv.*, 2015, **5**, 057151.

208 A. Riedinger, M. Pernia Leal, S. R. Deka, C. George, I. R. Franchini, A. Falqui, R. Cingolani and T. Pellegrino, *Nano Lett.*, 2011, **11**, 3136–3141.

209 N. Lopez-Ruiz, V. F. Curto, M. M. Erenas, F. Benito-Lopez, D. Diamond, A. J. Palma and L. F. Capitan-Vallvey, *Anal. Chem.*, 2014, **86**, 9554–9562.

210 R. S. Dudhe, J. Sinha, A. Kumar and V. R. Rao, *Sens. Actuators, B*, 2010, **148**, 158–165.

211 H. N. Raval and V. R. Rao, *IEEE Electron Device Lett.*, 2010, **31**, 1482–1484.

212 X. Wu, S. Mao, J. Chen and J. Huang, *Adv. Mater.*, 2018, **30**, 1705642.

213 K. Diallo, M. Erouel, J. Tardy, E. André and J.-L. Garden, *Appl. Phys. Lett.*, 2007, **91**, 183508.

214 K. Diallo, M. Lemiti, J. Tardy, F. Bessueille and N. Jaffrezic-Renault, *Appl. Phys. Lett.*, 2008, **93**, 183305.

215 A. Caboni, E. Orgiu, M. Barbaro and A. Bonfiglio, *IEEE Sens. J.*, 2009, **9**, 1963–1970.

216 Q. Li, J. Zhao, Y. Huang, W. Tang, S. Peng, S. Qiu, Q. Zhang and X. Guo, *IEEE Electron Device Lett.*, 2018, **39**, 591–594.

217 M. L. Faupel and G. A. P. Ganepola, *US Pat.*, 5320101A, 1994.

218 T. Aytur, J. Foley, M. Anwar, B. Boser, E. Harris and P. R. Beatty, *J. Immunol. Methods*, 2006, **314**, 21–29.

219 P. J. Mazzone, J. Hammel, R. Dweik, J. Na, C. Czich, D. Laskowski and T. Mekhail, *Thorax*, 2007, **62**, 565–568.

220 G. Pennazza, M. Santonico and A. F. Agrò, *Sens. Actuators, B*, 2013, **179**, 270–275.

221 M. Cavallari, J. Izquierdo, G. Braga, E. Dirani, M. Pereira-da-Silva, E. Rodríguez and F. Fonseca, *Sensors*, 2015, **15**, 9592–9609.

222 J. R. Carey, K. S. Suslick, K. I. Hulkower, J. A. Imlay, K. R. C. Imlay, C. K. Ingison, J. B. Ponder, A. Sen and A. E. Wittrig, *J. Am. Chem. Soc.*, 2011, **133**, 7571–7576.

223 B. C. Janegitz, J. Cancino and V. Zucolotto, *J. Nanosci. Nanotechnol.*, 2014, **14**, 378–389.

224 M. N. Costa, B. Veigas, J. M. Jacob, D. S. Santos, J. Gomes, P. V. Baptista, R. Martins, J. Inácio and E. Fortunato, *Nanotechnology*, 2014, **25**, 094006.

225 M. Faisal, Q. Saquib, A. A. Alatar, A. A. Al-Khedhairy, A. K. Hegazy and J. Musarrat, *J. Hazard. Mater.*, 2013, **250–251**, 318–332.

226 E. Panieri and M. M. Santoro, *Cell Death Dis.*, 2016, **7**, e2253.

227 P. W. Burridge, Y. F. Li, E. Matsa, H. Wu, S. G. Ong, A. Sharma, A. Holmstrom, A. C. Chang, M. J. Coronado, A. D. Ebert, J. W. Knowles, M. L. Telli, R. M. Witteles, H. M. Blau, D. Bernstein, R. B. Altman and J. C. Wu, *Nat. Med.*, 2016, **5**, 546–555.

228 J. Jeong, M. Essafi, C. Lee, M. Haoues, M. F. Diouani, H. Kim and Y. Kim, *J. Hazard. Mater.*, 2018, **355**, 17–24.

229 J. Elia, P. J. Ambrosini and J. L. Rapoport, *N. Engl. J. Med.*, 1999, **340**, 780–788.

230 C. A. Winstanley, D. M. Eagle and T. W. Robbins, *Clin. Psychol. Rev.*, 2006, **26**, 379–395.

231 D. J. Heal, S. L. Smith, J. Gosden and D. J. Nutt, *J. Psychopharmacol.*, 2013, **27**, 479–496.

232 H. Brownstein, *The Handbook of Drugs and Society*, 2015.

233 L. R. Gowing, S. M. Henry-Edwards, R. J. Irvine and R. L. Ali, *Drug Alcohol Abuse Rev.*, 2002, **21**, 51–63.

234 K. A. Alsenedi and C. Morrison, *J. Chromatogr. B: Anal. Technol. Biomed. Life Sci.*, 2018, **1076**, 91–102.

235 L. B. Scaffardi, N. Pellegri, O. de Sanctis and J. O. Tocho, *Nanotechnology*, 2005, **16**, 158–163.

236 D. Djozan, M. A. Farajzadeh, S. M. Sorouraddin and T. Baheri, *Microchim. Acta*, 2012, **179**, 209–217.

237 K. Graniczkowska, M. Pütz, F. M. Hauser, S. De Saeger and N. V. Beloglazova, *Biosens. Bioelectron.*, 2017, **92**, 741–747.

238 Y. Jang, M. Jang, H. Kim, S. J. Lee, E. Jin, J. Y. Koo, I.-C. Hwang, Y. Kim, Y. H. Ko, I. Hwang, J. H. Oh and K. Kim, *Chem*, 2017, **3**, 641–651.

239 V. Scenev, P. Cosseddu, A. Bonfiglio, I. Salzmann, N. Severin, M. Oehzelt, N. Koch and J. P. Rabe, *Org. Electron.*, 2013, **14**, 1323–1329.

240 M. Song, J. Seo, H. Kim and Y. Kim, *Sci. Rep.*, 2017, **7**, 2630.

241 T. Q. Trung, N. T. Tien, Y. G. Seol and N.-E. Lee, *Org. Electron.*, 2012, **13**, 533–540.

242 K. Ikeda, H. Kuwayama, T. Kobayashi, T. Watanabe, T. Nishikawa, T. Yoshida and K. Harada, *Sens. Actuators, A*, 1990, **23**, 1007–1010.

243 L. Zhou, S. Jung, E. Brandon and T. N. Jackson, *IEEE Trans. Electron Devices*, 2006, **53**, 380–385.

244 R. G. Azevedo, D. G. Jones, A. V. Jog, B. Jamshidi, D. R. Myers, L. Chen, X. Fu, M. Mehregany, M. B. J. Wijesundara and A. P. Pisano, *IEEE Sens. J.*, 2007, **7**, 568–576.

245 H.-H. Chou, A. Nguyen, A. Chortos, J. W. F. To, C. Lu, J. Mei, T. Kurosawa, W.-G. Bae, J. B.-H. Tok and Z. Bao, *Nat. Commun.*, 2015, **6**, 8011.

246 A. Loi, L. Basirico, P. Cosseddu, S. Lai, M. Barbaro, A. Bonfiglio, P. Maiolino, E. Baglini, S. Denei, F. Mastrogiovanni and G. Cannata, *IEEE Sens. J.*, 2013, **13**, 4764–4772.

247 G. Ge, W. Huang, J. Shao and X. Dong, *J. Semicond.*, 2018, **39**, 011012.

248 T. Lindner, G. Paasch and S. Scheinert, *J. Appl. Phys.*, 2005, **98**, 114505.

249 I. Manunza, A. Sulis and A. Bonfiglio, *Appl. Phys. Lett.*, 2006, **89**, 143502.

250 F.-C. Chen, T.-D. Chen, B.-R. Zeng and Y.-W. Chung, *Semicond. Sci. Technol.*, 2011, **26**, 034005.

251 L. G. Villanueva, J. Bausells and J. Brugger, *Front. Mech. Eng.*, 2016, **1**, 15.

252 S. Lai, A. Garufi, F. Madeddu, G. Angius, A. Bonfiglio and P. Cosseddu, *IEEE Sens. J.*, 2019, **19**, 6020–6028.

253 B. Timmer, W. Olthuis and A. van den Berg, *Sens. Actuators, B*, 2005, **107**, 666–677.

254 U. Yogeswaran and S.-M. Chen, *Sensors*, 2008, **8**, 290–313.

255 M. Brischwein, E. R. Motrescu, E. Cabala, A. M. Otto, H. Grothe and B. Wolf, *Lab Chip*, 2003, **3**, 234–240.

256 M. A. Aronova, K. S. Chang, I. Takeuchi, H. Jabs, D. Westerheim, A. Gonzalez-Martin, J. Kim and B. Lewis, *Appl. Phys. Lett.*, 2003, **83**, 1255–1257.

257 B. Hu, W. Chen and J. Zhou, *Sens. Actuators, B*, 2013, **176**, 522–533.

258 W. Qu, R. Green and M. Austin, *Meas. Sci. Technol.*, 2000, **11**, 1111–1118.

259 J. Sun and K. Shida, *IEEE Sens. J.*, 2002, **2**, 62–72.

260 X. Zhao, Q. Hua, R. Yu, Y. Zhang and C. Pan, *Adv. Electron. Mater.*, 2015, **1**, 1500142.

261 A. S. Almansouri, N. A. Alsharif, M. A. Khan, L. Swanepoel, A. Kaidarova, K. N. Salama and J. Kosel, *Adv. Mater. Technol.*, 2019, **4**, 1900493.

262 E. M. C. Fortunato, P. M. C. Barquinha, A. C. M. B. G. Pimentel, A. M. F. Gonçalves, A. J. S. Marques, L. M. N. Pereira and R. F. P. Martins, *Adv. Mater.*, 2005, **17**, 590–594.

263 J. Liu, D. B. Buchholz, J. W. Hennek, R. P. H. Chang, A. Facchetti and T. J. Marks, *J. Am. Chem. Soc.*, 2010, **132**, 11934–11942.

264 J. Liu, D. B. Buchholz, R. P. H. Chang, A. Facchetti and T. J. Marks, *Adv. Mater.*, 2010, **22**, 2333–2337.

265 M. Courté, S. G. Surya, R. Thamankar, C. Shen, V. R. Rao, S. G. Mhaisalkar and D. Fichou, *RSC Adv.*, 2017, **7**, 9772.

266 B. C.-K. Tee, C. Wang, R. Allen and Z. Bao, *Nat. Nanotechnol.*, 2012, **7**, 825–832.

267 Y. J. Tan, J. Wu, H. Li and B. C. K. Tee, *ACS Appl. Mater. Interfaces*, 2018, **10**, 15331–15345.